

ABSTRACT

Title of Dissertation: DEVELOPMENT OF ANALYTICAL METHODS FOR CHARACTERIZATION OF NANOPARTICLES FOR BIO-MEDICAL AND ENVIRONMENTAL APPLICATION BY ION MOBILITY-ICP-MS

Jiaojie Tan, Doctor of Philosophy, 2017

Dissertation directed by: Professor Michael R. Zachariah, Department of Chemical and Biomolecular Engineering and Department of Chemistry and Biochemistry

The development of nanotechnology necessitates appropriate tools for nanoparticle characterization to assure product quality, evaluate safety and facilitate manufacturing. The properties of interest particularly relevant to nanomedicine and environmental ecotoxicology include size, shape, aggregation, concentration, dissolution, surface chemistry, and composition etc. Engineered nanoparticles in a complex matrix, at realistic concentration are two of the major challenges for analytical scientist. Potential transformation of pristine engineered nanomaterials when put in contact with either biological or environmental media further complicate the analytical task.

In this dissertation, I aim to optimize and extend the application of novel hyphenated instruments consisting of differential mobility analysis (DMA) and inductively coupled plasma-mass spectrometry (ICP-MS) for real time size classification and elemental detection in biomedical and environmental fields. I have applied DMA-ICP-MS in

quantitatively characterizing anti-tumor drug delivery platform to assist design and performance evaluation. Optimal balance among drug loading, stability and release performance was achieved and evaluated by DMA-ICP-MS.

I have further developed a novel analytical methodology including DMA and ICP-MS operating in single particle mode (i.e. spICP-MS). I successfully demonstrated and validated the method for accurate and simultaneous size, mass and concentration measurement by NIST reference materials. DMA-spICP-MS was shown with the capability to characterize nanoparticle aggregation state and surface coating. In addition, this technique was shown to be useful for real-world samples with high ionic background due to its ability to remove dissolved ions yielding a cleaner background. Given this validated DMA-spICP-MS method, I applied it to quantifying the geometries of seven gold nanorod samples with different geometries. It was demonstrated that DMA-spICP-MS can achieve fast quantification of both length and diameter with accuracy comparable with TEM analysis. This method provided the capability to separate nanorods from spheres quantifying the geometry for each population.

Finally, an interesting open and high-order rosette protein structure was investigated by electrospray-DMA. The staining procedure was optimized and effect of electrospray process on protein particle structure was evaluated. Protein particle after electrospray was largely maintained. Mobility simulation by MOBCAL showed close matches with experimental data and enabled peak assignment to various particle assembly structures.

DEVELOPMENT OF ANALYTICAL METHODS FOR CHARACTERIZATION
OF NANOPARTICLES FOR BIO-MEDICAL AND ENVIRONMENTAL
APPLICATION BY ION MOBILITY-ICP-MS

by

Jiaojie Tan

Dissertation submitted to the Faculty of the Graduate School of the
University of Maryland, College Park, in partial fulfillment
of the requirements for the degree of
Doctor of Philosophy
2017

Advisory Committee:

Professor Michael R. Zachariah, Chair
Professor Donald K. Milton
Professor Srinivasa R. Raghavan
Professor Amy J. Karlsson
Professor Akua A. Asa-Awuku

© Copyright by
Jiaojie Tan
2017

Acknowledgements

I would like to express my sincere gratitude to all the people who gave me support and help along the way to accomplish my PhD work.

First and foremost, endless thanks to my primary advisor, Dr. Michael R. Zachariah for the generous support for my research, for the trust, patience, kindness, and inspiration you have given me during these years. Your advice and guidance helped me a lot in my research and life. I am fortunate and grateful to have you as my PhD advisor from the deep of my heart. I would also like to thank Dr. Vincent A. Hackley, for his support at NIST, as well as for the insightful suggestion in research, thoughtful encouragement and kind advice both inside and outside academia.

I would like to thank Dr. De-Hao Tsai for teaching me hands-on DMA-ICPMS when I first came to NIST labs. I express my great gratitude to him for helping me establish both skills and right attitude towards conducting research. I also hope to bring my deep gratitude to Dr. Jingyu Liu, my office mate at NIST who is always ready to help me out, and I value every discussion moment that happened at our office as an asset. I would also like to give special thanks to my colleague Dr. Mingdong Li, Dr. Lei Zhou, Dr. Rian You, Dr. Tae Joon Cho, Dr. Hind El Hadri, Dr. Stacey Louie, Dr. Kathryn Riley, Dr. John Pettibone, Dr. Justin Gorham, and Dr. Arnab Mukherjee for help and collaboration. I would like to thank Dr. John E. Bonevich for insightful discussion and help on TEM calibration.

I would also like to thank Dr. Donald K. Milton, Dr. Srinivasa R. Raghavan, Dr. Amy J. Karlsson and Dr. Akua A. Asa-Awuku for serving on my committee and providing me with valuable suggestions and corrections.

I would like to thank my friends for sharing me with joy, laughter and encouragement. Finally, I want to give my heartfelt gratitude to my families who always stand by me, giving me endless love, who share with me tears and laughter, who support me through difficulties and who make me who I am and where I am.

.

Table of Contents

Acknowledgements.....	ii
Table of Contents.....	iv
Abbreviation.....	vi
Nomenclature.....	viii
List of Tables.....	x
List of Figures.....	xi
Chapter 1: Introduction and Overview.....	1
1.1 Nanotechnology, Characterization and Challenges.....	1
1.2 Current tools in nanoparticle characterization.....	6
Chapter 2: Instrumentation.....	10
2.1 Differential Mobility Analyzer (DMA).....	10
2.2 Inductively Coupled Plasma Mass Spectrometry (ICP-MS).....	15
2.2.1 Components of ICP-MS Instrument.....	15
2.2.2 Single particle ICP-MS.....	16
2.3 Hyphenation of ES-DMA-ICP-MS.....	17
2.3.1 Incompatibility issue from ES-DMA-ICP-MS.....	17
2.3.2 Design of Gas Exchange Device (GED).....	18
2.3.3 Schematic of DMA-ICP-MS Hyphenation.....	20
2.4 Scope of the Dissertation.....	21
Chapter 3: Polyethylene Glycol Stabilized Gold Nanoparticle Platform for Chemo- Radiation Therapy: Relating Surface Engineering to Performance using Hyphenated ES-DMA-ICP-MS.....	24
3.1 Introduction.....	24
3.2 Materials and Experiments.....	27
3.2.1 Conjugation of AuNP-(dendron) and AuNP-(dendron)-(SH-PEG).....	28
3.2.2 Complexation with cisplatin.....	30
3.2.3 Optimization of cleaning steps and cisplatin complexation time.....	31
3.2.4 Cisplatin release.....	32
3.2.5 ATR-FTIR.....	33
3.2.6 ES-DMA-ICP-MS.....	33
3.2.7 Quantification of cisplatin loading.....	34
3.3 Discussion.....	35
3.3.1 Molecular conjugation of dendron and SH-PEG on AuNPs.....	35
3.3.2 Binding of cisplatin to surface engineered AuNPs.....	44
3.3.3 Colloidal stability (by ES-DMA-ICP-MS).....	48
3.3.4 Cisplatin Release Performance.....	54
3.4 Conclusions.....	56
Chapter 4: Electrospray Differential Mobility Hyphenated with Single Particle Mass Spectrometry for Characterization of Nanoparticles and their Aggregates.....	57
4.1 Introduction.....	57
4.2 Materials and Data Processing.....	59
4.2.1 Operational Mode of DMA-spICP-MS.....	61
4.2.2 Distinguishing Particle Events.....	63

4.2.3 Transit time from DMA to ICP-MS Determination	63
4.2.4 Particle Mobility Size Determination	66
4.3 Discussion	67
4.3.1 The ES-DMA-spICP-MS spectrum	67
4.3.2 Proof of concept studies.....	69
4.3.3 Resolving mixed populations.....	75
4.3.4 Analysis of discrete aggregates.....	78
4.3.5 Apparent Density for Aggregates	81
4.3.6 Resolving AuNPs from medium containing Au ³⁺	83
4.4 Conclusions.....	87
Chapter 5: Fast quantification of nanorod geometry by DMA-spICP-MS.....	88
5.1 Introduction.....	88
5.2 Materials and Methods.....	90
5.2.1 Basis of ES-DMA-spICP-MS in quantifying nanorod geometry	91
5.2.2 Procedure	92
5.3 Discussion	94
5.3.1 Characterization of GNRs by TEM	94
5.3.2 TEM evaluation for surface coating	97
5.3.3 Accuracy of DMA-spICP-MS for quantitative GNR dimensions	102
5.3.4 Robustness Analysis	104
5.3.5 Nanorod Detection and Separation Based on Aspect Ratio.....	108
5.4 Conclusions.....	112
Chapter 6: Feasibility of ES-DMA to characterize an open and high order structure protein particle.	114
6.1 Introduction.....	114
6.2 Experimental.....	115
6.3 Results and Discussion	116
6.3.1 Consideration prior to ES-DMA measurement.....	116
6.3.2 Staining Protocol Development for Aerosol Protein Particle Deposition	119
6.3.3 Protein Particle Structure after ES	120
6.3.4 Assignment of Peaks in Mobility Spectrum by MOBCAL Simulation...	122
6.4 Conclusions.....	124
Chapter 7: Conclusion and Future work.	125
7.1 Conclusion	125
7.2 Recommended Future Work.....	127
References.....	129

Abbreviation

ASTM	American society for testing and materials
CDER	Center for drug evaluation and research
FDA	Food and drug administration
API	Active pharmaceutical ingredient
CPI	Consumer products inventory
EM	Electron microscopy
SEM	Scanning electron microscopy
TEM	Transmission electron microscopy
EDS	Energy dispersive X-ray spectroscopy
EELS	Electron energy loss spectroscopy
DLS	Dynamic light scattering
FFF	Field flow fractionation
HDC	Hydrodynamic chromatography
NTA	Nanoparticle tracking analysis
FTIR	Fourier transform infrared spectroscopy
ATR-FTIR	Attenuated total reflection-fourier transform infrared spectroscopy
IR	Infrared spectroscopy
TGA-MS	Thermogravimetric analysis-mass spectrometry
MS	Mass spectrometry
ET-AAS	Electrothermal atomic absorption spectroscopy
ICP-OES	Inductively coupled plasma-optical emission spectrometry
ICP-MS	Inductively coupled plasma-mass spectrometry
DMA	Differential mobility analyzer
NP	Nanoparticle
FWHH	Full width at half height
ES	Electrospray
CPC	Condensation Particle Counter
ppt	Parts per trillion
TRA	Time resolved analysis
spICP-MS	Single particle inductively coupled plasma-mass spectrometry
PGM	Porous glass membrane
GED	Gas exchange device
GC-MS	Gas chromatography-mass spectrometry
MOBCAL	A software to calculate mobilities
EPR	Enhanced permeation and retention
(SH)-PEG	(Thiolated)-Polyethyleneglycol
PBS	Phosphate buffered saline
DMEM	Dulbecco's modified eagle's medium
DI	Deionized water
PSD	Particle size distribution
XPS	X-ray photoelectron spectroscopy
MUA	Mercaptoundecanoic acid
LOD	Limit of detection
AmAc	Ammonium acetate

FWHM	Full width at half maximum
Ppb	Parts per billion
Ppm	Parts per million
GNRs	Gold nanorods
SPR	Surface plasmon resonance
LSPR	Longitudinal surface plasmon resonance
AR	Aspect ratio
PTA	Phosphotungstic acid
UAc	Uranyl acetate
RP-HPLC	Reverse phase-high performance liquid chromatography
PA	Projection area method

Nomenclature

Z_p	Ion mobility
v_{drift}	Drift velocity
E	Electrical Field
C_c	Cunningham slip factor
μ	Viscosity of carrier gas
$d_p, d_m, d_{m,a}, d_{m,r}$	Electrical mobility diameter
e	Elementary electric charge
Q_a	Aerosol flowrate
Q_s	Sheath flowrate
R_{out}	Radii of outer electrode of DMA
R_{in}	Radii of inner electrode of DMA
L	Length of DMA classifier
V	Applied voltage
ΔZ_p	Observed ranges of mobilities of transmitted particles at Z_p
$\sigma_{Pt^{II}}$	Pt^{II} loading
$I_{Pt(CPS)}$	Intensity of platinum detected by ICP-MS
$I_{Au(CPS)}$	Intensity of gold detected by ICP-MS
α_{Au-Pt}	Calibration factor (sensitivity ratio of ^{197}Au to ^{195}Pt)
S_{AuNP}	Surface area of a single gold nanoparticle
V_{AuNP}, V_r	Volume of of gold nanoparticle, gold nanorod
$M_{m,Au}$	Molar mass of gold
ρ_{Au}	Density of gold
N_{av}	Avogadro's number
σ_{SH-PEG}	Packing density of SH-PEG
$\langle X^2 \rangle^{0.5}$	Random walk radius
$C_{Pt^{II}}$	Concentration of Pt^{II}
N_n	Number of n-oligomer particles
α_{Au}	Sensitivity factor for ^{197}Au
Ψ	Function of α_{Au} , ρ_{Au} and V_{AuNP}
DA	Degree of agglomeration
$I_{Au,n}$	Intensity of n-oligomer of gold nanoparticles
$I_{particle}$	Intensity of a single particle event
I	Average intensity (background + particle event)
n	Threshold multiplier
σ	Standard deviation of the average intensity
$d_{m,t}$	Electrical mobility diameter selected at DMA scanning time t
$d_{m,0}$	Initial stepped mobility diameter at t_0
t_{step}	DMA step time
$d_{m,step}$	Mobility step size by DMA
$t_{transit}$	Transit time from outlet of DMA to ICP-MS detector
$N_{spICP-MS}$	Total number of particles detected by spICP-MS
N_{raw}	Number of particles detected at each mobility size d_m
α_c	Probability that a particle is singly charged

$d_{m,max}$	Upper mobility size limit defining a peak
$d_{m,min}$	Lower mobility size limit defining a peak
[NP]	Nanoparticle concentration in solution
η_{ICPMS}	Transfer efficiency for ICP-MS
η_{DMA}	Transfer efficiency for DMA
η_{ES}	Transfer efficiency for ES
k	$\eta_{ICPMS} \times \eta_{DMA} \times \eta_{ES}$
ρ_a	Mobility-based apparent density
m_a, m_r	Mass of NP/aggregate, nanorod
I_a, I_r	spICP-MS intensity for NP/aggregate, nanorod
d_r	Diameter of gold nanorod
L_r	Length of gold nanorod
Δd_{gas}	Infinite diameter of bath gas molecule in DMA
t_{dwell}	Dwell time for spICP-MS
Δr	Layer thickness formed by non-volatile species
$d_{m,s}$	Mobility diameter of non-volatile species
Δd_{layer}	Thickness of layer on gold nanorod
CE	Combined error
d_{vol}	Volume based diameter
$V_{mobility}$	Volume calculated based on mobility diameter
v	Volume obtained by spICP-MS
λ	Theoretical parameter representing mean number of particles per electrospray droplet
V_d	Electrospray droplet volume
C_p	Analyte number concentration
A	Averaged cross section

List of Tables

Table 1.1. Properties to characterize nanomaterials in media (stock solution) proposed by a range of authors.....	5
Table 2.1. Gas exchange device (GED) settings.....	19
Table 3.1. Mean hydrodynamic size by DLS for AuNP-dendron-SH-PEG conjugates in water medium with one standard deviation reported from 5 replicate measurements.....	40
Table 4.1. Mobility size measurement of AuNPs.....	61
Table 5.1. Characterization of GNRs by TEM.....	96
Table 5.2. Geometries for GNRs provided by vendor (TEM).....	96
Table 5.3: Contribution of non-volatiles from ES to layer thickness (nm).....	101
Table 6.1. Simulation of mobility size by MOBCAL.....	123

List of Figures

Figure 1.1. Nanotechnology related submissions by CDER, 2012.....	2
Figure 1.2. Eight generally accepted consumer goods categories loosely based on publicly available consumer product classification system.....	4
Figure 2.1. Configuration of DMA.....	13
Figure 2.2. Configuration of ICP-MS.....	15
Figure 2.3. ICP-MS response to dissolved metal ions and nanoparticles (TRA mode).....	17
Figure 2.4. Improved gas exchange efficiency for new design of GED.....	20
Figure 2.5. Configuration of DMA-ICP-MS hyphenation.....	21
Figure 3.1. Cartoon depiction of conjugation and complexation steps in processing of AuNP-(dendron), AuNP-(dendron)-(SH-PEG) and Pt ^{II} complexed products.....	30
Figure 3.2. (a) The effect of centrifuge cleaning step on Pt ^{II} loading ($\sigma_{Pt^{II}}$) after each round of cleaning, and (b) the effect of reaction time on Pt ^{II} loading.....	32
Figure 3.3. Sensitivity calibration curve for (a) ¹⁹⁷ Au and (b) ¹⁹⁵ Pt by ICP-MS.....	35
Figure 3.4. Surface conjugation of SH-PEG and dendron on AuNPs.....	38
Figure 3.5. Mobility size distributions for (a) AuNP-(dendron)-(SH-PEG1K) and (b) AuNP-(dendron)-(SH-PEG10K).....	39
Figure 3.6. (a) Schematic illustration of the two-layer core-shell model used to quantify SH-PEG packing density used for Eq. (3.2). (b) Adsorption isotherm for SH-PEG on AuNP-dendron conjugates. (c) Citrate AuNP conjugated with SH-PEG 1K, 5K and 10K, at SH-PEG concentration of 0.42 mmol/L during reaction.....	44
Figure 3.7. Quantification of Pt ^{II} loading by ES-DMA-ICP-MS.....	47
Figure 3.8. Uncertainty examination for $\sigma_{Pt^{II}}$	48
Figure 3.9. Mobility size resolved-intensity (¹⁹⁷ Au) distribution.....	49
Figure 3.10. Quantifying colloidal stability using ES-DMA-ICP-MS.....	53
Figure 3.11. Pt ^{II} release under (a) PBS and (2) PH 5 (acetate buffer).....	55
Figure 4.1. A mixture of AuNPs containing 30 nm, 40 nm, 60 nm, 80 nm and 100 nm. The DMA selects, with increasing time, 20 nm, 35 nm, 50 nm, 65 nm, 80 nm and 95 nm and with a DMA step time of 151 s at each selected size.....	62
Figure 4.2. NP transit time from DMA to ICP-MS obtained by moderating voltage from the power supply; ¹⁹⁷ Au signal is recorded with respect to time.....	65
Figure 4.3. spICP-MS intensity spectrum as a function of DMA scanning time for 60 nm AuNPs.....	68
Figure 4.4. (a) Number concentration calibration curve (60 nm AuNP). (b) Mass calibration curve based on AuNPs of various sizes (30 nm, 60 nm, and 40 nm, 80 nm and 100 nm AuNPs). Au mass per NP was calculated based on DMA mobility	

equivalent spherical size. (c) Comparison of PSD for 60 nm AuNPs measured by DMA-spICP-MS and other conventional methods: Method-1: by summation of particle spikes over each DMA step by DMA-spICP-MS; Method-2: by single particle event intensity from DMA-spICP-MS; Method-3: by conventional DMA-CPC; Method-4: by single particle event intensity from conventional stand-alone spICP-MS.....73

Figure 4.5. (a) Plot of size, $\text{mass}^{1/3}$ (i.e., $(^{197}\text{Au intensity})^{1/3}$) and concentration (frequency of NPs) for mixtures containing five sizes of AuNPs as obtained by ES-DMA-spICP-MS. (b) Comparison between measured and known NP concentration initially mixed for five different sizes.....77

Figure 4.6. Heat map showing aggregation of 40 nm AuNPs occurring over 9 d ((a). day 1 and (b). day 9); ^{197}Au intensity was normalized to that of the first monomer peak. (c) Comparison of discrete aggregates with the expected results for a mixture of solid spheres.....80

Figure 4.7. Observation of higher aggregates at low concentration for day 9 aggregation; size axis begins at 70 nm. The color scale was reduced so that three distinct peaks are observable (i.e., the aggregates on day 9).....81

Figure 4.8. Heat maps for mobility-based apparent density: (a) NP mixtures containing 30 nm, 40 nm, 60 nm, 80 nm and 100 nm AuNPs. (b) Aggregates consisting of 40 nm primary AuNPs. The map indicates a small population with apparent density of 40 g cm^{-3} , which we attribute to particle coincidence and that around 4 g cm^{-3} are due to particle splitting.....83

Figure 4.9. Time resolved intensity spectrum for 30 nm AuNPs in medium containing Au^{3+} by both stand-alone spICP-MS and DMA-spICP-MS.....85

Figure 4.10. Particle size distribution for 30 nm AuNP in medium containing Au^{3+} measured by both stand-alone spICP-MS and DMA-spICP-MS corresponding to Figure 4.9.....86

Figure 5.1. Procedure to determine mobility diameter ($d_{m,r}$) and volume (v_r) by DMA-spICP-MS method.....93

Figure 5.2. TEM image for GNRs (a) CIT-660 (b) CIT-800 (c) CIT-980 (d) CTAB-600 (e) CTAB-20-850 (f) CTAB-40-850 (g) CTAB-1400.....95

Figure 5.3. Two representative TEM images show evidence for a thin low density adlayer on the surface of GNRs. Both citrate and CTAB coatings were examined: (a) CIT-660 (b) CTAB-40-850.....97

Figure 5.4. Comparison of dilution (D60 stands for 60 times dilution compared with original (as is) solution).....98

Figure 5.5. (a) Layer thickness of all GNRs by electrostatic deposition of peak size selected by DMA. (b) Comparison of number of GNRs sampled (5 vs around 50) on determination of layer thickness for both CTAB and CIT coated sample.....100

Figure 5.6. Mobility size distribution of CIT-600 by ES-DMA-CPC at its original concentration.....101

Figure 5.7. (a) Comparing d_r and L_r determined by DMA-spICP-MS (solid circles) to that obtained by TEM (open circles). (b) Relative error (%) in $d_{m,r}$ and v measured by DMA-spICP-MS in comparison to theoretical calculation based on TEM.....103

Figure 5.8. Robustness analysis of DMA-spICP-MS method.....107

Figure 5.9 (a) Comparison of volume-based d_{vol} and mobility diameter $d_{mobility}$ for mixture of GNRs and gold nano-spheres. (b) L_r , d_r obtained from mixture, individual and that of TEM as benchmark.....109

Figure 5.10. (a) Distinguishing mixtures of gold nanorods and spheres by aspect ratios. Black hollow dots are experimental data ($d_{mobility}$ vs. ρ). Blue line represented theoretical relationship between AR and ρ . (b) Comparison of AR by three different method: (1) AR no layer means deriving AR from theoretical curve as in (a), with assumption of no layer on rods. (2) AR layer means deriving AR from geometry obtained from figure 5.9(b) (i.e. mix, orange bar). (3) AR TEM is that calculated from geometry measured by TEM.....112

Figure 6.1. (a) Mobility size spectrum for protein particle after buffer exchange at three time points: 0 week (right after buffer exchange), 1 week, and 2 weeks. Samples were diluted 10 times right before conducting DMA experiment. (b) Mobility spectrum comparing different dilutions (i.e. 100 \times vs. 10 \times). No droplet induced aggregation was observed at that of 10 \times concentration.....118

Figure 6.2. (a) PTA was used as stain for protein particles in solution. (b) UAc was used as stain for protein particles in solution. (c) Carbon grid by UAc staining for electrospray deposited protein particles. (d) Silicon monoxide-formvar grid by UAc staining for electrospray deposited protein particles.....120

Figure 6.3. (a) Staining TEM for protein particles collected after electrospray and zoom-in (b) Staining TEM for particles from solution (c) Geometries comparison of L and d for a hatpin-shaped rods forming protein particles (i.e. from electrospray and solution, summarized from TEM measurement).....122

Chapter 1: Introduction and Overview

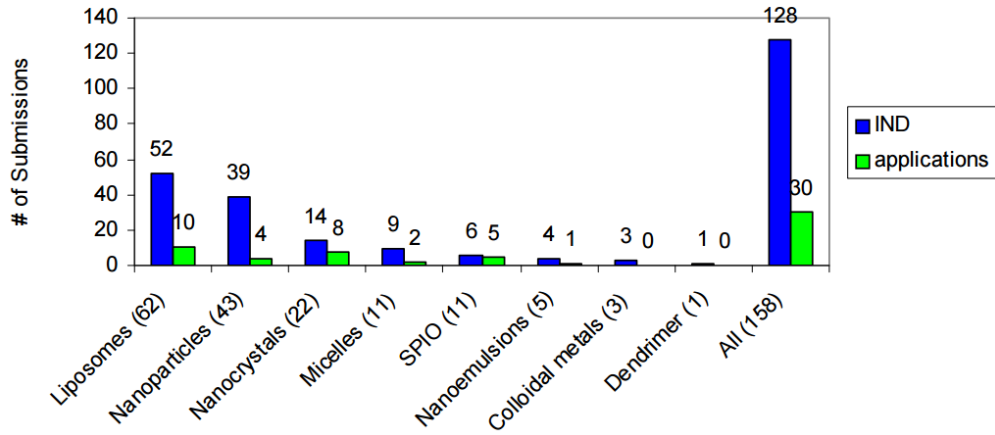
1.1 Nanotechnology, Characterization and Challenges.

Nanotechnology is defined by ASTM as “a term referring to a wide range of technologies that measure, manipulate, or incorporate materials and/or features with at least one dimension between approximately 1 and 100 nanometers (nm)”. [1] Because of the size, and the change in surface-to-volume ratio, nanomaterials show unique physio-chemical properties compared with their corresponding bulk materials including improved conductivity, strength, reactivity, as well as electrical, optical and catalytic properties. [2] Engineered nanomaterials are being manufactured in wide range of product applications including medicines, catalysts, electronics, renewable energy and environmental protection. [2, 3]

Nanomedicine for example, is an emerging field which used nanomaterials to improve diagnosis, prevention and treatment of disease. Distinct physicochemical properties of nanomaterials are critically relevant to particular physiological interactions, which provide benefits in medical applications including improving efficacy, reducing side effects, and assisting in prevention and treatment. [4, 5, 6, 7, 8] According to Center for Drug Evaluation and Research (CDER) internal database, nanotechnology related drug submissions to FDA in year 2012 was demonstrated in Figure 1.1. [9] The platform includes but are not limited to liposomes, nanocrystals, nanoemulsions, dendrimers, metal oxides (superparamagnetic iron oxide, titanium dioxide, zinc oxide), gold and

silver nanoparticles. Among the total 158 submissions, the majority are liposome (39.2%) and nanoparticle (27.2%) based platforms.

(a)



(b)

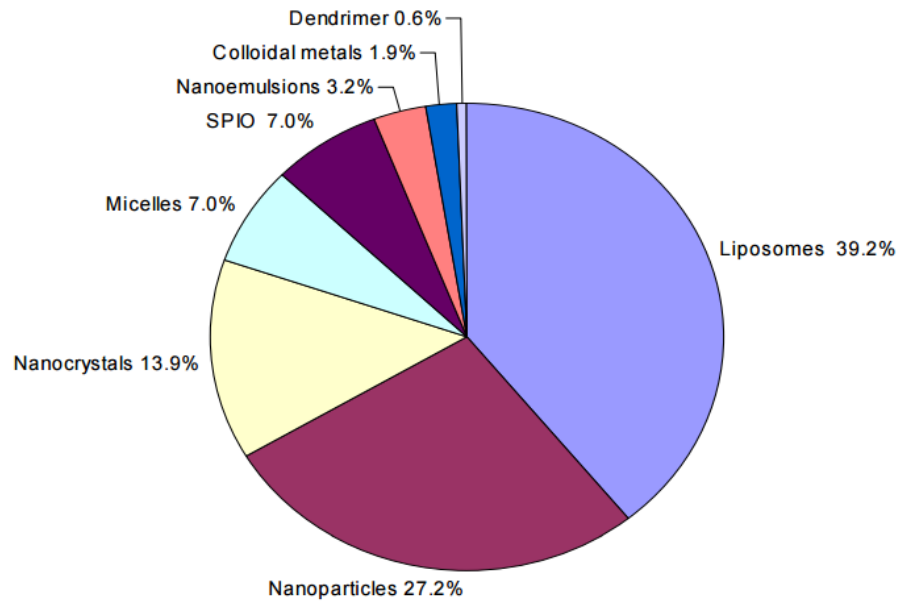


Figure 1.1. Nanotechnology related submissions by CDER, 2012.[⁹]

The Nanotechnology Risk Assessment Working Group was established in 2011 to assess possible risks associated with the application of nanotechnology in the development and manufacturing of drug products. They proposed in an Ishikawa diagram factors such as particle size, particle aggregation state could ultimately impact the quality, safety and efficacy of drug product containing nano-sized APIs during ingesting and dissolution. [10] Wide ranges of researches has discussed factors such as size, shape, surface property, composition, purity, stability and interaction with biological environments will influence the cellular uptake, circulation, bio distribution, toxicity etc. [11, 12, 13, 14, 15, 16, 17, 18, 19, 20, 21]

Aside from nanomedicine, increasing production of nanomaterial-containing commercial products, and their disposal raised concerns for nature environment. From updated Nanotechnology Consumer Products Inventory (CPI) released in October 2013, 1814 consumer products were listed from 622 companies in 32 countries, the major category listed in Figure 1.2. Health and Fitness category includes the largest listing of products (i.e. 42%). [22] Any potential deleterious effects of the huge quantity of disposed nanomaterials therefore need to be assessed in order to understand environmental impacts and potential effects on human health. Such work will required the linking of physicochemical characteristics of nanoparticles to their biological behavior. There is still debate regarding the key essential characterization information required for hazard identification purpose. According to several studies highlighted in Table 1.1, although there is slight variability amongst authors, the selection of characterization were with the priority given to surface area, surface chemistry, shape, morphology as well as material composition/purity. [23, 24, 25, 26, 27, 28, 29] Discussion held

by NanoImpactNet workshop I Zurich, 2008, (NanoImpactNet is funded under European Commission FP7(CSA-CA218539)), with a group of 42 researchers (consisting mainly ecotoxicologists, environmental chemists, material scientists, as well as toxicologists, risk assessors, and industrial stake holders) discussed and concluded six main properties to be characterized for nanomaterials investigated in environmental and ecotoxicology studies including aggregation / agglomeration / dispersibility, size, dissolution, surface area, surface charge, surface composition/surface chemistry. [23]

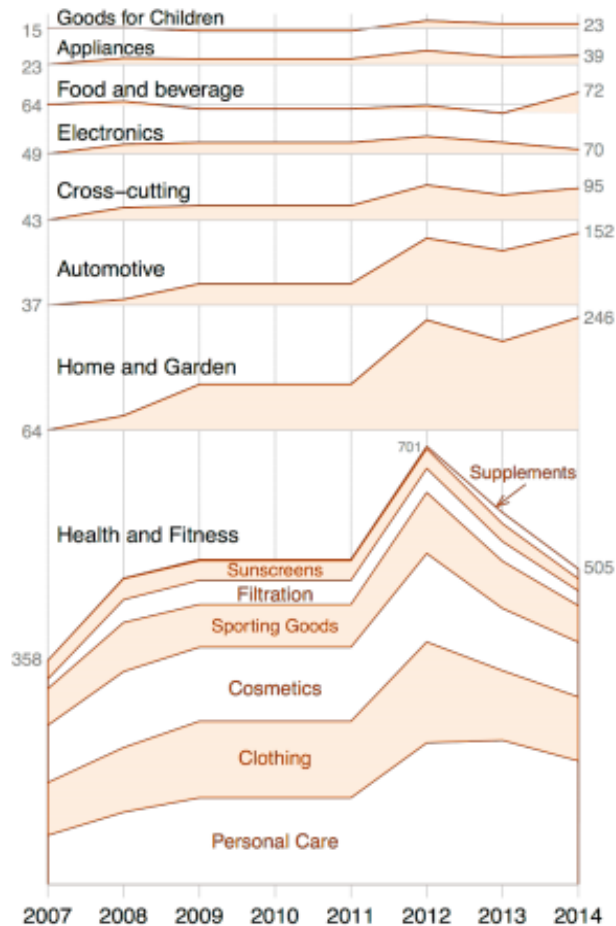


Figure 1.2. Eight generally accepted consumer goods categories loosely based on publicly available consumer product classification system. [22]

Table 1.1. Properties to characterize nanomaterials in media (stock solution) proposed by a range of authors. [23]

Property	Oberdorster et al. (2005)	Powers et al. (2006, 2007)	Thomas et al. (2006)	Warheit (2008)	Klaine et al. (2008)
Size distribution	*	**	**	**	**
Agglomeration state/dispersion	*	**	*	**	*
Crystal structure	*	*	*	**	
Chemical composition	*	*	*		**
Surface area and Porosity	*	**	*	**	**
Surface chemistry		**	*	**	*
Surface charge		*	*	**	*
Shape and morphology		**	**		*
Dissolution/Solubility		*	*		**
Physical/chemical properties (purity)		**		**	
Methods of synthesis				**	

*: Of importance; **: Priority.

The many facets of nanomaterials as discussed above, making the characterization far more complex compared with conventional analytes. Engineered nanoparticles in a complex matrix, at realistic concentration are two of the major challenges for analytical scientist. A number of common techniques becomes unfeasible when moving to trace level. Even though pre-sample preparation could assist in removing interfering matrix, sample preparation itself could induce artifacts and alter the original property. Sample preparing would also complicate the measurement process and add uncertainties which

need to be addressed by development of standard protocols. Potential transformation of pristine engineered nanomaterials when put in contact with either biological media or environmental media is another major challenge. This includes change of aggregation states (both homoaggregation and heteroaggregation), interaction with other species, surface modification, and nanoparticle dissolution. It is recommended to use a range of complementary tools existing, and combine in such a way that data can be validated. There is also a need to allow simultaneous determination of many different physicochemical properties real-time by hyphenated techniques.

1.2 Current tools in nanoparticle characterization

There are a lot of different instruments and characterization techniques for the different aspects of nanoparticle properties. The commonly used techniques discussed herein include the capability relevant to the following properties: particle size/size distribution, aggregation states, nanoparticle composition, concentration, and surface chemistry. Advantages and limitations are briefly discussed.

The most frequently used tools for the visualization of engineered nanoparticles are electron microscopes (EM). Both SEM and TEM have the capability to reveal the size, shape, heterogeneity of nanomaterials as well as the degrees of aggregation and dispersion in complex matrixes. [30, 31, 32, 33, 34] EM has been successful applied to characterize TiO₂ nanoparticles in soils amended with sewage sludge [35] and biosolids. [36] When coupled with energy dispersive X-ray spectroscopy (EDS), it permits a clear determination of the composition of elements heavier than oxygen with quantitative analysis (~20% uncertainty). [37] TEM can also couple with electron energy loss

spectroscopy (EELS) from which elements can be discriminated (10% uncertainty). [37] Staining is often used to measure inorganic species under TEM. [38] There are some limitations of EM methods: specimens can be damaged or even destroyed by intense high voltage electron beams prohibiting its subsequent analysis by other modalities. It is time-consuming to sample enough particles to generate good statistics and reliable data.

Dynamic light scattering (DLS) is the most commonly employed high-throughput technique to measure nanoparticle size in aqueous suspensions. [8, 39] Its analysis is fast (in minutes), convenient, noninvasive to samples with sufficient accuracy in determining the hydrodynamic size of monodisperse samples. [4] However the analysis of polydispersed samples or samples in complex medium would be difficult by DLS. It is incapable to detect the presence of smaller particles among bigger ones due to the fact that scattering intensity depends by the sixth power of the particle diameter. [31] Direct coupling to size separation technique like field flow fractionation (FFF) and hydrodynamic chromatography (HDC) may overcome polydispersity problems and the presence of interfering particles by delivering narrow size fractions to DLS detector. Another drawback of DLS techniques is that it requires information of viscosity and refractive index which is not available or difficult to know for sample that are highly complex. [30]

Nanoparticle tracking analysis (NTA) is an emerging light scattering technique in which video microscopy is used to measure the movement of particles under Brownian motion and their hydrodynamic diameters are calculated by a modified Stokes-Einstein equation. [40] NTA has high sensitivity for particle number concentration, provides

reliable size distributions in the presence of aggregates. Comparing to microscopy techniques, NTA is capable of measuring large number of individual particles in less time. It is not suitable for particles with hydrodynamic diameters below 20nm due to laser power and camera detector. [30]

Fourier transform infrared (FTIR) spectroscopy is commonly employed to use the expression of characteristic spectral bands to reveal information for nanomaterial-biomolecule conjugation or functional molecules grafted to nanomaterials. [12, 41, 42] Attenuated total reflection (ATR) FTIR, a recently developed technique, utilizes the property of total internal reflection in conjunction with IR spectroscopy to probe structure of absorbed species at interface. [43] It can be used to investigate surface features, however it is not very sensitive surface analysis method at nanometer scale because of the penetration depth of ATR-FTIR. [4, 44] Thermogravimetry in combination with mass spectrometry (TGA-MS) can be used for surface analysis, in which surface molecules are removed by heating whose composition are then analyzed by MS. Plot of weight loss with temperature characterizes thermal decomposition of the surface molecules. [45]

In terms of elemental compositional analysis, atomic spectrometry techniques like electrothermal atomic absorption spectroscopy (ET-AAS), inductively coupled plasma optical emission spectrometry (ICP-OES), inductively coupled plasma mass spectrometry (ICP-MS) can be used for sensitive detection of elements, as well as for quantification. [46] ICP-MS is the most commonly used technique because of low detection limits attainable down to ng / L. ICP-OES is in the $\mu\text{g} / \text{L}$ range. ET-AAS offers half-way performance in between. They are not capable of distinguishing the

physiochemical form of the element (dissolved vs particulate) or any other related information (size and aggregation). [30] These limitations can be overcome by combining with some other on-line continuous separation techniques (FFF and HDC). Single particle ICP-MS is another emerging branch in ICPMS which provides both size, and concentration information. Details will be discussed in next section. Field flow fractionation (FFF) is a family of separation techniques, and the optimization of operating conditions is needed for each type of sample. Uncontrolled particle membrane interaction and low recoveries are major disadvantages of the technique. [30] In hydrodynamic chromatography (HDC), the separation occurs due to streamlines of flow applied to a column packed with nonporous beads. Particles with bigger hydrodynamic diameter elute earlier than smaller particles due to velocity gradient, which results in broad separation ranges of sizes, yet poor resolution. Effect of coating surface on elution time is another issue. [47]

On-line hyphenated techniques combining size separation with subsequent detection which provide multi-dimensional information is promising. This can pre-sort complex samples by fractionation and simplify subsequent detection. This dissertation focuses on developing and extending the application of novel hyphenated instruments composing primarily ion mobility analysis (i.e. DMA) and ICP-MS achieving high resolution on-line size classification and elemental detection. Method validation were applied to nanoparticles characterization for biomedical and environmental application. We would like to illustrate how this novel hyphenated instrument fit in the big picture of nanoparticle characterization and contribute as a complementary tool among all the others.

Chapter 2: Instrumentation

2.1 Differential Mobility Analyzer (DMA)

DMA is an important instrument to classify nanoparticles (NP) based on ion mobility.

The electrical ion mobility of a particle Z_p is defined as:

$$Z_p = \frac{v_{drift}}{E} \quad (2.1)$$

Where v_{drift} is the drift velocity of a charge NP under the electric field with magnitude E . By balancing electric and drag forces on the particle with charge n , electrical mobility is also given by:

$$Z_p = \frac{neC_c(d_p)}{3\pi\mu d_p} \quad (2.2)$$

Where C_c (a function of d_p) is the Cunningham slip factor, which corrects for non-slip boundary condition. ^[48] μ is the viscosity of the carrier gas, d_p is the electrical mobility diameter and e is the elementary electric charge. For a spherical NP with $1e$, d_p is equal to the geometric diameter, while for non-spherical NP, d_p is the equivalent diameter of a sphere having the same drag force. ^[49]

The configuration of a cylindrical DMA consists of two concentric electrodes with inner electrode held at controlled high voltage V and outer electrode grounded (Figure 2.1). Therefore, an electrical field is generated between the two electrodes. A flow of polydispersed aerosol (called aerosol flow, Q_a) and a laminar sheath flow (Q_s) enter the DMA at the top inlet. Both the two flows pass down the annulus with no mixing and maintain a laminar flow. The charged particles are attracted towards the inner electrode

due to the electrical force while being carried by the sheath flow down the DMA column. At a fixed flowrate and DMA configuration, the mobility is strictly a function of applied voltage, and particles of a given mobility (Z_p) are selected by controlling the voltage and exit the DMA slit.

$$Z_p = \frac{Q_s \ln(R_{out}/R_{in})}{2\pi VL} \quad (2.3)$$

Where R_{out} and R_{in} are the radii of outer and inner electrode, L is the length of DMA classifier, V is the applied voltage. When certain mobility was selected, the mobility diameter is determined by Eq. (2.2). For non-spherical nanoparticle, mobility is a function of both particle shape and its orientation. (i.e. drag force dependent on orientation). Therefore, orientation-dependent mobility could theoretically provide information on particle shape. Kousaka et al. measured the dynamic shape factor for doublets of uniform polystyrene spheres and the dependence of orientation on electrical field and size of doublets were pointed out. [50] Based upon a scalar expression of drag force, the length of carbon nanotubes were measured by Kim et al. [51] Li et al. developed an orientation-averaged mobility theory for rigid axisymmetric particles as well as extended to any non-spherical shape, based upon which, geometric shape information can be obtained from experimental measurement at various electric fields. [52, 53, 54]

The resolution of DMA is defined by:

$$R = \frac{Z_p}{\Delta Z_p} \quad (2.4)$$

Where ΔZ_p is observed ranges of mobilities of transmitted particles selected at Z_p . The resolution of DMA is determined by the ratio of Q_s to Q_a . Most commercial DMAs

have poor transmission and resolving power at particle sizes below 5nm. [55] The performance of transmission and resolution of most DMAs are limited due to Brownian diffusivity and imperfect instrument concentricity. Nonetheless, extensive researches have been done to resolve the issue by increasing Reynolds number of laminar operation of sheath flow in DMA to values as large as possible. [56, 57] Optimizing geometrical design by using an axial distance L between inlet and outlet aerosol slits comparable to the inter electrode distance was also helpful. [58] So far, many nano-DMAs has been developed in which resolution achieved as high as a peak full width at half height (FWHH) $\sim 1.5\%$ for $\sim 1\text{nm}$ by operating Reynolds number at 3×10^4 . [55] Many new designs of DMA to achieve better performance include but are not limited to, high resolution and sensitivity capable of providing structural information, [59] classification of particles in 1-3 nm range with improved penetration efficiency and sizing resolution, [60] hand-held designs [61] and lightweight designs. [62]

Compared with many liquid-based fractionation methods or chromatographic separations, DMA offers flexibility in operation: enabling an arbitrarily chosen mobility size for a pre-determined time by choosing voltage and DMA step time accordingly. In addition, if operated at fixed voltage, DMA operates as a band filter to allow one specific size of NPs to exit. There is no need to optimize separation conditions for different types of samples which many liquid fractionation techniques require. The separation principle is straightforward as described above, and therefore there is no need to tune operation for different types of samples.

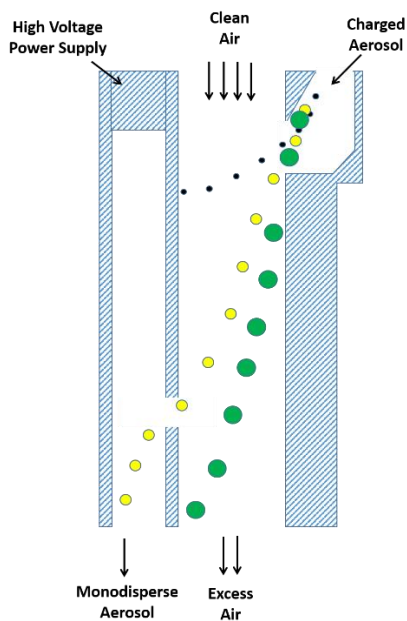


Figure 2.1 Configuration of DMA.

Electrospray (ES) is usually integrated with DMA to generate aerosols from colloidal suspension. The major advantage of using ES is that it generates well-controlled, monodisperse and sub-micrometer droplets containing a single particle per droplet by pushing analyte solutions through a fused silica capillary under pressure. Voltage applied at the tip of capillary enables generation of charged, fine and monodisperse droplets by Coulombic repulsion. Droplets containing analytes are mixed with carrier gas (air, sometimes also supplemented with CO₂), evaporate and obtain equilibrium charges in a 210-Po neutralizer (usually amount in ES device) which charge distribution is known. Most of aerosols will have +1, 0, -1 charges. Although only charged particles are size selected by downstream DMA, with a known Boltzmann charge distribution, the original population is obtainable. For ES, two types of fused silica capillaries (diameter of 25 μm and 40 μm) are usually used. Under a pressure of

3.7 psi, the flowrate from ES is on the order of ~100 nL/min. A buffer used extensively for ES is 2-20mM ammonium acetate at a wide range of conductivities, with 0.2S/m typically used. The sample volume is 30µl to 2mL at concentrations of 10^{10} to 10^{13} particles/ml. Higher concentrations above $\sim 10^{14}$ particles/mL risk the effect of droplet induced aggregation where artifact aggregation was formed from ES process. [63, 64] This usually should be avoided when conducting experiment for better interpretation data.

Condensation Particle Counter (CPC) is a most commonly used detector for ES-DMA. For particles smaller than 0.2 micrometer, direct detection by optical technique is not feasible. CPC works by condensing saturated butanol or water vapor on particles to grow to a size of about 10 micrometers. The concentration of NPs is then measured by corresponding scattering intensity detected by photodetector. CPC is a thousand times more sensitive than commercially available electrometers. NP samples classified by DMA can be deposited on TEM grid for further measurement by electrostatic deposition chamber. [65] Particles classified after ES-DMA have been demonstrated to be able to deposited directly into live cell culture if care is taken to preserve the viability of cells within a thick liquid layer. [66] Confirmation of viability of virus particles was conducted following electrospray by bubbling DMA output through a liquid solution. [67, 68, 69] Detailed reviews of ES-DMA applied to bio nanoparticles, as well as to characterization of nanoscale biomaterials relevant to disease diagnosis, treatment and pharmaceutical manufacturing could be found in references. [70, 71]

2.2 Inductively Coupled Plasma Mass Spectrometry (ICP-MS)

2.2.1 Components of ICP-MS Instrument

ICP-MS is a multicomponent elemental determination technique at ultra-trace level (as low as parts per trillion (ppt)). ICP-MS designs share similar components, such as nebulizer, spray chamber, plasma torch, interface, ion focusing system, mass separation device, vacuum chamber and detector.^[72] (Figure 2.2). The sample usually in liquid form is pumped through a peristaltic pump into a nebulizer and converted to fine droplets of aerosol by argon gas (~1L/min). Droplets containing analytes enter the plasma (~10,000K), evaporate, with analytes further atomized and ionized. Ions are then extracted and directed to the mass spectrometer via interface region and electrostatic lenses and separated by mass to charge ratio. There are four types of commonly used mass spectrometers (quadrupole, magnetic sector, time of flight, and collision/reaction cell). Finally, the selected ions are detected by the detector where ions are converted to an electrical signal.

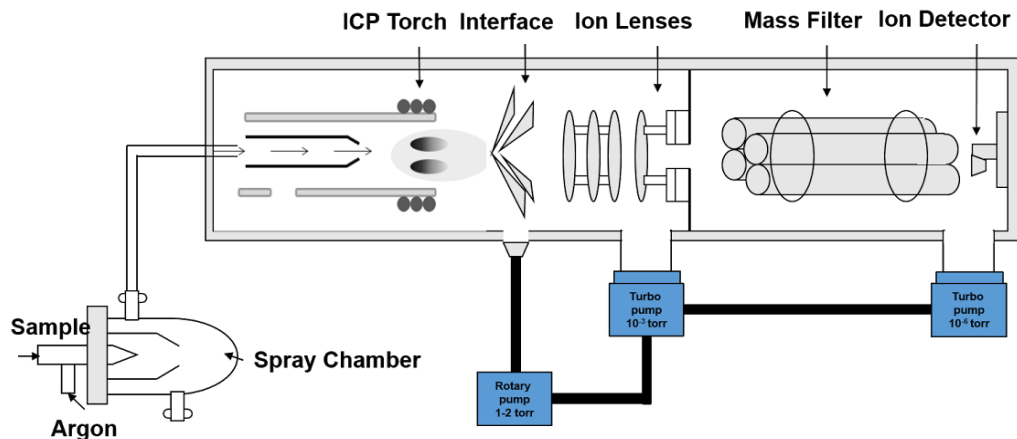


Figure 2.2 Configuration of ICP-MS. Figure adapted from reference. ^[72]

2.2.2 Single particle ICP-MS

When ICP-MS was operated in time resolved analysis (TRA) mode, the signals are monitored with respect to time. For dissolved analytes, regardless of concentration and dwell time, steady and continuous signals are produced as a function of monitor time. In contrast, if the analyte is NP and at sufficiently low concentrations and appropriate dwell time, pulse signal representing each particle event will be presented (Figure 2.3). [73] We call this specific operation condition single particle ICP-MS (spICP-MS). In this case, the frequency of the pulses is directly proportional to number concentration and the intensity of the pulse is proportional to the mass of the particle. spICP-MS can provide information about elemental composition, number concentration, and mass. Size information can be extracted if composition, shape is known as priori. Although it is a relatively emergent technology, the application of spICP-MS covers different fields for nanoanalysis including, but not limited to detection and quantification of NPs in environmental relevant concentrations, size distribution and stability studies, as well as NP migration and dissolution from matrixes. [74]

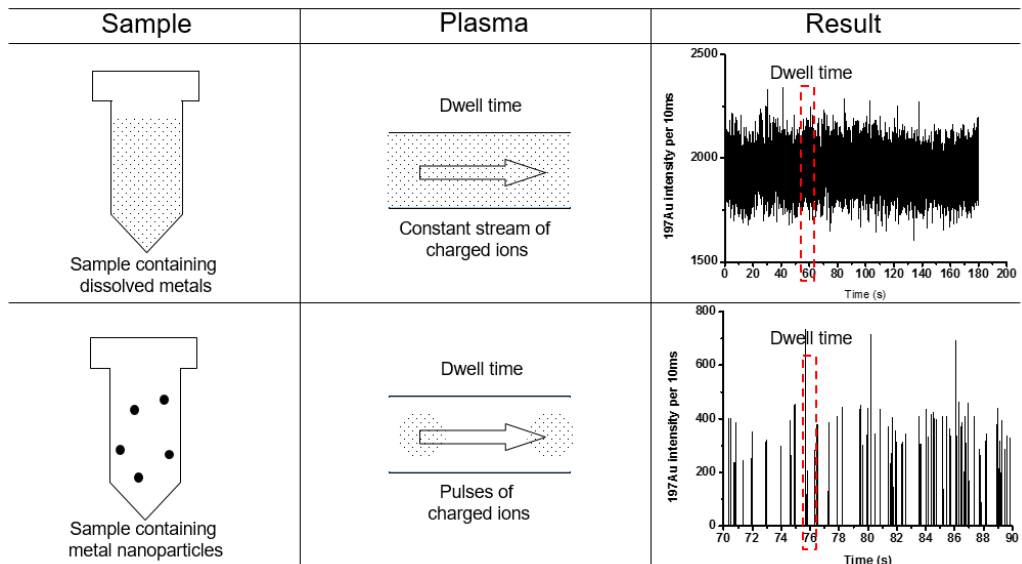


Figure 2.3 ICP-MS response to dissolved metal ions and nanoparticles (TRA mode).

Figures adapted from reference. [73]

2.3 Hyphenation of ES-DMA-ICP-MS

2.3.1 Incompatibility issue from ES-DMA-ICP-MS.

By combining DMA with ICP-MS, real-time size resolved compositional analysis is thus achieved taking advantage of both high size resolution from DMA and ultra-sensitive elemental detection by ICP-MS. Direct hyphenation of DMA with ICP-MS has been demonstrated to monitor aerosol particles of lead nitrate generated from nebulizer as aerosolizing source. [75] When it comes to using ES as the aerosol generator, the issue of incompatibility of air with ICP-MS becomes a challenge. Air is a conventional gas used for electrospray process and it is extremely difficult to achieve stable ES condition in Ar atmosphere. The reason for this is the occurrence of electrical breakdown of Ar when voltages of ~2-5 kv are applied to the electrospray source. On

the other hand, argon plasma is difficult to ignite and sustain in the presence of even moderate levels of air. [76] This incompatibility has been partially addressed through using DMA itself as a gas exchange converter by operating in argon sheathflow. [75,76] There is need to operate DMA at high sheathflow to serve as effective gas converter, which significantly limits the upper operational size.

2.3.2 Design of Gas Exchange Device (GED)

Nishiguchi et al. introduced design of gas converter apparatus to efficiently exchange molecules in air to argon. This design enables direct and real time multielement monitoring of airborne particulate matter from outdoor sample.[77] Based on this concept. Elzey et al. designed a gas exchange device installed prior to ICP-MS, therefore affording flexibility in operational size ranges for ES-DMA-ICP-MS system. [78] A porous $\text{Al}_2\text{O}_3\text{-SiO}_2$ glass membrane (PGM, from SPG Technology Co., Ltd., Japan) is housed in a custom-made Pyrex glass tube. The performance of GED in terms of gas exchange efficiency and particle transport through GED were systemically investigated. [79] I optimized the design of GED by incorporating longer lengths of PGM membrane, by reducing diameter of outside glass tube as well as change of flow from co-current to counter-current. The settings and parameters are listed in Table 2.1

Table 2.1. Gas exchange device (GED) settings

GED Parameters	Values
Length of GED outer tube	90 cm
Diameter of GED outer tube	1.3 cm
Argon flow rates	3 L/min
Sample flow rates	1 L/min
Length of PGM	60 cm
Pore size of PGM	100 nm
Inner diameter of PGM	0.42 cm
Outer diameter of PGM	0.5 cm

In my design, sample flows inside membrane and argon gas flows outside membrane in a counter-current pattern. Due to concentration gradient, argon diffuses into membrane to enrich argon content in sample flow, meanwhile air in sample flow diffuses out of membrane and exits the GED device. The overall gas exchange efficiency was improved (Figure 2.4) for the new GED design and achieved around 90% for an argon gas flow of 4 L/min.

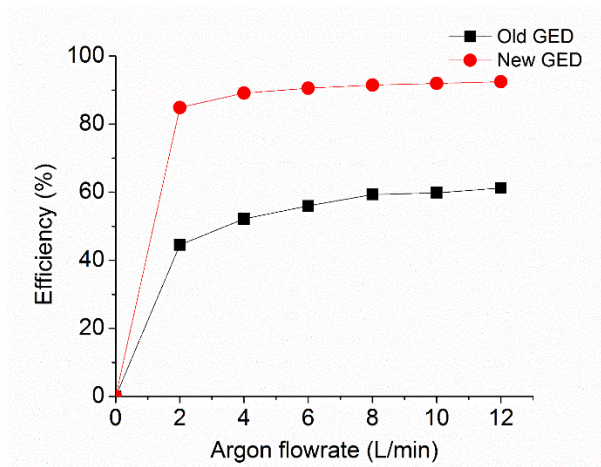


Figure 2.4 Improved gas exchange efficiency for new design of GED. Efficiency vs. argon flow was evaluated (with sample flowrate of 1.1 L/min).

2.3.3 Schematic of DMA-ICP-MS Hyphenation

A schematic of DMA-ICP-MS is shown in Figure 2.5, and is composed of four major components: ((a)-(b)) ES and neutralizer for aerosolizing colloidal nanoparticles, (c) DMA for particle mobility classification, (d) a gas exchange device (GED) to exchange air to ICP compatible argon and (e) the ICP-MS for elemental-specific particle counting and mass quantification. The ES-DMA was coupled to the ICP-MS via the GED. Specifically, aerosol flow out of DMA is interfaced to the ICP-MS through the GED directly into the plasma (like a GC-MS connection). Conductive silicone tubing (0.31" ID \times 0.5" OD, TSI Inc., Shoreview, MN) is used to couple between devices, with outlet of GED connected to the ball joint at the end of torch via a 12 \times 5 Pyrex glass socket joint.

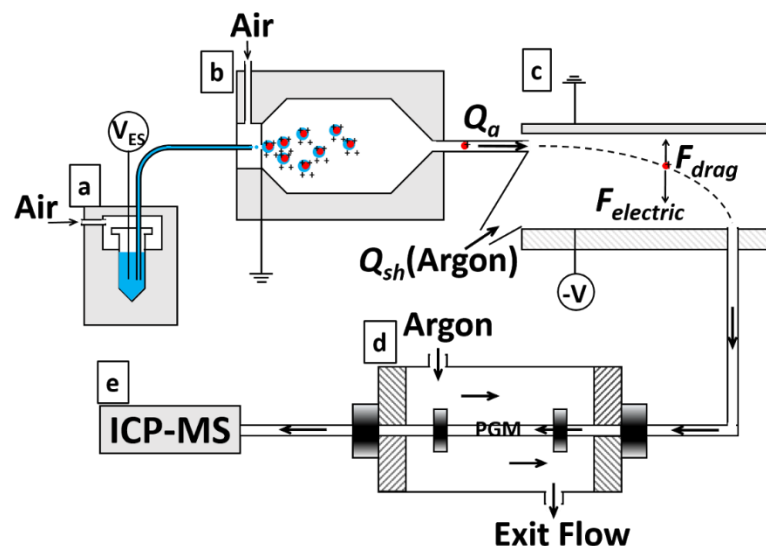


Figure 2.5 Configuration of DMA-ICP-MS hyphenation.

2.4 Scope of the Dissertation

This dissertation focuses on the development of DMA-ICP-MS based methods for characterization and quantification of NPs. In Chapter 3. ES-DMA-ICP-MS was applied to investigate a model anti-tumor drug delivery platform: cisplatin-complexed gold nanoparticles (Pt^{II} -AuNP). On a quantitative basis, surface engineering and its influence in drug payload, stability and release was evaluated. An optimal balance between drug loading and conjugate stability under biologically relevant conditions can be achieved by surface engineering. In addition, by employing quantitative measurements by DMA-ICP-MS, and orthogonal measurement, one can monitor and control properties that determine drug delivery efficacy, and by extension the safety, of nano-based drug delivery platforms.

In Chapter 4. A novel methodology of ICP-MS operating in single particle mode with ES-DMA was demonstrated with the capacity for real-time size, mass and concentration measurement of nanoparticles (NPs) on a particle-to-particle basis. A detection limit of 10^5 NPs mL⁻¹ was determined under current experimental conditions, which is about four orders of magnitude lower in comparison to a traditional ES-DMA setup using a condensation particle counter as principal detector. This technique showed the capability (1) Clearly resolving NP populations from a mixture containing a broad size range; (2) Defining a linear relationship between mobility size and one-third power of ICP-MS intensity for spherical NPs; (3) Monitoring propagation of NP aggregation with well characterized oligomers; and (4) Differentiating aggregated NPs and non-aggregated states based on the “apparent density” derived from both DMA size and spICP-MS mass.

In Chapter 5, based upon the technique developed by Chapter 4. ES-DMA-spICP-MS was applied as a fast and quantitative method for determining the geometries of nanorods (i.e., length and diameter). Seven gold nanorod samples with different geometries (diameters 11.8-38.2 nm, aspect ratios 1.8-6.9) were used to evaluate the method. I demonstrated that DMA-spICP-MS can (1) achieve quantification of both length and diameter with accuracy comparable with TEM analysis, (2) make statistically meaningful measurements in minutes at low concentrations and (3) separate nanorods from spheres to quantify the geometry of each population. A robustness analysis of this method was performed to evaluate this approach.

In Chapter 6, the feasibility of ES-DMA to study soft, high order protein with interesting rosette structure was investigated. The effect of electrospray aerosolization

process on the preservation of protein structure was examined by gas phase ES collection of protein followed by staining TEM. The negative staining procedure was optimized in terms of stain types and grid type. It was demonstrated electrospray is gentle enough to maintain some extent of structure. Particle size distribution representing different protein higher assembly structure measured by ES-DMA was consistent with that of MOBCAL simulation.

In Chapter 7, I concluded the dissertation and discussed future work.

Chapter 3: Polyethylene Glycol Stabilized Gold Nanoparticle Platform for Chemo-Radiation Therapy: Relating Surface Engineering to Performance using Hyphenated ES-DMA-ICP-MS

3.1 Introduction

Since its discovery as an antitumor agent, cisplatin or cis-diamminedichloroplatinum(II) (Pt^{II}), has been applied in the treatment of various solid tumors (e.g., ovarian and testicular cancer, germ cell tumors, and non-small-cell carcinoma) with a cure rate as high as 90 % for testicular cancer. [80, 81, 82, 83, 84] When entering tumor cells, the active Pt drug reacts with DNA to form adducts, inhibits its replication and triggers apoptosis (programmed cell death). The synergistic combination of Pt^{II} and ionizing radiation induces additional damage to DNA, and degrades cell viability through formation of toxic Pt intermediates and inhibition of the DNA repair process. [83]

However, clinical use of Pt^{II} is limited by severe side effects and poor patient compliance, due to nephrotoxicity, severe nausea and vomiting, ototoxicity and neurotoxicity. [85] Indiscriminate uptake of the drug into both normal and cancerous tissue, coupled with rapid clearance and excretion through the kidney, limits the achievable dose delivered to tumor cells. [86]

In this context, NP-based drug delivery systems are a promising avenue to improve targeting and enable high delivered doses, while minimizing the toxic side-effects to healthy tissue. [87, 88] Use of NP delivery platforms may enhance the accumulation of the drug in tumors, minimizing either kidney excretion or uptake by healthy cells, via

the well-documented enhanced permeation and retention (EPR) effect. [89, 90] In other words, by attaching the drug to NPs, its physicochemical properties are modified, leading to altered pharmacokinetics and biodistribution profiles. NPs can also be engineered through surface chemistry to serve multiple functions in addition to drug delivery (e.g., active and passive targeting, avoidance of the reticuloendothelial system, reduced interaction with plasma proteins, imaging of localized drug delivery. [91, 92, 93, 94, 95]

AuNPs are often the platform material of choice for drug delivery, due to their generally non-toxic nature, biocompatibility, facile synthesis and functionalization, and chemical stability. [96, 97, 98] For instance, cytotoxicity in both lung epithelial and colon cancer cell lines, and an unusual ability to penetrate the cell nucleus, have been demonstrated when the chemotherapy drug oxaliplatin (another member of the class of Pt-containing anti-tumor drugs) is complexed with AuNPs. [99] Additionally, AuNPs complexed with Pt-based therapeutics may provide an enhanced radiation therapeutic effect. [100, 101, 102] Lee et al. demonstrated Auger electron emissions from Pt^{II}-AuNP complexes triggered by external ionizing radiation, suggesting its potential as an X-ray absorbing adjuvant agent for chemo-radiation cancer therapy. [102]

Although the Pt^{II}-complexed AuNP vector provides a promising strategy for the use of targeted drug delivery in cancer treatment, one challenge is to accurately engineer this platform on a quantitative basis to achieve optimal therapeutic performance. [103] In terms of efficacy, both drug loading and the stability of the drug vector (i.e., colloidal stability and the stability of active drug under different conditions) are of crucial importance. In this context, an optimized design may ultimately require a balance

between drug loading and stability. The design should also afford rational control facilitated by an understanding of the underlying surface properties.

Pt^{II}-dendron-AuNPs have been identified previously as a promising formulation, where the “dendrimer-like” structures with high uniformity and reactive functional groups provide active sites for Pt^{II} loading in combination with steric repulsion for increased colloidal stability. [103, 104] Previous efforts [103] utilized a thiolated dendron with carboxylic terminal groups as the surface-binding ligand. Although the dendron can provide the steric repulsion necessary to support colloidal stability, the Pt^{II}-dendron-AuNP complex was not sufficiently stable following cisplatin complexation, presumably due to neutralization of surface charge.

In Chapter 3, one particular dendron structure was chosen as test bed, designated SH-G1-COOH, which in previous study exhibited the maximum available surface binding sites, but also the poorest colloidal stability. [103] The AuNP surface was modified with polyethyleneglycol (PEG) for the purpose of improving colloidal stability through additional steric hindrance. Additionally, PEGylation has been shown to enhance biocompatibility and delay clearance, [105, 106, 107] though quantifying these effects was beyond the scope of this study. This Chapter investigated the effect of surface PEGylation on colloidal stability, drug loading and release performance using the test bed formulation.

Electrospray differential mobility analyzer hyphenated with inductively coupled plasma mass spectrometry (ES-DMA-ICP-MS) and a condensation particle counter (CPC), [78] was used on a quantitative basis to systematically study: (1) the relationship between loading of Pt^{II} and colloidal stability in biologically relevant test media such

as phosphate buffered saline (PBS) and Dulbecco's modified Eagle's medium (DMEM); (2) the effect of PEGylation (packing density and relative molecular mass) on colloidal stability and Pt^{II} loading capacity; and (3) pH-dependent release performance of Pt^{II} from the AuNP-dendron delivery platform and the consequent influence of PEGylation.

3.2 Materials and Experiments

Citrate stabilized gold colloid (10 nm, nominal particle diameter) was obtained from Ted Pella, Inc. (Redding, CA) and produced by BBI Solutions (Cardiff, UK).* Thiolated polyethylene glycol (SH-PEG, 1, 5 and 10 kDa) was purchased from Nanocs Inc. (New York, NY). Cis-diamminedichloroplatinum (II) (trade name Platinol; formula cis-PtCl₂(NH₃)₂) and silver nitrate (AgNO₃, 99 %) were purchased from Sigma-Aldrich (St. Louis, MO). Sodium hydroxide (NaOH, pellets, 99 %) was obtained from Mallinckrodt Chemicals (Phillipsburg, NJ). Phosphate buffered saline (PBS10X) and Dulbecco's modified Eagle's medium (DMEM) were obtained from HyClone (Logan, Utah). The composition of pH 5 buffer used for release experiment contains 137 mmol/L of NaCl, 2.7 mmol/L KCl, 3.48 mmol/L of HAc and 8.32 mmol/L NaAc to better match the electrolyte content of PBS.

All chemicals were used as received without further purification. Deionized (DI) water (18.2 MΩ·cm) was produced by an Aqua Solutions (Jasper, GA) biological grade water

* The identification of any commercial product or trade name does not imply endorsement or recommendation by the National Institute of Standards and Technology.

purification system. As an activated Pt(II) moiety for complexation, *cis*-[Pt^{II}(NH₃)₂(H₂O)₂](NO₃)₂ was prepared by a slightly modified procedure reported in the literature, as follows: [108] An aqueous solution of AgNO₃ (16.9 mg, 0.1 mmol) in water (2.5 mL) was added drop wise to cisplatin (15 mg, 0.05 mmol) in DI water (2.5 mL) and stirred in the dark for 1 h at 50 °C. A white precipitate (AgCl) was removed by filtration and the filtrate of the activated Pt(II) (with Cl⁻ displaced by the more labile NO₃⁻) was used for complexation with surface modified AuNPs diluted as needed. The dendron was synthesized in our lab using a previously described method. [104] Among the different structural forms of dendrons, we used SH-G1-COOH because it yielded the highest loading capacity for cisplatin (Pt^{II}). G1 expresses a branched structure analogous to a 1st generation dendrimer terminated with three COOH groups. SH-G1-COOH has a wedge-shaped branching structure as shown in Figure 3.1. The COOH groups provide complexing sites for Pt^{II}, and the thiol group provides covalent bonding to the AuNP surface. To activate (deprotonate) the carboxylate group, the dendron (5 mmol/L) was dissolved in NaOH (15 mmol/L) to obtain the maximum carboxylate population.

3.2.1 Conjugation of AuNP-(dendron) and AuNP-(dendron)-(SH-PEG)

As illustrated in Figure 3.1 the initial AuNP-(dendron) conjugate and the modified conjugate AuNP-(dendron)-(SH-PEG) were used for comparison. Carboxylate terminated dendron (5 mmol/L) was added dropwise to a AuNP suspension (57.6 µg/mL) in a 1-to-10 volume ratio, and stirred for 5 h at room temperature. The

resulting product (designated as AuNP-(dendron)) was purified by centrifugal filtration using a 100 kDa regenerated cellulose membrane.

A series of AuNP-(dendron)-(SH-PEG) samples were prepared by drop-wise addition of 1 part by volume of an aqueous solution containing (1, 5 or 10) kDa SH-PEG at concentrations of (0.1, 0.5, 1.0, and 5.0) mmol/L, to 11 parts by volume of purified AuNP-dendron conjugate suspension with stirring at room temperature for 5 h. The resulting products were designated as AuNP-(dendron)-(SH-PEG)-(50-1), AuNP-(dendron)-(SH-PEG)-(10-1), AuNP-(dendron)-(SH-PEG)-(5-1), and AuNP-(dendron)-(SH-PEG)-(1-1), where X-1 represents the molar ratio (X:1) of dendron to SH-PEG for the reaction. The designation “xK” appended to the product name is shorthand for “x kDa” relative molecular mass of SH-PEG. The full naming scheme is, for example, AuNP-(dendron)-(SH-PEG5K)-(50-1), for the 5 kDa PEGylated dendron ligated AuNPs with a 50:1 molar ratio of dendron to SH-PEG in solution. For convenience, 5K is shorthand for SH-PEG5K in all the figures, and similarly for 1K and 10K.

After reaction, the mixture was again purified by centrifugal filtration. As a control, citrate-stabilized AuNPs were conjugated with SH-PEG, and labeled as AuNP-(SH-PEG)-(5mM) where 5 mmol/L SH-PEG solution was added drop-wise to AuNP suspensions in a 1 to 11 volume ratio (final SH-PEG concentration in solution was 0.42 mmol/L)

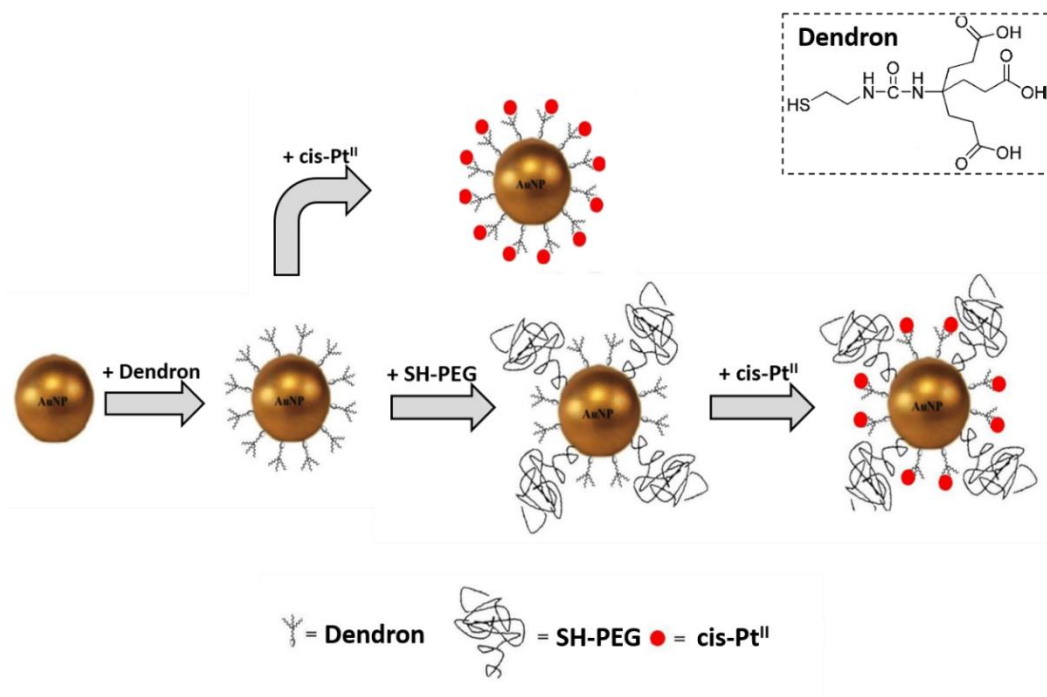


Figure 3.1. Cartoon depiction of conjugation and complexation steps in processing of AuNP-(dendron), AuNP-(dendron)-(SH-PEG) and Pt^{II} complexed products.

3.2.2 Complexation with cisplatin

A solution of *cis*-[Pt^{II}(NH₃)₂(H₂O)₂](NO₃)₂ was added drop-wise to either AuNP-dendron suspension or PEGylated AuNP-(dendron) suspension (in a volumetric ratio of 1 to 10), and was then mildly shaken using a vortex mixer (from VWR) at 400 rpm in the dark for 2 h at room temperature. The final concentration of Pt^{II} for the reaction ranges from 0.6 μmol/L to 34 μmol/L (of Pt to Au mass ratio 1:448 to 1:8). Before mixing with Pt^{II}, the AuNP containing suspension was modified to obtain a pH of roughly 7 by addition of NaOH. After complexation, any free (uncomplexed) Pt^{II} was removed by spinning down the NPs in a microfuge and replacing the supernatant with DI water.

3.2.3 Optimization of cleaning steps and cisplatin complexation time

The cleaning step was examined and optimized to ensure that free Pt^{II} would not influence the Pt^{II} loading measurement. In order to eliminate the effect of free Pt^{II} (note: free Pt^{II} dries on the AuNP surface during the electrospray process) on the Pt^{II} loading measured by ES-DMA-ICP-MS, the cleaning procedure was investigated. Centrifugation was applied to remove any free Pt^{II}. Briefly, 1 mL of solution was centrifuged to separate AuNP from solution and the supernatant was carefully removed ($\approx 970 \mu\text{L}$, which represents 1st round of centrifugal cleaning). Subsequently, 450 μL of deionized (DI) water was added back to the solution, and the suspension was centrifuged again, and $\approx 470 \mu\text{L}$ of supernatant was removed (2nd round). This last step was then repeated several more times. For each cleaned sample, 30 μL water and 20 μL ammonium acetate (20 mmol/L) was added immediately before measurement. Figure 3.2(a) demonstrates that no significant difference in Pt^{II} loading was observed before centrifuge cleaning and after several rounds of cleaning. In our experiment, 2 rounds of cleaning was adopted as a standard procedure. Different reaction times for Pt^{II} complexation ranging from 0 h to 6 h were examined. From Figure 3.2(b) the reaction rate for Pt^{II} complexation is fast and no significant difference in Pt^{II} loading was observed for reaction times from 1 h to 6 h. Therefore, 2 h was deemed sufficient for Pt^{II} complexation and was adopted for this study. For 0 h of Pt^{II} complexation, the Pt^{II} was added to AuNP suspension and immediately cleaned of free Pt^{II} before measurement by ES-DMA-ICP-MS. The loading of 0 h reaction was considered to be due to the contact of free Pt^{II} and AuNP suspension during the centrifuge cleaning step.

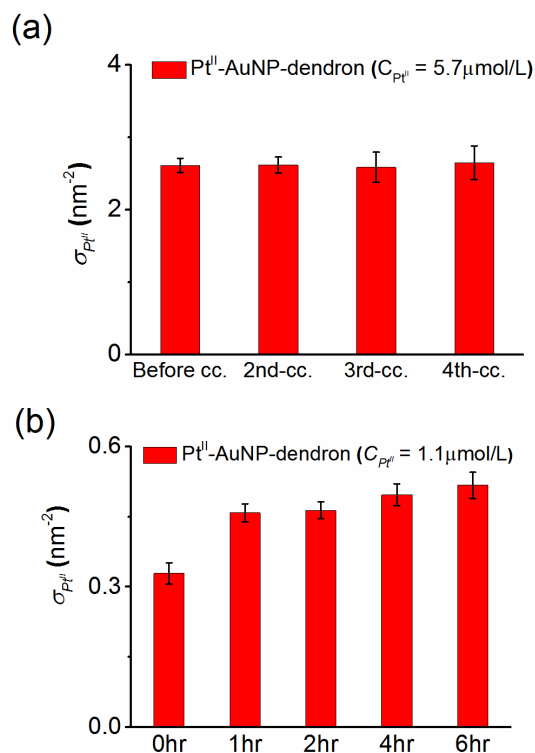


Figure 3.2. (a) The effect of centrifuge cleaning step on Pt^{II} loading ($\sigma_{Pt^{II}}$) after each round of cleaning, and (b) the effect of reaction time on Pt^{II} loading. Error bars for $\sigma_{Pt^{II}}$ represent the standard deviation derived from the value of Pt/Au across a range of particle sizes in the mass based PSD.

3.2.4 Cisplatin release

Pt^{II} release studies were carried out by ICP-MS measurement of free released Pt^{II} at time points of 0, 2 and 10 days. Centrifugal filtration (3 kDa regenerated cellulose membrane) was used to separate free Pt^{II} from that loaded on AuNPs. Before initiation of release experiment, uncomplexed Pt^{II} was removed by two rounds of cleaning (via centrifugation) in a microfuge and replacing the supernatant with DI water. Total

loading of Pt^{II} on AuNPs was obtained by ICP-MS measurement of digested cleaned Pt^{II}-AuNP conjugates. The percentage of Pt^{II} release at a specific time is defined as the ratio of free released Pt^{II} to that of the total Pt^{II} on AuNPs. Two buffers (PBS and pH 5 buffer) were used for release studies.

3.2.5 ATR-FTIR

Attenuated total reflectance Fourier transform infrared (ATR-FTIR) spectra were collected on a Thermo Scientific Nicolet iS50 (Thermo Fisher Scientific, Waltham, MA) equipped with Pike horizontal ATR (HATR) ZnSe 45° crystal (Pike Technologies, Madison, WI). Three samples, AuNP-(dendron), AuNP-(dendron)-(PEG5K)-(5-1) and AuNP-PEG5K, were purified by centrifugal filtration, dropcasted onto the crystal, and dried prior to examination. Spectra presented were collected over 250 scans at 2.0 cm⁻¹ resolution.

3.2.6 ES-DMA-ICP-MS

ES-DMA was operated with a sheath flow of 10 L/min (argon) and an aerosol flow of 1 L/min (air). To make a direct measurement of particle counts as a function of size we direct the output of the DMA to the CPC (inlet flow of 1.5 L /min) to obtain a number-weighted particle size distribution. The ICP-MS was operated in time resolved acquisition mode (TRA), with a dwell time of 0.5 s, to monitor signal intensity ($I_{Pt(CPS)}$ and $I_{Au(CPS)}$) at a fixed DMA voltage. The DMA was then stepped to another voltage representing a specific mobility size so that an elemental characterization as a function of particle size could be obtained.

3.2.7 Quantification of cisplatin loading

The Pt^{II} loading on a AuNP is defined as the number of Pt^{II} molecules per unit surface area of a single particle. The ratio can be measured quantitatively by ICP-MS as: [103]

$$\sigma_{\text{Pt}^{\text{II}}} = \alpha_{\text{Au-Pt}} \times \frac{I_{\text{Pt}}(\text{cps})}{\frac{I_{\text{Au}}(\text{cps}) \times M_{\text{m,Au}}}{N_{\text{av}} \times \rho_{\text{Au}}} \times \frac{S_{\text{AuNP}}}{V_{\text{AuNP}}}} \quad (3.1)$$

Where $I_{\text{Pt}}(\text{CPS})$ and $I_{\text{Au}}(\text{CPS})$ represents the signal intensity of ¹⁹⁵Pt and ¹⁹⁷Au detected by ICP-MS in counts per second (CPS); S_{AuNP} and V_{AuNP} are the surface area and volume of a single AuNP (in this case, these parameters are obtained from the DMA diameter d_p and assuming spherical geometry); $M_{\text{m,Au}}$ and ρ_{Au} are the molar mass and density of Au, and N_{av} is Avogadro's number; $\alpha_{\text{Au-Pt}}$ is a calibration factor taking into account the relative sensitivity of ICP-MS for ¹⁹⁷Au and ¹⁹⁵Pt. As shown in Figure 3.3, the ratio from the slope of the two calibration curves represent the relative sensitivity. $\alpha_{\text{Au-Pt}} = 12367/10437=1.18$.

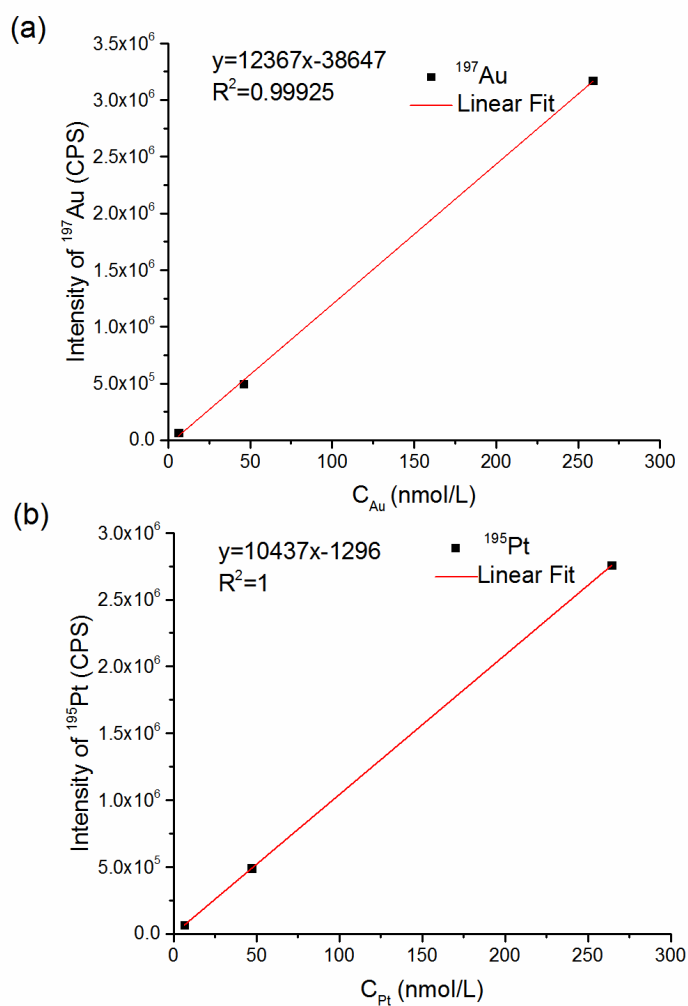


Figure 3.3. Sensitivity calibration curve for (a) ^{197}Au and (b) ^{195}Pt by ICP-MS

3.3 Discussion

3.3.1 Molecular conjugation of dendron and SH-PEG on AuNPs

SH-PEG with three relative molecular masses (1 kDa, 5 kDa and 10 kDa) were examined. Figure 3.4(a) shows the corresponding particle size distributions (PSDs) measured for AuNPs, their dendron conjugates and the product after reaction with SH-

PEG5K. The PSDs for the 1 kDa and 10 kDa SH-PEG conjugation to AuNP-dendron are shown in Figure 3.5(a)-(b). The corresponding hydrodynamic size measured by DLS is provided in Table 3.1. For clarity, the number densities shown in Figure 3.4(a) are normalized to unity. As shown in Figure 3.4(a), the citrate-stabilized AuNPs (after centrifugal cleaning) have a size distribution centered at 11.4 nm prior to molecular conjugation. Upon conjugation with the dendron, the peak size increases to 12.4 nm; the difference representing the dried dendron corona. After subsequent reaction with increasing concentrations of SH-PEG5K, from (0.1 to 5) mmol/L, the peak size continually increases from 14.8 nm to 15.6 nm; this increase is indicative of SH-PEG5K uptake onto the AuNP surface. The width of the size distribution, as determined from the peak-width at half-maximum, does not significantly change with conjugation (from 1.7 nm for citrate stabilized AuNPs to 1.8 nm for AuNP-(dendron)-(SH-PEG5K)), implying that conjugation does not alter the effective PSD shape or width (i.e., it does not induce significant agglomeration).

The peak size in Figure 3.4(a) reaches a plateau value of 15.6 nm with increasing concentration of SH-PEG, yet is clearly smaller than the peak size (20.8 nm) obtained for AuNP-(SH-PEG5K) formed in the absence of the dendron. This clearly shows that the dendron partially inhibits adsorption of SH-PEG5K. Similar results were obtained for the 1 kDa and 10 kDa PEG. Note that the small DMA peaks situated below 10 nm are attributed to the nonvolatile remnants generated by the electrospray, [¹⁰⁹] and in our case these remnants are negligibly small due to the previously described cleaning steps.

ATR-FTIR spectra, shown in Figure 3.4(b), were recorded for AuNP-(dendron) and AuNP-(SH-PEG5K). The ATR-FTIR spectrum of the target species AuNP-(dendron)-

(SH-PEG5K) was then compared with that of both AuNP-(dendron) and AuNP-(SH-PEG5K) in order to monitor the presence and relative quantity of each ligand. Each spectrum was normalized to the highest peak intensity for clarity. As shown in Figure 3.4(b), the AuNP-(dendron) exhibits a distinct peak at 1570 cm^{-1} designated as the anti-symmetric stretching for COO^- from the carboxyl group of the dendron, and similarly the absorbance at 1410 cm^{-1} corresponds to the symmetric stretch for COO^- . The small peak at 1710 cm^{-1} is assigned to $\text{C}=\text{O}$ stretching (again associated with the dendron). [110] On the other hand, for AuNP-(SH-PEG5K), the peak at 1110 cm^{-1} is characteristic of C-O stretching in the SH-PEG5K structure. [111] Comparing the measured absorbance for AuNP-(dendron)-(SH-PEG5K), where SH-PEG5K was added post-dendron conjugation, the characteristic peaks for both dendron and SH-PEG5K appear, confirming the presence of both ligands. The physical measurement of PSDs using DMA combined with the ATR-FTIR spectroscopic results confirm that SH-PEG5K binds to the AuNP-(dendron) conjugate, and suggests that this reaction occurs without substantial displacement of the bound dendron. It should be emphasized that SH-PEG is a potential competitive binding ligand capable of displacing other ligands, but in this case the dendron-Au bond appears sufficiently stable to resist displacement and block some potential adsorption sites for SH-PEG.

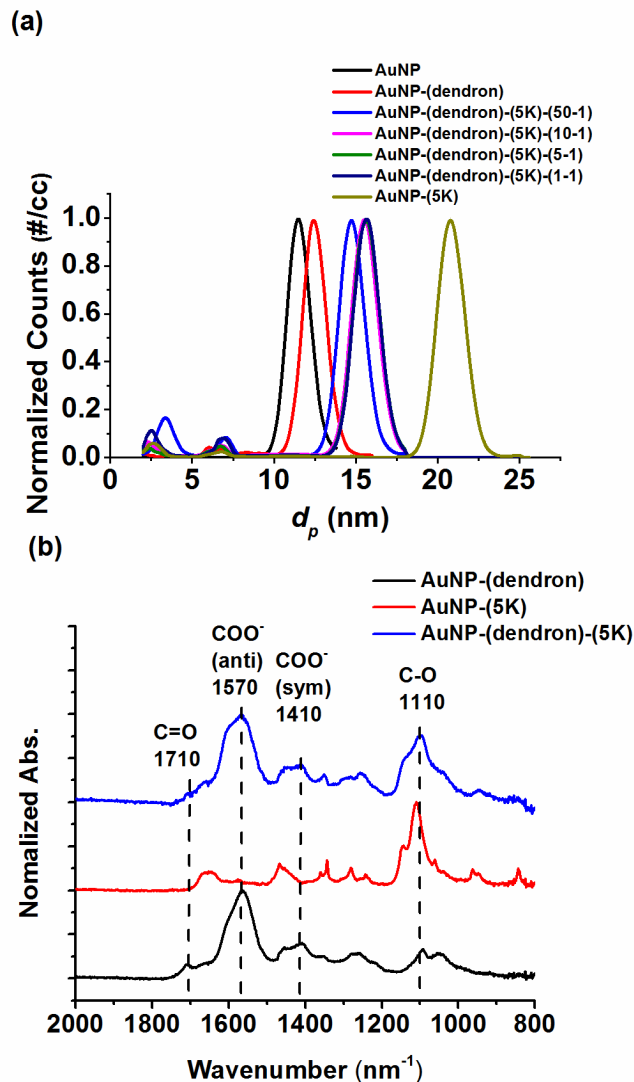


Figure 3.4. Surface conjugation of SH-PEG and dendron on AuNPs. (a) Normalized number-weighted PSDs measured by ES-DMA-CPC. (b) Molecular binding of dendron and SH-PEG5K on AuNP characterized by ATR-FTIR. A 5-1 ratio of dendron to SH-PEG5K was used as a representative example for the ATR-FTIR study. Baseline subtraction was performed for each spectrum (adsorption at wavenumber 1800 nm^{-1} was chosen as zero) and followed by normalization to the highest peak intensity. Dashed lines mark the characteristic vibrational modes from dendron and SH-PEG5K.

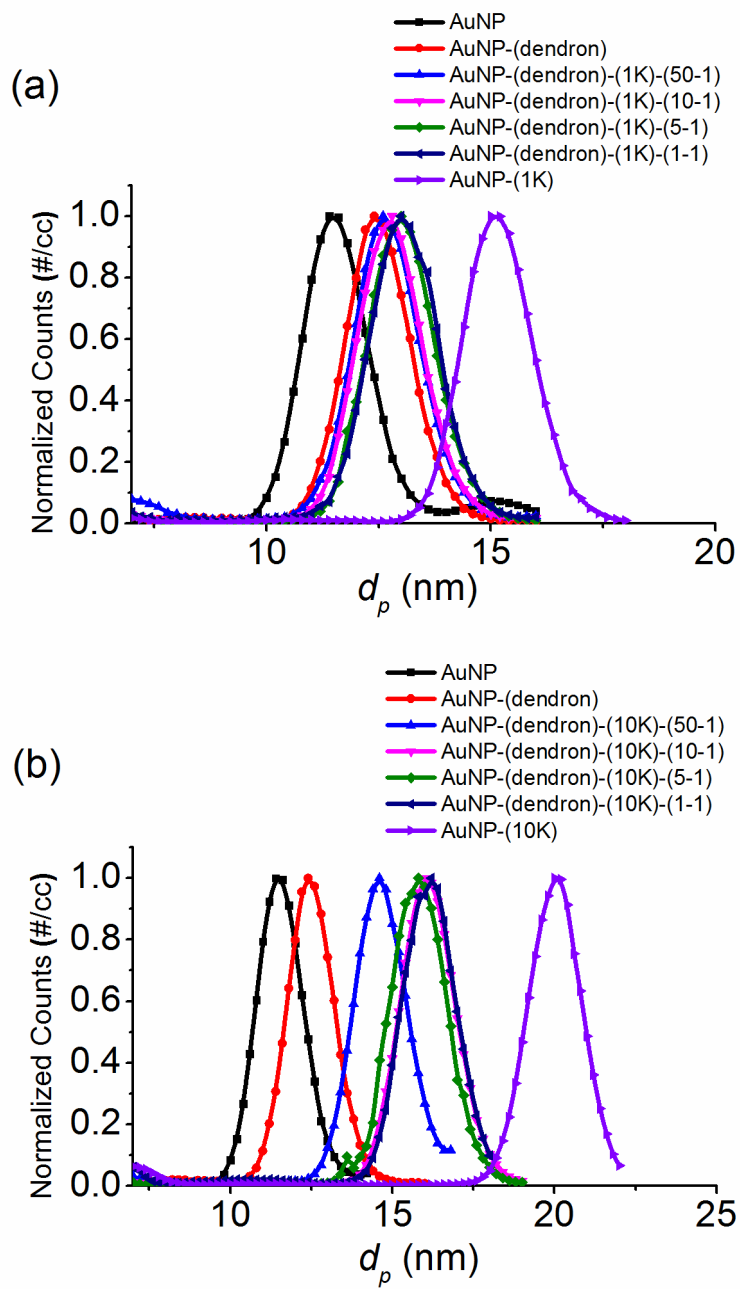


Figure 3.5. Mobility size distributions for (a) AuNP-(dendron)-(SH-PEG1K) and (b) AuNP-(dendron)-(SH-PEG10K).

Table 3.1. Mean hydrodynamic size by DLS for AuNP-dendron-SH-PEG conjugates in water medium with one standard deviation reported from 5 replicate measurements.

Sample	Z-average (<i>d</i>,nm)
AuNP	14.4±0.7
AuNP-(dendron)	13.3±0.5
AuNP-(dendron)-(1K)-(50-1)	17.1±0.1
AuNP-(dendron)-(1K)-(10-1)	16.0±0.3
AuNP-(dendron)-(1K)-(5-1)	16.2±0.3
AuNP-(dendron)-(1K)-(1-1)	17.5±0.5
AuNP-(1K)-(5mM)	19.5±0.6
AuNP-(dendron)-(5K)-(50-1)	28.5±0.3
AuNP-(dendron)-(5K)-(10-1)	29.8±0.7
AuNP-(dendron)-(5K)-(5-1)	29.1±0.5
AuNP-(dendron)-(5K)-(1-1)	30.6±0.5
AuNP-(5K)-(5mM)	35.9±0.7
AuNP-(dendron)-(10K)-(50-1)	35.0±0.2
AuNP-(dendron)-(10K)-(10-1)	36.8±0.2
AuNP-(dendron)-(10K)-(5-1)	36.6±0.2
AuNP-(dendron)-(10K)-(1-1)	45.5±0.5
AuNP-(10K)-(5mM)	47.1±0.3

To better understand the absorption, and to quantify dendron binding and possible steric hindrance due to SH-PEG, we quantify the extent of SH-PEG adsorption on the dendron conjugated AuNP using a refined two-layer geometric model. Prior work has demonstrated the capacity to quantify ligand surface packing density based on careful PSD measurements using ES-DMA. [112] The general concept of this analysis is that by assuming a random coil configuration for the linear SH-PEG molecule, the surface coverage of SH-PEG is obtained from the increase in cross-sectional area obtained via DMA. Here, a refined core-shell model used previously was used to account for two ligand layers, as the contributions to particle size from either ligand could not be neglected (Figure 3.6(a)).

In the two-layer model, the net contribution of SH-PEG to the increase of cross-sectional area was obtained by subtracting the cross-section increase due to the dendron from the total increase. The cross-sectional area of the SH-PEG corona is a function of particle diameter, and therefore the packing density (σ in unit of molecules/nm²) of SH-PEG can be correlated with changes in particle diameter. [113] :

$$\sigma_{SH-PEG} = \frac{[(dp_{Au-dendron} + \Delta dp_{Au-dendron})^2 - dp_{Au-dendron}^2]^2}{[2\pi dp_{bare Au} \langle x^2 \rangle]^2} \quad (3.2)$$

where $\langle x^2 \rangle^{0.5}$ is the random walk radius, the calculated value of which is 3.7 nm [113] for SH-PEG5K under a dried aerosol condition. The random walk radius for 1K and 10K could be calculated similarly using equations from previous work. [113] The surface packing density of SH-PEG was examined as a function of molar mass and SH-PEG concentration.

Figure 3.6(b) shows the adsorption isotherm derived for the surface packing density of SH-PEG onto AuNP-dendron conjugates versus PEG relative molecular mass. With the increase of SH-PEG concentration, the packing density of SH-PEG increases and then plateaus. The plateau surface density, when there is dendron pre-attached to the surface, is 0.003 molecules/nm², 0.008 molecules/nm² and 0.003 molecules/nm², for SH-PEG1K, SH-PEG5K and SH-PEG10K, respectively. The saturated packing density of SH-PEG was compared with the surface coverage of the dendron molecule. Using the same conjugation method, Cho *et al.* [104] reported a packing density for dendron (i.e., SH-G1-COOH) by x-ray photoelectron spectroscopy (XPS) of 0.76 relative to mercaptoundecanoic acid (MUA). Ivanov *et al.* [114] reported that the absolute packing density of MUA on a roughly 12 nm diameter AuNP surface was 4.97 molecules/nm² determined by XPS. Therefore, the estimated packing density for the dendron was ≈ 3.8 molecules/nm². In comparison, the saturated packing density of SH-PEG accounted for ≤ 0.2 % that of dendrons, (0.08 %, 0.2 % and 0.08 % for SH-PEG1K, SH-PEG5K and SH-PEG10K, respectively, in ratio to dendron). The surface is therefore covered primarily by dendrons, with a relatively small presence of SH-PEG on a number basis. In terms of molecular mass, the saturated packing density of PEG-1K, 5K, and 10K is 0.2 %, 3 % and 2.3 %, respectively, relative to that of dendron. The saturated packing density is independent of PEG relative molecular mass in this case. As shown below, a very different result is obtained when SH-PEG is conjugated directly to the citrate-stabilized AuNPs without the dendron corona present.

For comparison, 0.42 mmol/L of SH-PEG was added to citrate-stabilized AuNPs. At this concentration, the surface packing of SH-PEG reached saturation levels on the

AuNP-dendron surface (≤ 0.008 molecules/nm²), as indicated by the adsorption isotherms in Figure 3.6(b). By contrast, the resulting SH-PEG packing density on citrate-stabilized AuNPs, as shown in Figure 3.6(c), is ≈ 0.12 molecules/nm², 0.08 molecules/nm² and 0.02 molecules/nm², for SH-PEG1K, SH-PEG5K and SH-PEG10K, respectively. These packing densities are more than an order of magnitude higher in comparison to those for AuNP-(dendron)-(SH-PEG1K, 5K, and 10K) conjugates. The sharp decrease in packing density with respect to an increase of SH-PEG molecular mass on citrate-stabilized AuNPs is attributed to intermolecular steric hindrance between the SH-PEG molecules when more closely packed on the surface. Note that the higher relative molecular mass of SH-PEG10K yields a higher occupied area per molecule on the AuNP surface, and therefore a lower molecular packing density.

It was concluded for this part of the study that the principal limiting factor for uptake of SH-PEG by the AuNP-dendron conjugate surface is the availability of bonding sites (due to pre-attached dendron) rather than steric hindrance produced by the relatively larger SH-PEG molecules.

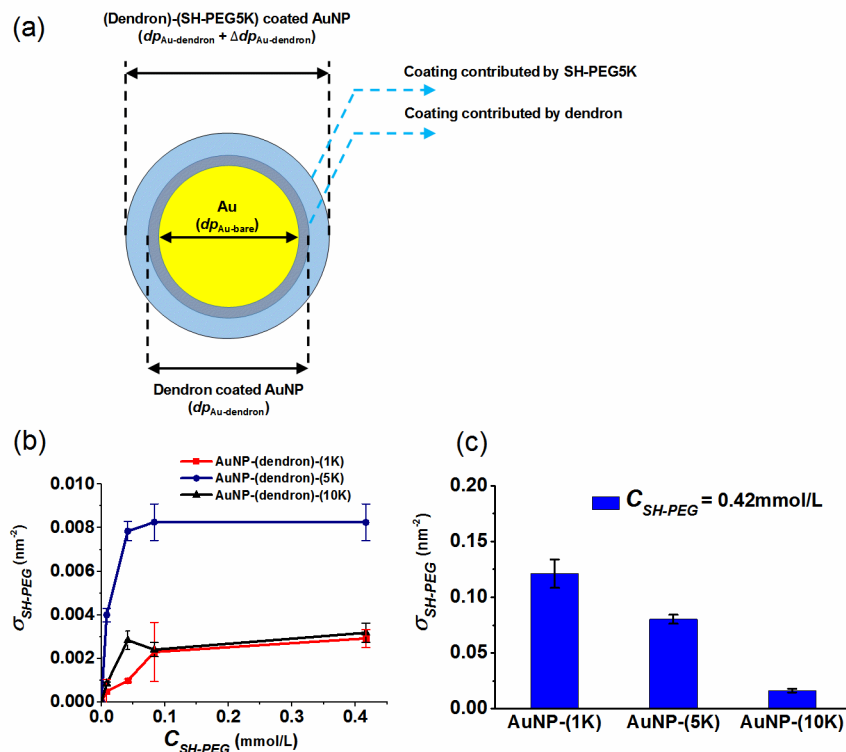


Figure 3.6. (a) Schematic illustration of the two-layer core-shell model used to quantify SH-PEG packing density used for Eq. (3.2). (b) Adsorption isotherm for SH-PEG on AuNP-dendron conjugates. (c) Citrate AuNP conjugated with SH-PEG 1K, 5K and 10K, at SH-PEG concentration of 0.42 mmol/L during reaction. Packing density is given in molecules/nm². Error bars represent one standard deviation for at least four replicate measurements. In order to include ligand stability over the time scale of experiments, four replicate measurements were performed within a time scale of ≈ 10 days.

3.3.2 Binding of cisplatin to surface engineered AuNPs

In the next phase of this investigation, we evaluate the effects of Pt^{II} complexation on conjugated AuNPs and, conversely, the effects of surface engineering on Pt^{II} complexation. Figure 3.7(a) shows the element-mass weighted particle size distribution for Pt^{II} complexed AuNPs obtained by ES-DMA-ICP-MS. Before analysis, free Pt^{II} was removed from the Pt^{II}-AuNP-(dendron)-(with or without SH-PEG) suspension by centrifugation. In this case we can simultaneously track signal intensity for ¹⁹⁷Au and ¹⁹⁵Pt ($I_{Pt(CPS)}$ and $I_{Au(CPS)}$) as a function of the mobility diameter, d_p (determined solely by the voltage applied to the DMA). Note that the signal intensity for ¹⁹⁷Au is significantly higher than that for ¹⁹⁵Pt, however the two curves are clearly superimposed and indicate more than sufficient signal-to-noise for characterizing size classified particles. These results also confirm that Pt is associated with the AuNPs and not free in solution. From this result, the average Pt^{II} loading on AuNP-(dendron) conjugates can be determined using Eq. (3.1).

Exploiting the capacity to quantify Pt^{II} loading on AuNPs, we examine the effect of Pt^{II} solution concentration. As shown in Figure 3.7(b), the loading of Pt^{II} ($\sigma_{Pt^{II}}$) increased gradually with respect to increased Pt^{II} concentration during complex formation, and plateaued at ≈ 8 Pt^{II} molecules/nm², indicating that Pt^{II} has reached a saturation level under the conditions studied. Since surface coverage of the dendron is ≈ 3.8 molecules/nm² and each dendron molecule contains three carboxylate groups, this yields ≈ 3 Pt^{II}/nm² of available complexing sites. The saturated Pt^{II} loading of ≈ 3 Pt^{II}/nm² suggests that some fraction of Pt^{II} ions may form bidentate complexes with adjacent carboxyl groups. [¹⁰²]

Next we address the quantitative effect of SH-PEG surface packing (σ_{SH-PEG} and relative molecular mass of SH-PEG) on Pt^{II} loading. Figure 3.7(c) shows how the Pt^{II} loading changes with respect to the SH-PEG5K packing density (σ_{SH-PEG}), while fixing the available Pt^{II} complexation sites. In this case, Pt^{II} loading is relatively insensitive to the packing density SH-PEG5K – ranging from (0 to 0.008) molecules/nm² – on AuNP-(dendron)-(SH-PEG5K). Considering that SH-PEG5K binding density on the AuNP-(dendron) surface amounts to less than 0.2 % by number of the total dendron present, the available binding sites (COO⁻) for AuNP-dendron and AuNP-(dendron)-(SH-PEG5K) should be roughly equivalent. Similarly, there is a very mild effect of SH-PEG molecular mass (1K, 5K and 10K in this case) on Pt^{II} loading (see Figure 3.7(d)). For samples susceptible to agglomerate formation during the centrifugal cleaning process, $\sigma_{Pt^{II}}$ was reported from agglomerates since $\sigma_{Pt^{II}}$ was previously demonstrated to be independent of agglomeration states. [103]

In combination with the quantification of dendron and SH-PEG obtained in Figure 3.6 and Figure 3.7, it was concluded that attachment of SH-PEG does not significantly degrade the loading capacity for the active drug. What remains to be determined is the effect of SH-PEG on colloidal stability of the Pt^{II} complexed conjugate.

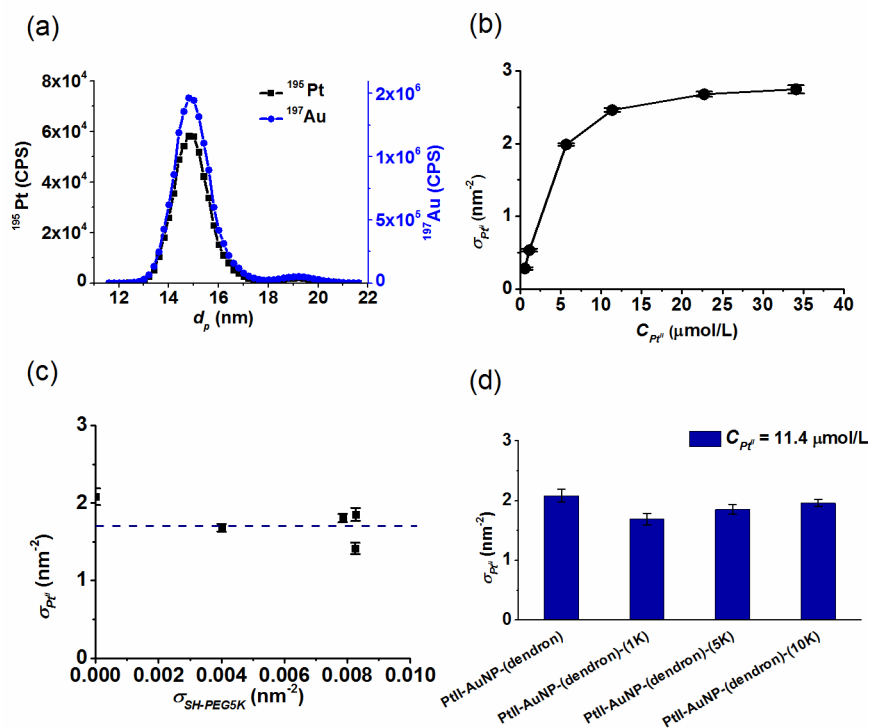


Figure 3.7. Quantification of Pt^{II} loading by ES-DMA-ICP-MS. (a) Representative elemental mass-based particle size distributions for AuNP-(dendron)-(SH-PEG5K) at $C_{Pt^{II}} = 11.4 \mu\text{mol/L}$. Blue: ^{197}Au trace; black: ^{195}Pt trace, (b) Loading of Pt^{II} on AuNP-dendron vs the concentration of Pt^{II}, (c) Loading of Pt^{II} vs the packing density of SH-PEG5K on AuNP at $C_{Pt^{II}} = 11.4 \mu\text{mol/L}$ (dashed line is only a guide), (d) Pt^{II} loading vs SH-PEG relative molecular mass (1kDa, 5kDa and 10kDa), at around saturation packing density (i.e. 5 to 1 dendron to SH-PEG) at $C_{Pt^{II}} = 11.4 \mu\text{mol/L}$. Error bars for $\sigma_{Pt^{II}}$ represent one standard deviation about the mean value derived from Pt/Au across a range of particle sizes in the mass-based PSD for one measurement in the same subsample. Uncertainties for same subsample (but with measurement replicates) and between different subsamples were determined by relative standard deviation and were $< 9\%$ demonstrating good precision (Figure 3.8).

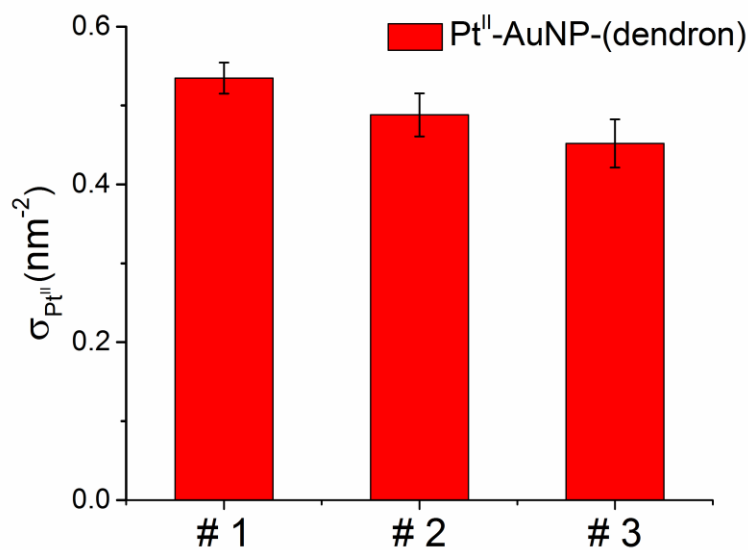


Figure 3.8. Uncertainty examination for $\sigma_{\text{Pt}^{\text{II}}}$. $\text{Pt}^{\text{II}}\text{-AuNP-(dendron)}$ at $C_{\text{pt}^{\text{II}}} = 1.1 \mu\text{mol/L}$ was used as an example. #1 and #2 represent $\sigma_{\text{Pt}^{\text{II}}}$ obtained from different replicate measurements for the same sub-sample and represents instrument or measurement precision. #3 is obtained from replicate samples beginning with sample preparation. Error bars represent uncertainty derived from the average value of Pt/Au across a range of particle sizes in the mass based PSD for one experiment and for the same sub-sample. The relative standard deviation from the average of #1 to #3 is less than 9% demonstrating good repeatability.

3.3.3 Colloidal stability (by ES-DMA-ICP-MS)

Previous work has shown that complexation of Pt^{II} itself leads to colloidal destabilization of the conjugate due to electrostatic interactions between the anionic carboxylates and the positively charged Pt^{II} . [103] The principal motivation for

PEGylation is to counteract that effect. Here we investigate the efficacy of PEGylation to preserve stability in biologically relevant media. ES-DMA has the capacity to quantify nanoparticle agglomeration kinetics. [65] The high sensitivity of ICP-MS as a detector enables sensitivity for low-order AuNP agglomerates at very low concentrations and should also be useful in tracking agglomeration in complex media (in this case, DMEM and PBS solution), as the element-specific detection enables direct identification of the agglomeration component (whereas CPC is indiscriminant with respect to detection).

The raw spectrum obtained by ES-DMA-ICP-MS is a mobility size-resolved intensity (^{197}Au) distribution (as shown in Figure 3.9).

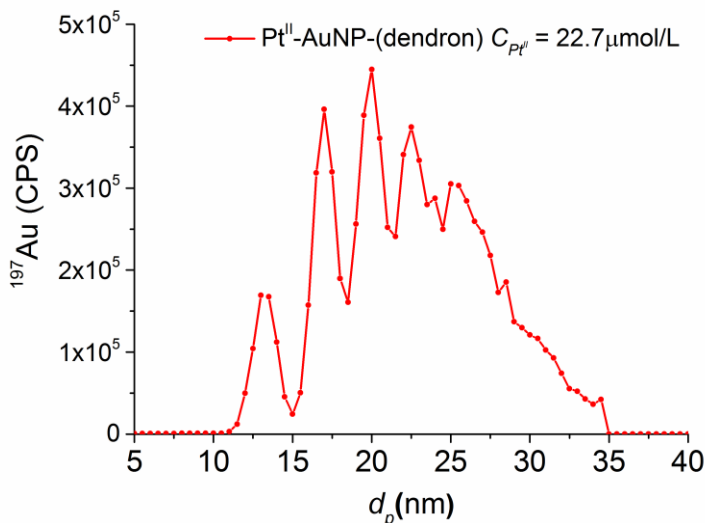


Figure 3.9. Mobility size resolved-intensity (^{197}Au) distribution. Each resolved peak represents oligomers of AuNP conjugates (i.e. $\text{Pt}^{\text{II}}\text{-AuNP-(dendron)}$ in this case) : monomer, dimer, trimer etc.

Each distinguishable peak is assigned to an oligomer state based on mobility size: [115] monomer, dimer, trimer, tetramer, etc. The ICP-MS intensity $I_{Au,n}$ for oligomer n is related to the oligomer mass through an appropriate calibration factor. For a single oligomer, the mass of n -mer (an oligomer consisting of n primary particles) is n times the mass of a primary AuNP of. Therefore, the number of oligomer particles is related to the ^{197}Au intensity as follows:

$$N_n = \psi \times \frac{I_{Au,n}}{n} \quad (3.3)$$

where Ψ represents a function that includes the sensitivity factor for ^{197}Au , α_{Au} , and the density and volume of a primary size AuNP, ρ_{Au} and V_{AuNP} (i.e., $\Psi = f(\alpha_{Au}, \rho_{Au}, V_{AuNP})$). N_n represents the number of nanoparticle agglomerates containing n primary particles. It should be noted that for a given set of experimental conditions, Ψ is a constant and not a function of the oligomer state.

In order to investigate the colloidal stability of nanoparticles, we utilize the degree of agglomeration (DA). The degree of agglomeration is defined here as follows: [65]

$$DA = \frac{\sum n n N_n}{\sum n N_n} \quad (3.4)$$

Combining with equation (3.3), DA is expressed as:

$$DA = \frac{\sum n I_{Au,n}}{\sum n \frac{I_{Au,n}}{n}} \quad (3.5)$$

Therefore, DA represents the average number of particles per agglomerate and will increase from unity with respect to time for an unstable system. Considering the resolving power of ES-DMA-ICP-MS to distinguish oligomers, the analysis is limited to tetramers, and therefore the maximum DA in this study is four.

Figure 3.10(a) quantifies the effect of added Pt^{II} on DA versus reaction time, t , for various Pt^{II} concentrations. At low Pt^{II} concentrations ($C_{\text{Pt}^{\text{II}}} = 1.1 \mu\text{mol/L}$ and $5.7 \mu\text{mol/L}$) and for reaction times as long as 12.5 days, DA remains close to unity, demonstrating that the monomer specie is dominant in solution and the conjugate is colloiddally stable before mixing with Pt^{II} ; therefore, $\text{DA}=1$ is assumed for $t=0$ (0 h stands for the point immediately after adding Pt^{II}). With an increase in Pt^{II} concentration to $11.4 \mu\text{mol/L}$, a gradual increase in agglomeration with respect to time was observed. At Pt^{II} concentrations as high as $34.1 \mu\text{mol/L}$, DA approaches ≈ 3.0 in less than 4 h, indicating a substantial increase in agglomeration kinetics. We attribute the reduced stability at higher cisplatin loadings to an increase in neutralization of carboxylate groups resulting in weaker charge stabilization.

Figure 3.10(b) characterizes the effect of PEGylation on colloidal stability at a fixed Pt^{II} concentration ($C_{\text{Pt}^{\text{II}}} = 11.4 \mu\text{mol/L}$). We examined PEG with three relative molecular masses (1 kDa, 5 kDa and 10 kDa). Since no significant influence of SH-PEG packing density on Pt^{II} loading was observed, we chose to investigate the highest SH-PEG packing density for each relative molecular mass. In comparison to the Pt^{II} -Au-dendron complexes, where DA increased gradually to roughly 3 within one day, the PEGylated Au-(dendron)-(SH-PEG1K), Au-(dendron)-(SH-PEG5K) and Au-(dendron)-(SH-PEG10K) remained close to unity for up to 24 d. This result unequivocally confirms that PEGylation imparts stabilization to otherwise unstable highly loaded Pt^{II} complexed AuNPs. The effect was independent of SH-PEG relative molecular mass. Colloidal stability in biologically relevant matrices (PBS and DMEM) was also examined. The AuNP-dendron complexed with Pt^{II} precipitated immediately

(visually evident) when in contact with either PBS or DMEM buffer. However PEGylated samples exhibited visibly improved stability with a DA less than ≈ 1.5 over a period of two days. Since electrostatic induced stability is generally eliminated at biological saline levels, the enhanced dispersion stability can be attributed to steric interactions provided by the PEG chains attached to the surface. Although SH-PEG uses less than 2 % of dendron surface coverage, it is sufficient to provide obvious enhancement of dispersion stability for the Pt^{II}-AuNP platform, either in water or more complex biological media, with an insignificant trade-off in drug loading.

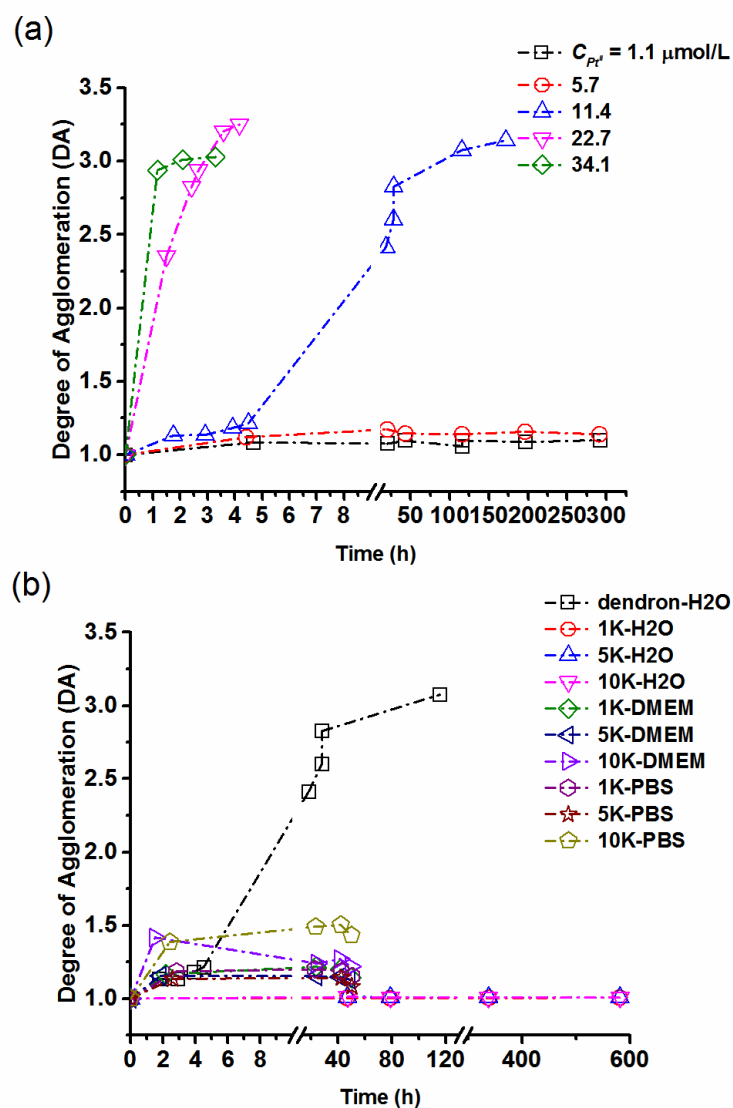


Figure 3.10. Quantifying colloidal stability using ES-DMA-ICP-MS. Initial mixing of cisplatin with AuNP conjugates occurs at 0 h, with the x-axis showing time after mixing or reaction time. Before mixing with Pt^{II} , samples are stable and therefore $DA=1$ was assumed at $t=0$. (a) Effect of Pt^{II} on colloidal stability. (b) Effect of PEGylation on stability in different media. The parameter DA was calculated from mass distribution measurements using DMA-ICP-MS. A relative standard deviation of 7 % is estimated based on the mean standard deviation performed at each size step. [103]

3.3.4 Cisplatin Release Performance

Nanoparticles were incubated at pH 5 mimicking the acidic pH of the endolysosomal compartment of a tumor. PBS was selected as a control to mimic pH conditions during blood circulation (pH 7.4), where Pt^{II} release should be minimal. In PBS (Figure 3.11(a)), the Pt^{II}-AuNP platforms examined in this study showed essentially no release of Pt^{II}, while at pH 5 (Figure 3.11(b)), a clear preferential release relative to PBS was observed.

As an example, at day 10, AuNP-(dendron)-(SH-PEG5K)-high Pt^{II} exhibited a 10-fold increase in Pt^{II} release at pH 5 compared with PBS. Under acidic conditions, a release burst occurred within 2 d, followed by a slow release between (2 and 10) d. Notably, PEG relative molecular mass (1 kDa and 5 kDa) showed no significant influence on Pt^{II} release performance. Overall release performance is poor, but by increasing Pt^{II} loading (high Pt^{II} compared with the average of the three low concentrations), the release percentage increased approximately 2-fold. The absolute amount of Pt^{II} release was about 6 times greater for high Pt^{II} loading compared with that of low Pt^{II} loading. It should be noted that in the published literature, the plateau percentage of Pt^{II} released ranges between 10% and 100% for carboxylated ligands (on a time scale < 10 d).^[102, 116, 117, 118, 119] Our results fall within this range, but in the lower/weak release performance end. Overall the relatively weak release performance of Pt^{II} observed here can be attributed to the stability of the dicarboxylate complex between Pt^{II} and the Dendron. ^[119] To improve performance, the strength of this complex must be modified,

perhaps through alteration of the ligand structure, [119] a goal that was beyond the scope of the present work.

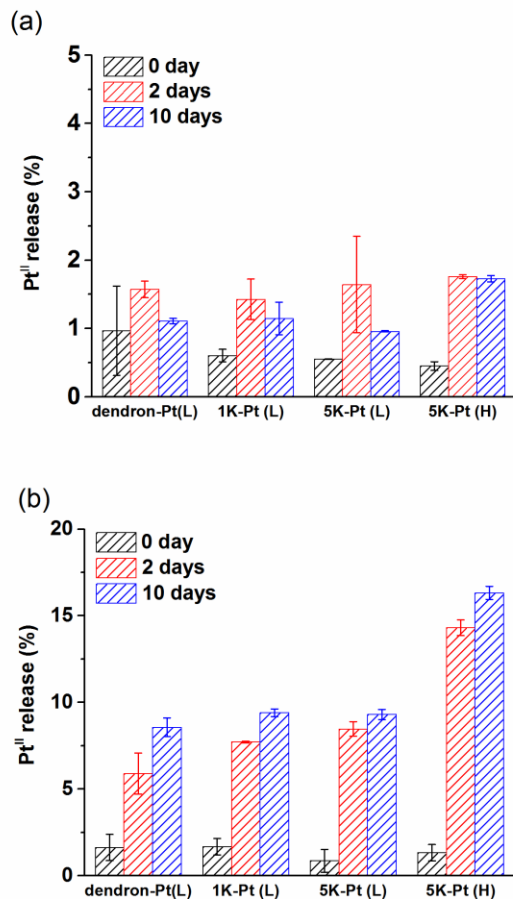


Figure 3.11. Pt^{II} release under (a) PBS and (b) PH 5 (acetate buffer). The platform studied included AuNP-dendron, AuNP-(dendron)-(SH-PEG1K) and AuNP-(dendron)-(SH-PEG5K) at two different Pt^{II} loading concentrations (low Pt^{II}: C_{Pt^{II}} = 1.1 μmol/L and high Pt^{II}: C_{Pt^{II}} = 11.4 μmol/L), which are labeled as Pt (H) (Pt^{II} at high concentration) and Pt (L) (Pt^{II} at low concentration). Error bars represent one standard deviation of two replicate experiments.

3.4 Conclusions

In this chapter, we build upon previous efforts that established the capacity for a novel hyphenated technique, ES-DMA-ICP-MS, to examine, on a quantitative basis, the effects of surface engineering on drug loading and colloidal stability for a model nanoscale anti-tumor drug delivery platform. The model platform consists of cisplatin (Pt^{II}) complexed to a carboxylate-terminated dendron tethered covalently by thiols to the surface of nominally 10 nm diameter AuNPs. In the present study we extend this foundational work to analyze a more complex system containing multiple ligands (SH-PEG and thiolated carboxyl-terminated dendron). We quantify the effects of SH-PEG relative molecular mass and concentration on Pt^{II} loading, and the impact of the dendron ligand on PEG uptake. We also examine the capacity for PEG to improve the colloidal stability of the Pt^{II} -loaded nano-conjugate, its primary role in this system, and the effect of PEG on pH dependent *in vitro* release of Pt^{II} . We showed that SH-PEG uptake is inhibited by the dendron ligand if the ligand is pre-attached to the AuNP surface, but that once bound to the surface PEG does not significantly impact Pt^{II} loading capacity or release performance, while it does substantially improve colloidal stability both in water and in biologically relevant media such as PBS and DMEM. An optimal balance between drug loading and conjugate stability under biologically relevant conditions can thus be achieved. This chapter shows that by employing quantitative and orthogonal measurements, one can monitor and control properties that determine drug delivery efficacy, and by extension the safety, of nano-based drug delivery platforms. The lack of such quantitative measurements is one factor limiting the clinical application of these novel materials.

Chapter 4: Electrospray Differential Mobility Hyphenated with Single Particle Mass Spectrometry for Characterization of Nanoparticles and their Aggregates

4.1 Introduction

Engineered nanoparticles (NPs) in colloidal form have found a wide range of commercial applications. [120, 121, 122, 123] However, when released into the environment, they are unlikely to remain in their pristine manufactured state throughout their lifecycle. Their transport properties and potential interaction with living organisms are highly dependent on their state of aggregation, complexation and dissolution. [124, 125, 126] In order to evaluate the potential impact of nanotechnology on environmental and biological systems, validated analytical tools are critically needed that address challenges posed by real-world samples. This includes environmentally relevant concentrations in the $\mu\text{g L}^{-1}$ to mg L^{-1} range [127] and the capacity to distinguish between and detect changes in different NP states, including size polydispersity, aggregation and adsorption of coatings. Ultimately, the ability to distinguish between naturally occurring and engineered NPs would be highly beneficial.

In this regard, no single analytical tool is available that can fulfill the wide range of characterization needs. One method that has featured prominently in the area of environmental systems is inductively coupled plasma mass spectrometry (ICP-MS). ICP-MS provides rapid and quantitative elemental analysis, and low limit of detection (LOD). More recently, single particle-ICP-MS (spICP-MS) has emerged as a powerful technique to quantify NPs on a particle-to-particle mass basis and to differentiate between dissolved and particulate forms. The potential of using spICP-MS for

simultaneous particle sizing, mass measurement, and particle number quantification at environmentally relevant concentrations has been demonstrated, and further method development and validation are ongoing. [73, 128, 129, 130] Though promising, the technique of spICP-MS has some significant limitations. First, ICP-MS is a mass based analytical tool, thus unless chemical composition, density and shape are known *a priori*, the size of NPs cannot be accurately determined. Additionally, spICP-MS, without further size information, cannot be employed to distinguish between complex NP states, such as aggregate forms, heteroaggregates or particles with coatings (such as proteins). In this respect, an upstream separation tool hyphenated with spICP-MS to pre-sort constituents in a complex sample has the potential to address such limitations by providing independent size information.

While chromatographic pre-separation has been suggested, to our knowledge, the only method directly coupled to spICP-MS to-date is hydrodynamic chromatography (HDC). Pergantis et al. [131] utilized HDC online with spICP-MS for the detection and characterization of metal-containing NPs in terms of number concentration, size and metal content. Subsequent work by Rakcheev et al. [132] explored HDC-spICP-MS to investigate morphology and temporal behavior of aggregation. While HDC has a very low LOD ($\approx \text{ng L}^{-1}$) and can be applied to heterogeneous and complex samples, its resolution (the capacity to resolve multiple populations) was found to be insufficient to separate a mixture of NPs (5, 20, 50 and 100 nm); Efforts must be made to improve resolution by, for example, optimization of flow rates and column length. Furthermore, to obtain size from retention time in HDC requires the calibration with standards, and the influence of surface coatings on retention time complicates the accuracy for size

determination.^[47] Finally, we are aware of on-going efforts to hyphenate asymmetric flow field-flow fractionation with spICP-MS, but to-date published literature is limited to off-line analysis of collected fractions.^[133]

In Chapter 4, we employ electrospray-differential mobility analysis (ES-DMA) as an ion-mobility based size discrimination technique, coupled to spICP-MS. This Chapter serve as a proof-of-concept study to demonstrate the capabilities and advantages of coupling ES-DMA directly to ICP-MS operated in time-resolved single particle analysis mode (i.e., spICP-MS), for characterizing NP size, mass, and number concentration at environmentally relevant concentrations and on a particle-by-particle basis. The simultaneous and independent measurement of NP mass and size makes this coupled approach amenable to characterizing the aggregation state as well as differentiating between polydispersity due to primary size variation and that due to aggregation of primary particles, a critical distinction.

4.2 Materials and Data Processing

Gold NPs (AuNPs) were used as a test bed in this study as they can be readily obtained in a variety of monodisperse sizes, and are available as NIST reference materials. A series of AuNPs were employed in this study including NIST reference materials with nominal diameters of 30 nm and 60 nm (RM 8012 and RM 8013, respectively), and AuNP suspensions with nominal diameters of 40 nm, 80 nm and 100 nm obtained from Ted Pella (Redding, CA, U.S.A.).[¶] The sizes of AuNPs were validated by mobility

[¶] The identification of any commercial product or trade name does not imply endorsement or recommendation by the National Institute of Standards and Technology.

measurement using a customized ES-DMA-CPC system and compared with reference values (Table 4.1). Ammonium acetate (AmAc - Sigma, 99.9%) was used for preparation of buffer solutions for electrospray and for inducing AuNP aggregation. The DMA was calibrated with NIST standard reference material polystyrene spheres (SRM 1963a) with a certified mobility diameter of 101.8 ± 1.1 nm. High purity filtered deionized (DI) water was used to prepare all solutions and suspensions. Formation of AuNP aggregates consisting of primary 40 nm monomers was induced by adjusting the ionic strength through addition of aqueous AmAc. A 4 mL AuNP colloid suspension (40 nm) was centrifuged twice to remove the supernatant containing any excess (unbound) citrate. The centrifuged AuNP suspension was then re-suspended in 1 mL of DI water as a stock suspension, which was confirmed to be colloidally stable over several days. In order to induce aggregation, 50 mmol L^{-1} aqueous ammonium acetate was mixed in equal volume with the AuNP suspension. Prior to conducting single particle measurements by ES-DMA-spICP-MS, the aggregated samples were diluted with 4 mmol L^{-1} AmAc buffer to an appropriate concentration.

Table 4.1 Mobility size measurement of AuNPs

sample	Diameter by DMA (nm)*	Certified diameter (nm)
Nominal 100 nm PSL	100.1	101.8 ± 1.1
Nominal 30 nm AuNP	29.7	28.4 ± 1.1
Nominal 40 nm AuNP	42.8	42.4
Nominal 60 nm AuNP	58.7	56.3 ± 1.5
Nominal 80 nm AuNP	85.2	79.0
Nominal 100nm AuNP	104.4	98.5 ⁻

*The uncertainty of diameter by DMA is consistently less than 1% based on replicate measurements for 30 nm AuNP RM 8012 and PSL SRM 1963a. ⁻ The diameter for nominal 100 nm AuNPs is not available from the provider, but the value of a different batch of the same material from the same provider was utilized.

4.2.1 Operational Mode of DMA-spICP-MS

Unlike many liquid-based fractionation methods or chromatographic separations, the DMA offers flexibility in operation: enabling an arbitrarily chosen mobility size for a pre-determined time by choosing voltage and DMA step time accordingly. And with the fixed voltage, the DMA operates as a band filter to allow one specific size of NPs to exit. Figure 4.1 demonstrates a characteristic “ladder” pattern of increasing intensity for ¹⁹⁷Au spikes (i.e., increasing mass or size) with respect to DMA scanning time *t*, (for each DMA voltage step). Overall, for each “ladder-step” within the DMA step time (i.e., 151 s). In this study, ES-DMA was operated with a sheath flow of 10 L/min

(argon) and an aerosol flow of 1 L/min (air). The ICP-MS was operated in time resolved acquisition mode (TRA), with a dwell time of 10 ms. (i.e. single particle ICP-MS).

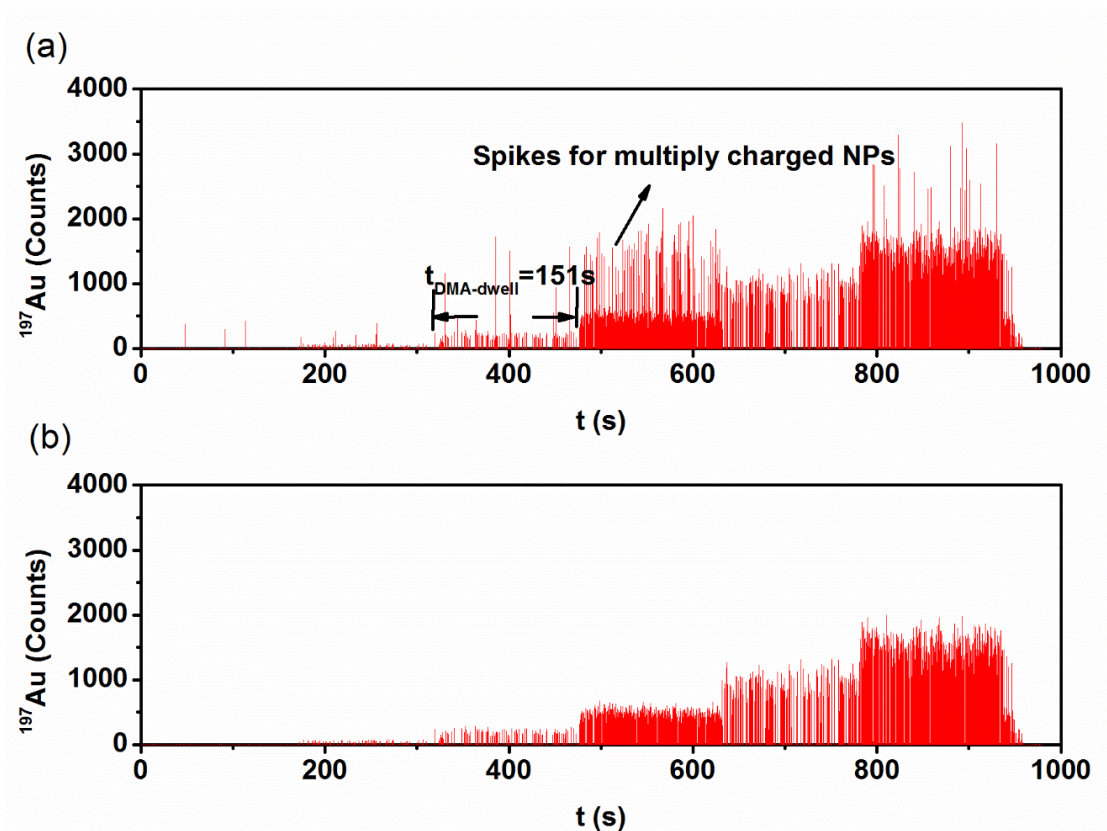


Figure 4.1. A mixture of AuNPs containing 30 nm, 40 nm, 60 nm, 80 nm and 100 nm. The DMA selects, with increasing time, 20 nm, 35 nm, 50 nm, 65 nm, 80 nm and 95 nm and with a DMA step time of 151 s at each selected size. (a) Arrow pointing the few higher intensities compared with mostly low intensity spikes from around 480 s to 650 s, representing multiply charged larger NPs. (b) After removing the multiply charged larger NPs which intensity is higher than 2σ of the mean intensity for each size step.

4.2.2 Distinguishing Particle Events

In spICP-MS, ^{197}Au was recorded in single particle analysis mode with dwell time, t_{dwell} , defining the measurement window for particle events. With an appropriately chosen t_{dwell} , a single intensity pulse represents a single particle event. In this study, 10 ms was chosen to avoid both particle splitting (a single particle event split over two adjacent dwell periods) and coincidence (more than one particle event occurring within a single dwell period). A five-sigma criterion (5σ) was applied to distinguish particle events from background. [128]

The basic criteria for distinguishing a particle event from the background signal is $I_{particle} > \bar{I} + n\sigma$, where $I_{particle}$ represents the signal from a particle event, \bar{I} is the average intensity (background + particle events), σ is the standard deviation of the average intensity and n is a threshold multiplier set to 5 in this study. A previous study demonstrated that $n = 5$ is a good compromise between retaining sufficiently high particle counts and minimizing false positives ($< 0.1\%$). The raw data exported from ICP-MS was recorded as intensity versus time (in counts per dwell time). To process the data, \bar{I} and σ are calculated for the complete data set, and only those pulses satisfying the criteria $I_{particle} > \bar{I} + 5\sigma$ are identified as particle events and subtracted. The same procedure is applied to the remaining data set and repeated until particle events can no longer be distinguished from the background signal. By this method, the particle pulses are separated from the background signal.

4.2.3 Transit time from DMA to ICP-MS Determination

In order to obtain the transit time between the exit port on the DMA and ICP-MS detection, the DMA voltage was applied at $t=150$ s while recording a gradual increase of ^{197}Au intensity until the signal no longer changed. Similarly, the DMA power was turned off at $t=330$ s to observe the time required for the ^{197}Au signal to decay down to the background value. The response time based on these measurements shown in Figure 4.2 is ≈ 15 s, which we define as the transit time.

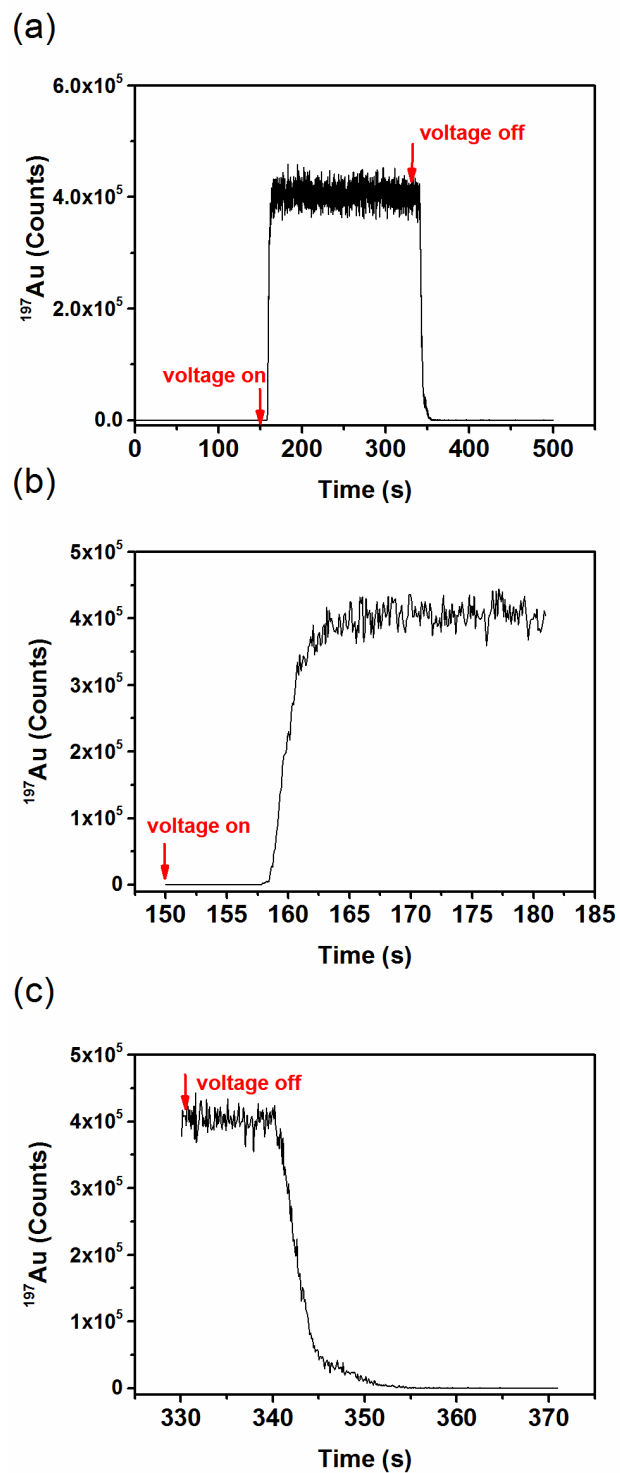


Figure 4.2. NP transit time from DMA to ICP-MS obtained by moderating voltage from the power supply; ^{197}Au signal is recorded with respect to time.

4.2.4 Particle Mobility Size Determination

In our experiments, by stepping the applied voltage, the DMA is operated in a step-wise mode with respect to DMA scanning time, t , so that singly charged NPs are selected as shown on the y-axis in Figure 4.3 inset. Operationally, a mobility step size, $d_{m,step} = 2$ nm, and a step time, $t_{step} = 31$ s, are fixed. The lag time for NPs exiting the DMA to reach the ICP-MS interface was determined to be approximately 15 s ($t_{transit} = 15$ s). Although recorded continuously by ICP-MS with respect to t , this transit time of 15 s has to be subtracted from 31 s yielding 16 s for actual data analysis for an individual step, as indicated by the dashed zone in Figure 4.3 inset. With a spICP-MS dwell time of 10 ms, about 1600 measurements can be performed at each selected mobility size using the current experimental setup. Therefore $d_{m,t}$ for the singly charged state is correlated with DMA scanning time t (i.e., spICP-MS recording time) by Eq. (4.1):

$$d_{m,t} = d_{m,0} + \left[\frac{(t-t_0)}{t_{step}} \right] \times d_{m,step} \quad (4.1)$$

Where $d_{m,t}$ is the spherical equivalent mobility diameter of NPs selected by the DMA at t , $d_{m,0}$ is the initial stepped diameter at t_0 . The bracket in Eq. (4.1) represents the *greatest integer function* such that the DMA selects particle size in a step-wise mode (the greatest integer function rounds to the nearest smaller whole number). For a nonspherical particle (e.g., clusters of NPs), $d_{m,t}$ is the equivalent spherical mobility diameter with the same drag force as the measured particle.

4.3 Discussion

4.3.1 The ES-DMA-spICP-MS spectrum

A typical time-resolved intensity (^{197}Au) spectrum for nominal 60 nm AuNPs obtained by DMA-spICP-MS is presented in Figure 4.3 (raw data before removing background). The detection by spICP-MS yields element-specific intensity spikes, each representing a single particle event generating an ion plume in the plasma. Thus each spike should be directly relatable to the mass of a specific element in one particle. In our case since the particles comprise single component Au, the spike represents the total mass of the metallic core (excluding citrate capping agent). Unlike raw intensity spectra obtained in stand-alone spICP-MS, time on the x-axis is the DMA scanning time, which corresponds to the selected mobility size for singly charged particles (step-mode following Eq. (4.1): blue line in Figure. 4.3). Therefore, a simultaneously correlated size and mass measurement is achieved by the coupling of DMA to spICP-MS. Closer examination of the spectrum shows that the majority of event spikes are narrowly distributed between 200 s and 600 s, which corresponds to a mobility size ranging from 50 nm to 75 nm (i.e., the singly charged nominal 60 nm AuNP population). The doubly charged states of this population have a greater mobility, corresponding to a theoretical mobility diameter from 35 nm to 52 nm. Hence the small number of single particle events below 100 s is attributed to doubly charged particles. As expected, the nominal intensity of the single particle events are of similar magnitude, with average of 280 counts, regardless of the charged state of the particle.

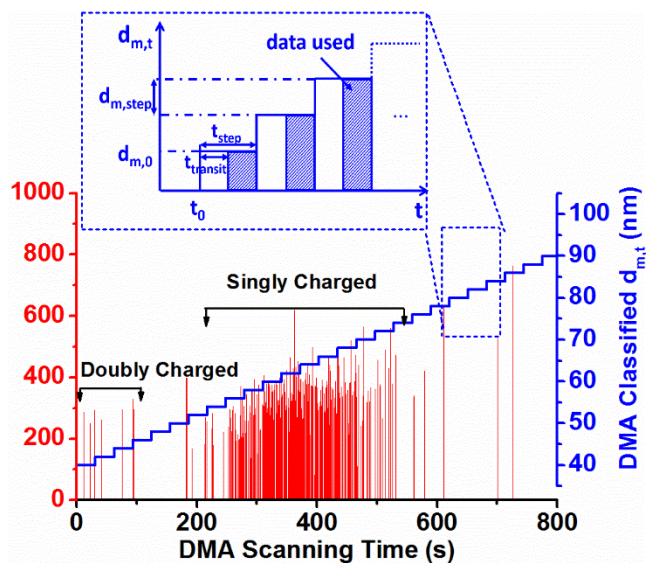


Figure 4.3. spICP-MS intensity spectrum as a function of DMA scanning time for 60 nm AuNPs. Single particle events are presented as red spikes. The $d_{m,t}$ selected by the DMA with respect to time is represented by the stepped blue line following Eq. (4.1) ($d_{m,0} = 20$ nm, $d_{m,step} = 2$ nm, and $t_{step} = 31$ s). Two major populations representing singly and doubly charged 60 nm AuNPs are highlighted by the black brackets. Inset shows operational features of DMA-spICP-MS relevant to data acquisition (Eq. (4.1)).

Overall, there are three independent types of information that can be extracted from the spectrum: *particle mobility size determined by DMA, intensity of each event spike and frequency of spikes*. In the following section, we establish two calibration curves that correlate (1) the intensity to the NP mass, and (2) the frequency of spikes to the NP number concentration. The two calibration curves combined with the known DMA classified size can be used for simultaneous determination of NP mass, size and particle concentration for unknown samples.

4.3.2 Proof of concept studies

4.3.2.1 Measurement of number concentration

In order to explore the capacity of DMA-spICP-MS to measure NP concentration and its sensitivity range, we utilized 60 nm AuNPs, serially diluted to yield a final number concentration ranging from $(3.1 \times 10^6 \text{ to } 7.9 \times 10^7) \text{ mL}^{-1}$ (mass concentration of $6 \mu\text{g L}^{-1}$ to $160 \mu\text{g L}^{-1}$). The number concentration was calculated based on the mass concentration ($51.86 \mu\text{g g}^{-1}$) given on the RM certificate combined with an assumption of spherical shape with a Gaussian fit DMA measured diameter. Figure 4.4(a) illustrates a linear relationship between the number of particles in the aerosol phase detected by spICP-MS and the concentration of NPs in solution (i.e., $N_{spICP-MS}$ and $[NP]$ respectively) with a R^2 value of 0.99999, indicating a high degree of linearity. This demonstrates the capacity of DMA-spICP-MS to quantitatively measure NP concentration in solution for unknown samples with appropriate calibration. For our ES-DMA-spICP-MS system we find that the upper range of concentration for which single particle events are statistically meaningful without significant ($< 5\%$) particle coincidence is $\approx 10^8 \text{ mL}^{-1}$. Above this concentration we observe high mass event spikes corresponding to doublets. A LOD of $3.7 \times 10^5 \text{ NPs mL}^{-1}$ was determined under our experimental conditions from the calibration curve: $Y_{(N_{spICP-MS})} = 2.6 \times 10^{-5} X_{([AuNP 60nm])} + 46.4$ (LOD = $3.3\sigma/S$, where σ = standard deviation of y-intercept from regression line, S = slope of the calibration curve). [134] This leads to a mass LOD of $0.8 \mu\text{g L}^{-1}$ for 60 nm AuNPs. The slope of the calibration curve represents the transfer coefficient (k), which takes into account particle loss channels associated within ES, DMA and ICP-MS. It can be determined by relating NPs detected by DMA-spICP-MS ($N_{spICP-MS}$) to

concentration of NPs in solution, $[NP]$. The total number ($N_{spICP-MS}$) in the aerosol phase detected by spICP-MS was obtained by integrating the peaks for each size NP.

$$N_{spICP-MS} = \int_{d_{m,min}}^{d_{m,max}} \frac{d(N_{raw}/\alpha_c)}{dd_m} dd_m \quad (4.2)$$

Where d_m represents the mobility diameter selected by DMA, and N_{raw} is the raw number of particles detected by spICP-MS at each mobility size d_m for a fixed amount of time t , α_c is the probability that a particle is singly charged (which is size dependent and follows Fuchs' charge distribution). $d_{m,max}$ and $d_{m,min}$ are the upper and lower size limit defining the peak. $N_{spICP-MS}$ is then utilized to obtain the real concentration in solution ($[NP]$) by considering the transfer efficiency for ICP-MS (η_{ICPMS}), DMA (η_{DMA}), and electrospray (η_{ES}).

$$[NP] = \frac{N_{spICP-MS}}{\eta_{ICPMS} \cdot \eta_{DMA} \cdot \eta_{ES}} = \left(\frac{N_{spICP-MS}}{k} \right) \quad (4.3)$$

4.3.2.2 Measurement of Nanoparticle Mass

In order to demonstrate the capability for accurate mass measurement, NPs of different nominal diameters: 30 nm, 40 nm, 60 nm, 80 nm and 100 nm were utilized. The mass of each NP was calculated by assuming that AuNPs have a density equal to bulk gold (19.3 g cm^{-3}) and are spherical in shape. The geometric diameter (equivalent to mobility diameter for spheres) was obtained by a Gaussian peak fit to the particle size distribution measured by DMA-CPC (Table 4.1). The reader should keep in mind that because the DMA resolution is much higher than the width of the size distribution for these nominally monodisperse AuNPs, the DMA must be scanned / stepped over the entire size distribution to obtain a full representation of the population by event spikes. AuNPs of different sizes were measured and the averaged intensities of each size were

used to construct a mass calibration curve versus the mass of a NP calculated from the diameter.

Within the size range studied, a linear relationship is demonstrated between the averaged ^{197}Au intensity, and the Au mass per AuNP as shown in Figure 4.4(b): $Y (^{197}\text{Au Intensity}) = 110.5X (\text{Au mass per NP}) + 3.3$; $R^2 = 0.99995$ This mass calibration curve demonstrates the capacity for the determination of metal mass of unknown NPs from detected spike intensity of an appropriate element. From the calibration curve, a LOD of 0.1 fg (4×10^{35} Au atoms) is obtained, which converts to a AuNP size of about 23 nm. This detection limit (dependent on sensitivity to noise of the ICP-MS instrument) is comparable to the smallest detectable size of 15 nm for AuNPs reported by Hu et al. [135] and the theoretical calculated size of 13 nm obtained by Lee et al. [136]

4.3.2.3 Measurement of particle size distributions

Next we compare the particle size distribution (PSD) of 60 nm AuNPs obtained by DMA-spICP-MS with that obtained from the standard ES-DMA-CPC method. The latter technique was applied as one of the primary tools for development of traceable NIST AuNP reference materials. [137] The CPC detects particles by light scattering from droplets that nucleate and grow on the particles themselves and the LOD for ES-DMA-CPC is reported to be $>10^9$ NPs mL⁻¹. [138]

Using the raw data obtained by DMA-spICP-MS (Figure 4.3), the spikes representing particle events were first resolved from the background based on a 5σ criteria as discussed previously. Then two different methods were applied to obtain particle size distributions. In one approach, where the ICP-MS was used exclusively as a particle

counter, the number of particle spikes occurring over the step time of a mobility size were summed, and this process was repeated for each size step to yield a number-based PSD as shown in Figure 4.4(c) (designated as “Method-1”). In the second method, the intensities of all particle spikes were converted to mass using the mass calibration curve (Figure 4.4(b)). Based on spherical geometry and the density of Au, the mass was converted to size and the distribution was obtained and designated as “Method-2”, in Figure 4.4(c). The PSDs obtained from DMA-spICP-MS, either by counting NP frequency at a specific size, or by converting NP mass to diameter, are internally consistent and consistent with the PSD obtained by the traditional ES-DMA-CPC (“Method-3”, in Figure 4.4(c)). This clearly demonstrates that for a near monodisperse PSD of the type examined here, the mass resolution and counting ability of the DMA-spICP-MS yields accurate size distributions.

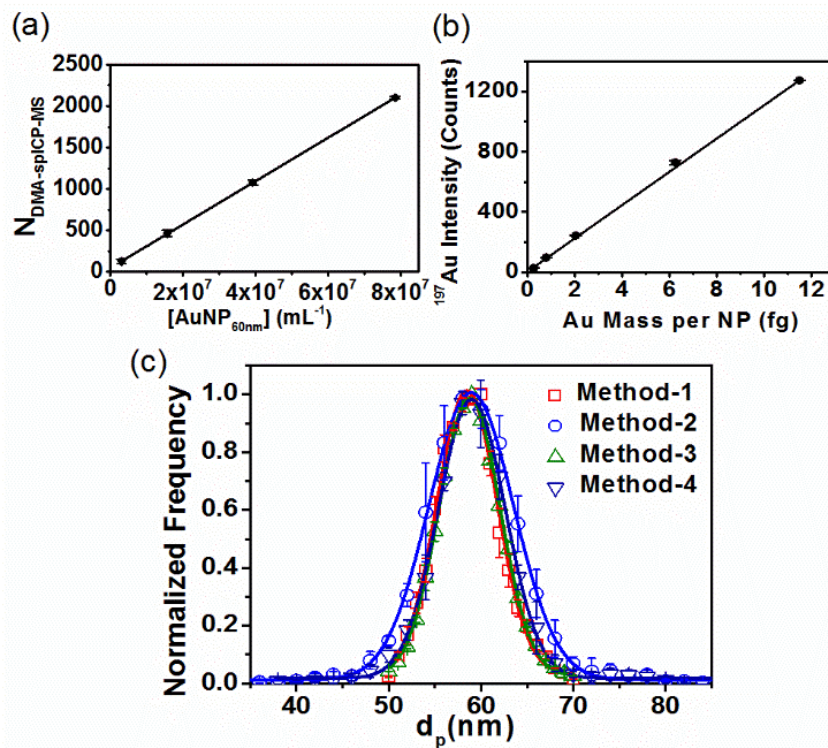


Figure 4.4. (a) Number concentration calibration curve (60 nm AuNP). (b) Mass calibration curve based on AuNPs of various sizes (30 nm, 60 nm, and 40 nm, 80 nm and 100 nm AuNPs). Au mass per NP was calculated based on DMA mobility equivalent spherical size. (c) Comparison of PSD for 60 nm AuNPs measured by DMA-spICP-MS and other conventional methods: Method-1: by summation of particle spikes over each DMA step by DMA-spICP-MS; Method-2: by single particle event intensity from DMA-spICP-MS; Method-3: by conventional DMA-CPC; Method-4: by single particle event intensity from conventional stand-alone spICP-MS. Lines represent Gaussian fits applied to each set of data. Error bars, if not visually apparent, are smaller than the symbols and are based on one standard deviation from at least two replicate runs.

The FWHM was calculated for the Gaussian fits. The FWHM (7.7) for the PSD obtained by counting single particle event spikes (Method-1) was essentially equivalent to that (7.8) obtained by DMA-CPC (Method-3). This is reasonable, since in the case of single particle event counting, the size binning is determined by the DMA; in this case the spICP-MS is utilized as an ultra-sensitive particle counter, and thus functionally similar to a CPC. The PSD obtained based on DMA-spICP-MS particle intensity (Method-2) has a slightly wider breadth (FWHM=10.8) in comparison to the other two methods (Method-1 and Method-3). The FWHM in PSD obtained from the single particle intensity by conventional stand-alone spICP-MS (Method-4) is 8.6, which is intermediate between the DMA-size based (Method-1 and Method-3) and Method-2.

Results indicate that the nature of determining size (either by DMA or by conversion from spICP-MS particle intensity) has an influence in the resulting width of the PSD. For the case examined here, DMA yields a narrower PSD in comparison to a single particle intensity based method (i.e., better resolution). The reason for the difference in FWHM, comparing Method-2 to Method-4, is not clear at this point. One likely attribution is the different operating condition in ICP-MS, which influences single particle intensity for each event (e.g., gas introduction for DMA-spICP-MS in comparison to liquid introduction for conventional stand-alone spICP-MS). Considering the error bars (precision) from the PSD, the PSDs with the exception of Method-2 are essentially indistinguishable. The upper size limit for our study is around 150 nm, which is primarily limited by the breakdown voltage of argon used as sheath flow in the DMA. An improvement in efficiency for the GED would permit the use of

air (with higher breakdown voltage) as the sheath flow, and thereby expand the applicability to sizes of several hundred nm.

4.3.3 Resolving mixed populations

In order to evaluate the robustness of DMA-spICP-MS, we turn to a problem of more practical relevance, that of particle mixtures, using a 5-component AuNP sample with sizes ranging from 30 nm to 100 nm. For these experiments the number concentration of NPs of various sizes were adjusted to a nominally equivalent basis, based on independent spICP-MS measurements. Figure 4.5(a) is a 3-D contour map and heat map showing simultaneously the measurement of NP mobility size, NP mass (intensity per NP) and NP concentration (frequency of NPs). Populations of AuNPs of different sizes are clearly distinguishable from each other, demonstrating the superb resolution obtained by coupling DMA with spICP-MS.

For spheres one would predict a linear relationship between mobility diameter (d_m) and 1/3 power of ^{197}Au intensity ($\text{mass}^{1/3}$). This is clearly apparent in the heat map of Figure 4.5(a), as the five NP populations lie on a diagonal. The off-diagonal populations, which are obviously fewer in number, located above the diagonal correspond to doubly charged NPs, while the populations below the diagonal are indications of split particle events.

This pattern if obtained for an unknown sample should also indicate that the particles in the mixture are largely spherical and in an unaggregated state (as will be shown in section 4.3.4-4.3.5). Furthermore, the diagonal also implies that there is no significant coating on the particle, because otherwise, the coating would bias particles of the same

^{197}Au mass toward a larger mobility size and would appear below the diagonal line. Therefore, independent and simultaneous quantification of both size and mass provides rich information regarding the NP state (e.g., shape, state of aggregation, and coating information), which is not possible using stand-alone spICP-MS. Utilizing 60 nm AuNPs for single-point calibration of concentration, the measured particle number concentration for all five populations are consistent with the known concentration initially in the mixture (Figure 4.5(b)). This implies high fidelity of the system in measuring number concentration, size, and mass simultaneously as well as providing NP states information.

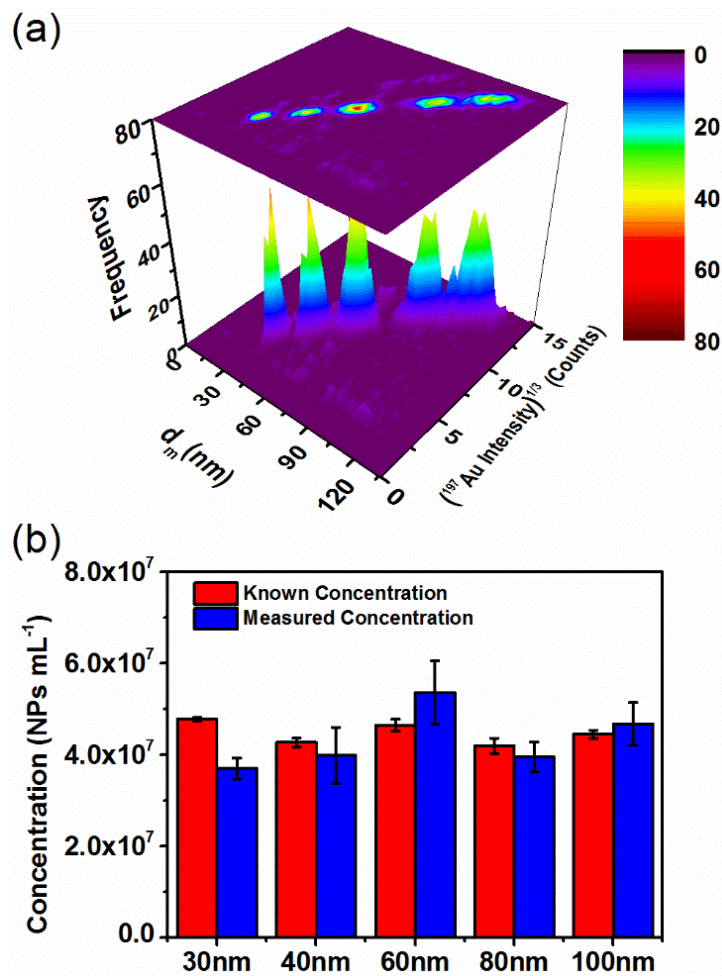


Figure 4.5. (a) Plot of size, mass^{1/3} (i.e., (¹⁹⁷Au intensity)^{1/3}) and concentration (frequency of NPs) for mixtures containing five sizes of AuNPs as obtained by ES-DMA-spICP-MS. (b) Comparison between measured and known NP concentration initially mixed for five different sizes. Error bars represent one standard deviation for three replicate measurements. The known concentration initially mixed was based on independent relative number concentration measurement for all five different sizes by stand-alone spICP-MS and normalized to known 60 nm AuNPs concentration from certificate.

4.3.4 Analysis of discrete aggregates

Here, we examine a fundamental issue frequently encountered in colloidal systems, that of particle aggregation and the ability to quantify both the process and the products. In Figure 4.6, we present results clearly demonstrating the capacity of DMA-spICP-MS to differentiate discrete aggregates, and track aggregation temporally, in this case over a 9 d period. As singlet primary 40 nm AuNPs aggregate, the mass for N -mers (discrete aggregates composed of N primary particles) increases linearly with N ; similarly, for DMA the mobility size will increase, but will follow a non-linear function of N (i.e., independent confirmation of aggregate number is required).

Distinguishable populations of NP oligomers are presented as islands (heat map) associated with the peaks in Figure 4.6. For day 1 after initiation of aggregation, two populations are clearly resolved and distinguished from each other (Figure 4.6(a)). As the aggregation process propagates, aggregates with larger size and mass appear, forming a continuum of discrete aggregation states in solution. In Figure 4.6(b), three peaks are clearly resolved on day 9 of aggregation, while two additional low height peaks appear at larger sizes forming a tail (see Figure 4.7). The first (smallest size) peak (in bin 44 nm to 46 nm) with maximum height is identified as the monomer 40 nm AuNPs ($d_m = 42.8$ nm, see Table 4.1). In order to assign the remaining peaks, each spike intensity contributing to the peak was normalized to the intensity of 40 nm monomers, resulting in normalized intensities of 1, 2, 3, 4 and 5. In other words, the normalized intensities correspond to monomers, dimers, trimers, tetramers and pentamers of the aggregating AuNPs, since intensity (correlating to particle mass) linearly increases with the number of primary NPs associated with a given aggregate. In these studies the

samples were first diluted to appropriate concentration to avoid particle coincidence. However, as aggregation proceeds number concentration decreases, and thus by day 9, the dilution employed was 8x lower than day 1 so as to obtain similar spICP-MS spike frequency. This difference in dilution factor would need to be accounted for if the objective were quantitative kinetic information.

A more challenging test of DMA-spICP-MS is to explore its suitability to differentiate NP aggregates from mixtures of solid spherical NPs that vary in size. This is a substantial challenge for either stand-alone spICP-MS or DMA. However, due to the fact that DMA-spICP-MS offers an independent measurement of both mass and size (i.e., density), the approach offers a unique capability to differentiate NP states. As mentioned previously, the mixture of spherical NPs lies diagonally on a graph of $(^{197}\text{Au})^{1/3}$ versus d_m . In contrast, the aggregated sample clearly exhibits a deviation from the diagonal (indicated by the dashed white line in Figure 4.6(c)). More specifically, the peak trail in the heat map for the aggregated sample lies below the diagonal for mixtures of spheres, indicating that for particles with the same mass as spheres, a larger d_m is observed. This is due to the fact that the non-spherical and less compact structure of aggregates presents a larger drag force relative to a sphere of equivalent mass.

These results show that the hyphenation of DMA with spICP-MS can be used to track aggregation temporally, resolve aggregate distributions and distinguish solid spheres from aggregates. The following section will demonstrate quantitative differentiation of aggregates and spheres by defining an apparent density parameter.

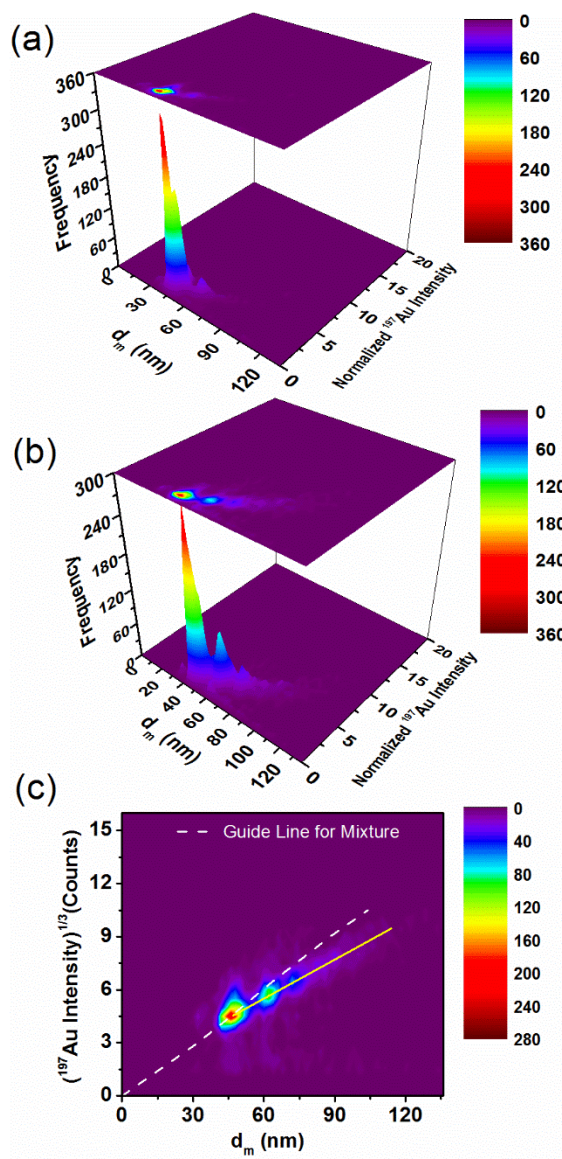


Figure 4.6. Heat map showing aggregation of 40 nm AuNPs occurring over 9 d ((a). day 1 and (b). day 9); ^{197}Au intensity was normalized to that of the first monomer peak. (c) Comparison of discrete aggregates with the expected results for a mixture of solid spheres.

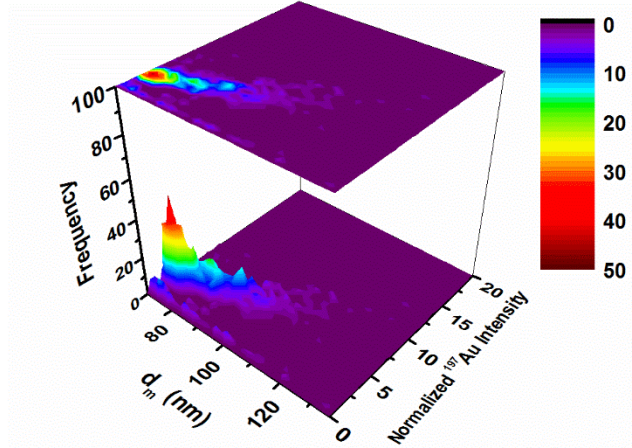


Figure 4.7. Observation of higher aggregates at low concentration for day 9 aggregation; size axis begins at 70 nm. The color scale was reduced so that three distinct peaks are observable (i.e., the aggregates on day 9).

4.3.5 Apparent Density for Aggregates

One can also apply a more quantitative approach by defining a “mobility-based apparent density” (ρ_a) to characterize the state of aggregation:

$$\rho_a = \frac{m_a}{\frac{\pi}{6}(d_{m,a})^3} \propto \frac{I_a}{d_{m,a}^3} \quad (4.4)$$

where m_a represents the mass of NP aggregates measured by spICP-MS intensity I_a for each particle event calibrated using spherical 60 nm AuNPs. $d_{m,a}$ is the measured mobility diameter as previously defined, and the function $\pi/6(d_{m,a})^3$ represents the volume of a sphere that has the same mobility as the aggregate. Eq. (4.4) represents an apparent density for the measured particle. Thus for a particle with an apparent density less than the theoretical solid bulk density, we conclude that this particle must be an

aggregate. Figure 4.8(a) shows apparent density for a mixture of different size spherical solid AuNPs. Five distinct populations are clearly resolved with similar apparent density centered just below 20 g cm^{-3} , which is close to the expected density based on the known bulk density of Au (19.3 g cm^{-3}). By contrast, Figure 4.8(b) shows a decreasing apparent density with respect to size for aggregates of primary 40 nm AuNPs. As aggregates form, the apparent density decreases from just less than 20 g cm^{-3} for spherical monomers to approximately 12.5 g cm^{-3} for discrete aggregate states. The decreasing apparent density results from the formation of less compact NP aggregates. A decreasing relative density for agglomerates has been observed using hyphenation of HDC with spICP-MS.¹³² However that work presents the results as an average over the whole distribution, while in this work we are able to both identify aggregates, and assign an apparent density to each oligomer state. In this way ES-DMA-spICP-MS offers the opportunity to quantitatively assess the state of aggregation and the aggregation number of discrete populations.

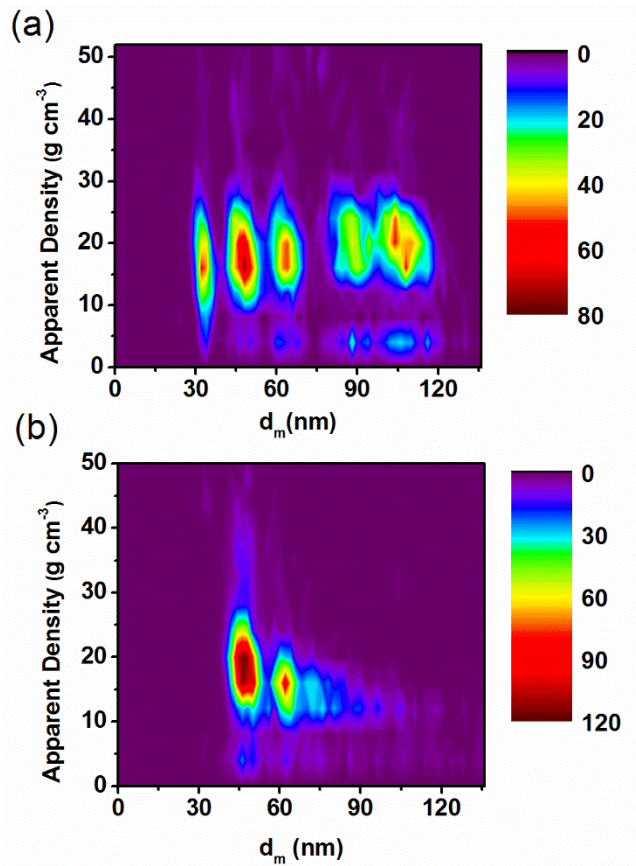


Figure 4.8. Heat maps for mobility-based apparent density: (a) NP mixtures containing 30 nm, 40 nm, 60 nm, 80 nm and 100 nm AuNPs. (b) Aggregates consisting of 40 nm primary AuNPs. The map indicates a small population with apparent density of 40 g cm^{-3} , which we attribute to particle coincidence and that around 4 g cm^{-3} are due to particle splitting.

4.3.6 Resolving AuNPs from medium containing Au^{3+}

Finally, the background signal with DMA hyphenation is lower relative to direct analysis of aqueous NP suspensions (particularly in the presence of dissolved ionic forms). This is because there is no interference arising from dissolved ions in solution

(Au³⁺), as they are pre-classified as “salt” particles leaving a clean gas phase for injection into the plasma. Therefore, the hyphenation of DMA with spICP-MS offers the advantage of reduced background and better detection of NP populations relative to conventional stand-alone spICP-MS. This capability is demonstrated by mixing AuNP with different concentrations of dissolved Au³⁺. It is clearly shown in Figure 4.9 that DMA-spICP-MS classified dissolved Au³⁺ ahead of AuNP signal and therefore generated much cleaner background ((e)-(h) in comparison to (a)-(d)). The result of this cleaner background is the capability to better resolved AuNP signals from dissolved ionic backgrounds. As shown in Figure 4.10, spICP-MS alone is not able to resolve the whole population of AuNP at 0.1ppb of dissolved Au³⁺ (i.e. only half of the AuNP peak is resolved from background). However with cleaner background provided by DMA-spICP-MS, it is capable to resolve the whole AuNP signal population even at Au³⁺ concentration of 6.5 ppm.

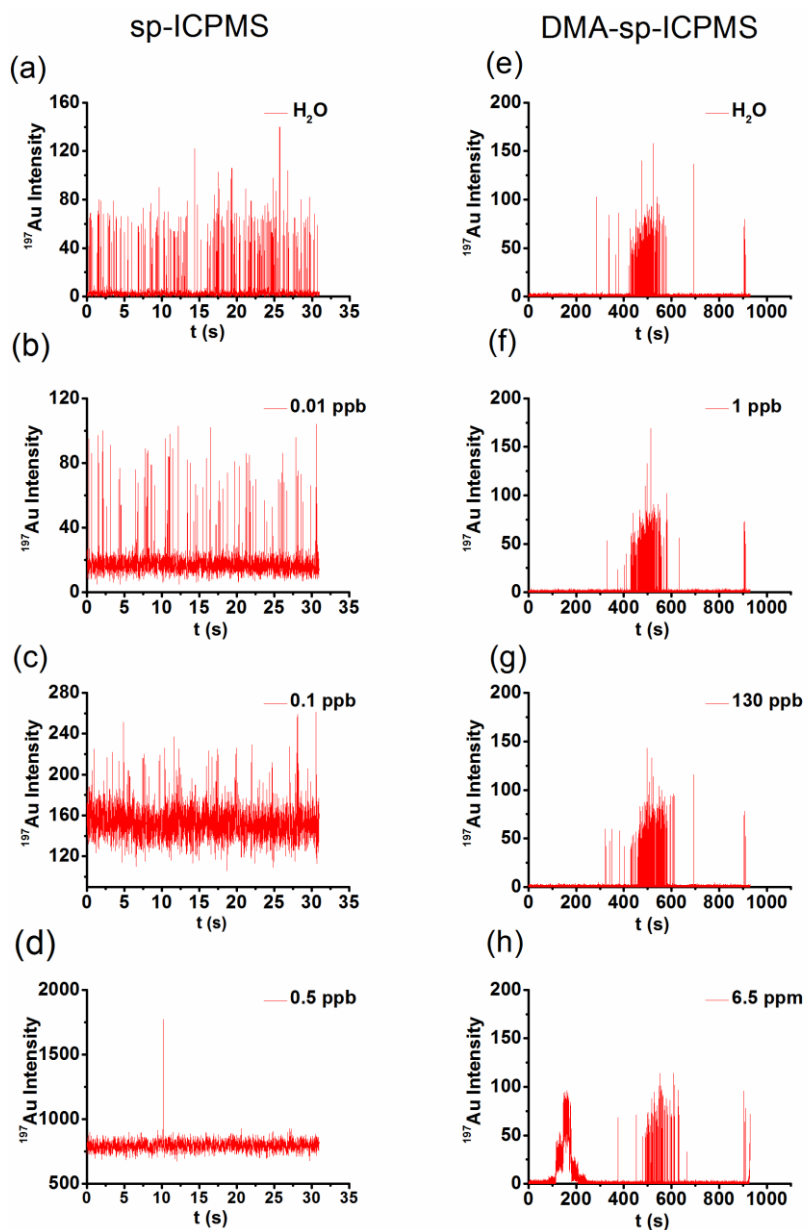


Figure 4.9. Time resolved intensity spectrum for 30 nm AuNPs in medium containing Au^{3+} by both stand-alone spICP-MS and DMA-spICP-MS. Dissolved Au^{3+} ranges from $0.01 \mu\text{g L}^{-1}$ (ppb) to 6.5mg L^{-1} (ppm) with a fixed AuNP concentration of $0.001 \mu\text{g L}^{-1}$ (ppb) for stand-alone spICP-MS and $13 \mu\text{g L}^{-1}$ (ppb) for DMA-spICP-MS. In DMA-spICP-MS, dissolved Au^{3+} is either insignificant (e)-(g) or pre-classified by DMA yielding a small “salt” peak between 0 s and 200 s (h).

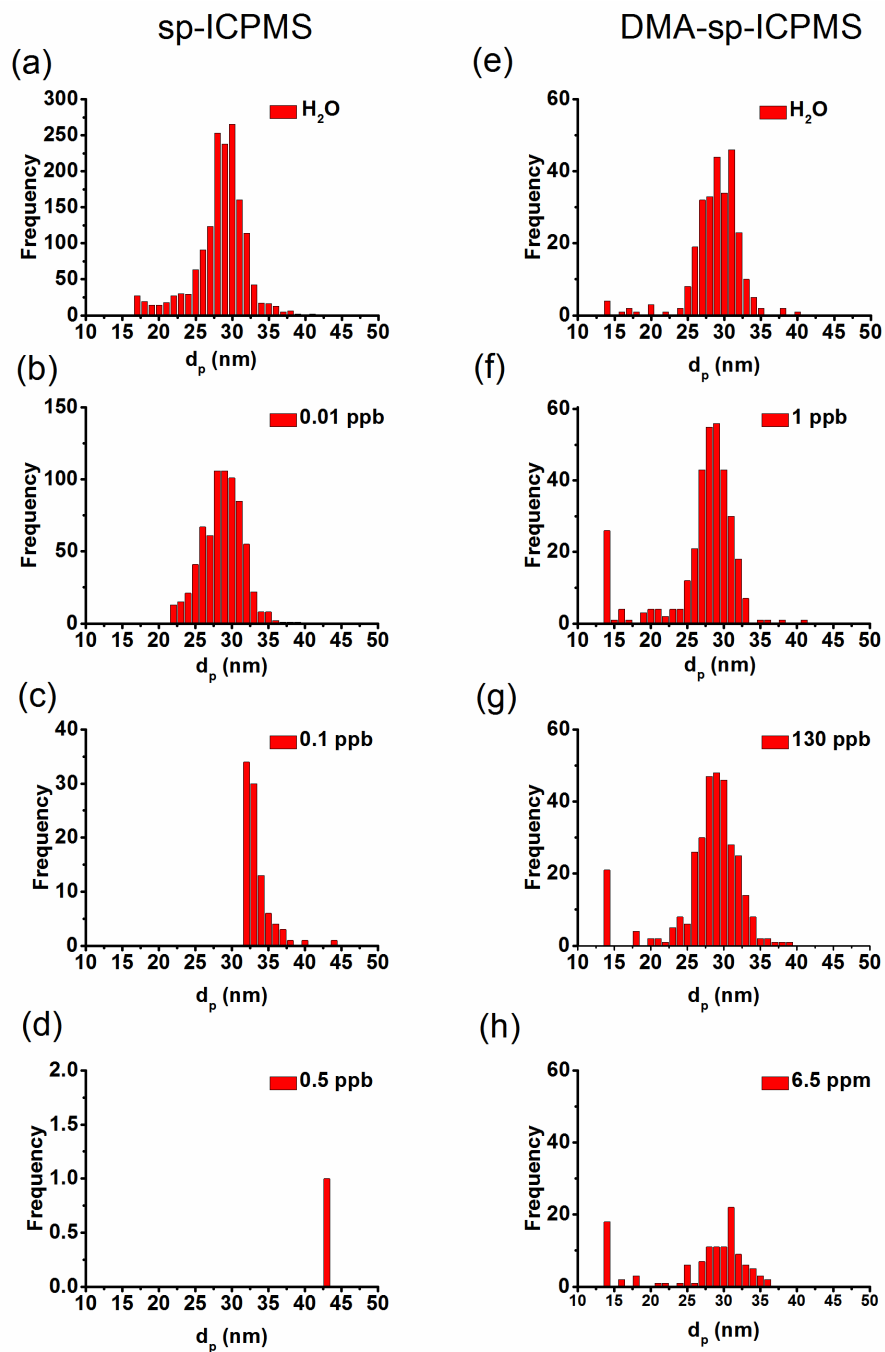


Figure 4.10. Particle size distribution for 30 nm AuNP in medium containing Au^{3+} measured by both stand-alone spICP-MS and DMA-spICP-MS corresponding to Figure 4.9.

4.4 Conclusions

The capacity of ES-DMA-spICP-MS for simultaneous determination of NP size, mass and concentration, and the analysis of complex mixtures and aggregated samples was clearly demonstrated using AuNPs. The high size resolution and tunability associated with DMA, combined with the low LOD, single particle detection and elemental specificity of spICP-MS, permits not only resolution of different NP populations, but also enables the detection of different aggregate states (oligomers) with a defined apparent density at environmentally relevant concentrations. Meanwhile the operational flexibility of ES-DMA allows for selection of a specific particle size and step time, both simplifying and expanding the capabilities of stand-alone spICP-MS as it has been implemented to-date. The concurrent improvements in the spICP-MS technique (both data processing and hardware capabilities), leading to increased sensitivity and faster dwell times, is pushing the lower size limit downward and improving the overall statistical quality of data. Overall the coupling of mobility analysis with spICP-MS offers what we believe to be a substantial and novel advancement in the characterization of NP populations.

Chapter 5: Fast quantification of nanorod geometry by DMA-spICP-MS

5.1 Introduction

Rod shaped metallic nanoparticles have found increasing applications in various fields including biomedical, catalysis and electronics [139, 140, 141, 142, 143]. Gold nanorods (GNRs) have been used in diagnostics, [144] biosensors, [145] and hyperthermal therapy, [146] due to their size-dependent localized surface plasmon resonance (SPR). Rod shaped metal oxides, such as Fe₃O₄, CeO₂, TiO₂ and others have been employed as catalysts or essential components for heterogeneous catalysis applications. [139] The geometry (i.e., length and diameter) of the rod is often crucial in determining the properties of interest, and can influence final utilization. Therefore, the control of geometry during and post synthesis requires rapid and reliable analytical tools.

TEM imaging is the most frequently used method to obtain geometries of nanorods; however, a sufficiently large number of particles must be counted to obtain statistically reliable results, which can be costly and laborious. Furthermore, artifacts such as aggregation can be produced during sample preparation for TEM analysis.

Efforts have also been made to relate GNR geometries with unique spectral features. [147, 148, 149, 150, 151]. For instance, Link et al. [147] modeled the optical absorption spectra of GNRs and derived a simple relationship between the longitudinal surface plasmon resonance (LSPR) absorption maximum and the aspect ratio. The extraction of geometric parameters is primarily based on electromagnetic modeling and with the assist of priori knowledge of mean diameter and end shape. [152, 153, 154] Hu et al. [155] developed a more convenient method from spectral fitting by establishing LSPR

relations for GNRs, and achieved reliable results. However, such simulations require significant expertise in the fundamental theories and therefore are not widely available to non-experts. Applications are limited to well-defined gold nanorods, and are not readily extendable to non-SPR nanorods, such as hybrid metal rods or metal oxides. This approach becomes considerably more complex and less accurate when dealing with a mixture of geometries or length/diameter distributions.

Since for a cylindrical shaped particle, mass is a function of diameter d_r and length L_r , combining the independent information from mobility (i.e., derived from DMA measurement) with mass (i.e., derived from spICP-MS), d_r and L_r are theoretically calculable and can be performed in a single hyphenated measurement. An analogous though off-line approach was explored by Nguyen et al., [156] where fractions from a polydisperse commercial GNR sample were collected following separation by asymmetric flow field flow fractionation. Off-line analysis of fractions was performed using spICP-MS to extract length; the diameter was obtained from independent TEM imaging and assumed constant in this study.

In Chapter 4, I have explored hyphenation of DMA with spICP-MS for simultaneous and accurate measurement of size, mass and concentration, and validated using NIST Au nanoparticle reference materials. [137] In Chapter 5, work is extended to non-spherical particles and the simultaneous characterization of nanorod diameter and length, while demonstrating the capacity to obtain statistically meaningful measurements in minutes at very low particle concentrations. Finally, we use this approach to distinguish nanorod populations from spherical impurities in a mixture, a measurement critical for manufacturing quality control.

5.2 Materials and Methods

Cetyltrimethylammonium bromide (CTAB) stabilized GNRs in aqueous suspension were obtained from Nanopartz (Loveland, CO, USA) and citrate stabilized GNRs were obtained from NanoComposix (San Diego, CA, USA). LSPR bands for the nanorods range from 600 nm to 1400 nm. The naming scheme presented in Table 5.1 indicates the surface coating and the LSPR. For example, CIT-660 refers to citrate capped nanorods with LSPR at 660 nm. There are two nanorod samples with LSPR at 850 nm, but they differ in diameter (20 nm and 40 nm). To distinguish between these two, we included their diameters in the sample name: *viz.* CTAB-20-850 and CTAB-40-850. NIST Reference Material 8013 (Gold Nanoparticles, Nominal 60 nm Diameter) was used as a calibration standard for spICP-MS. Ammonium acetate (sigma 99.9 %) was used as a buffer solution for the electrospray process to generate charged aerosols from aqueous suspensions. Nanorod samples were first diluted in ammonium acetate to the desired concentration just prior to analysis. Electron microscopy grids (carbon and lacey carbon films) were purchased from Ted Pella (Redding, CA, USA).

Transmission electron microscopy (TEM) was performed using a JEOL-2100 FEG (JEOL, Peabody, MA, USA) with an accelerating voltage of 200 kV. To obtain the geometries of GNRs (Table 5.1), one drop of each aqueous GNR sample was drop-cast onto carbon coated TEM grids. To examine the surface coating of GNRs after electrospray treatment, GNRs were selected at the peak mobility using the DMA as a bandpass filter and directly deposited electrostatically onto a lacey carbon film for TEM imaging. Nanometer Aerosol Sampler (model 3089, TSI Inc., Shoreview, MN)

was used for electrostatic deposition. The operation of DMA-spICP-MS is the same as in Chapter 4.

5.2.1 Basis of ES-DMA-spICP-MS in quantifying nanorod geometry

Particle mobility size is commonly expressed as an equivalent spherical diameter, (i.e., electrical mobility diameter) regardless of the actual particle shape. Electrical mobility diameter represents the diameter of a sphere that has the equivalent mobility of the analyte. For a spherical particle, the electrical mobility diameter is equivalent to its geometric diameter. However, for non-spherical particles, the measured electrical mobility diameter is a function of both particle shape and particle orientation during transit through the DMA. For simplicity, our model was built on an assumption that the GNR is a cylindrical shape with flat end-caps defined by two geometrical parameters: *viz.* diameter (d_r) and length (L_r). In such cases, and by operating at low voltage (i.e., < 2kV), fully random orientation is achieved. The capacity for ES-DMA-spICP-MS hyphenation to determine d_r and L_r relies on the fact that it provides simultaneous characterization of mobility diameter, $d_{m,r}$, from DMA and mass, m_r , (or volume, v_r , if density is known) from spICP-MS intensity. In this case, $d_{m,r}$, m_r , d_r and L_r are related as follows:

$$d_{m,r} = ((d_r + \Delta d_{gas})(L_r + \Delta d_{gas}) + \frac{1}{2}(d_r + \Delta d_{gas})^2)^{\frac{1}{2}} \quad (5.1)$$

$$I_r \propto m_r = \rho v_r = \rho \left(\pi \left(\frac{d_r}{2} \right)^2 L_r \right) \quad (5.2)$$

Where I_r is the ICP-MS event intensity generated by a GNR of mass m_r . With two equations ((5.1) and (5.2)), two unknowns (d_r , L_r) are obtainable. The Infinite diameter

of the bath gas molecule in DMA, Δd_{gas} , was added to both d_r and L_r . (The inclusion of bath gas diameter makes the mobility model more accurate). [157, 158]. In our case, $\Delta d_{gas} = 2 \times 0.34$ nm for argon.

The least squares method was used to search for the optimal combination of d_r and L_r , such that the calculated $d_{m,r}$ and m_r from Eq. (5.1)-(5.2) yield the best fit to the measured $d_{mr,0}$ and $m_{r,0}$. Mathematically,

$$\left(\frac{v_r - v_{r,0}}{v_{r,0}}\right)^2 + \left(\frac{d_{m,r} - d_{m,r0}}{d_{m,r0}}\right)^2 == \textit{minimum} \quad (5.3)$$

5.2.2 Procedure

For each GNR sample, the mass-weighted mobility size distribution was determined by DMA-ICP-MS in non-single particle mode (Figure 5.1(a)). The sample was then diluted to an appropriate concentration for spICP-MS measurement. The limit of detection for the DMA-spICP-MS in terms of concentration and mass was described in our previous work. [159] GNRs selected at the peak mobility diameter ($d_{m,r}$) are representative of the central population. Experimentally, the DMA was set at a specific voltage corresponding to the peak mobility for an observation time, t , during which the ICP-MS was operating in time resolved single particle mode to detect single GNR events. Figure 5.1(b) shows the raw spectrum for the spICP-MS signal, each spike representing one GNR event. A 5σ criteria was used to distinguish particle events from the background. [128] The intensity of each spike was then converted to a frequency histogram (Figure 5.1(c)) to obtain the mean intensity by a Gaussian fit. With appropriate calibration by reference material (NIST RM8013), the mean intensity was then converted to the mean mass (or volume, v) for a single GNR event. For this we

calculated the mass (or volume, v) of RM8013 based on the TEM mean diameter with assumed spherical geometry. Therefore, volume per intensity was calculated (from RM8013) and was utilized to obtain the volume of the GNR based on mean intensity from Figure 1(c). Finally, $d_{m,r}$ and v were utilized by the least squares method (i.e. Eq. (5.3)) to obtain d_r and L_r .

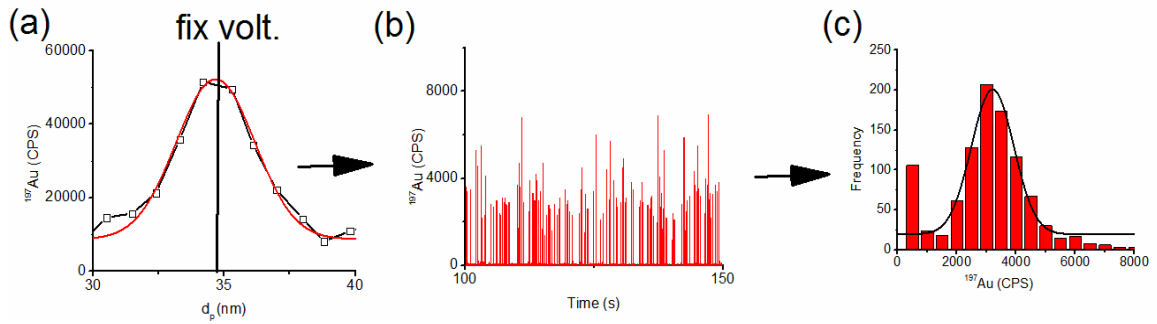


Figure 5.1. Procedure to determine mobility diameter ($d_{m,r}$) and volume (v_r) by DMA-spICP-MS method. (a) Intensity (volume) based mobility size distribution by DMA-ICP-MS (ICP-MS operates in non-single particle mode ($t_{dwell} = 0.5$ s), ^{197}Au in counts per second (CPS) was reported). Peak maximum represents the $d_{m,r}$ of the central tendency of the GNR population. For samples diluted to appropriate concentration, DMA was set at a voltage corresponding to the peak $d_{m,r}$. GNRs corresponding to this voltage were then delivered to the ICP-MS operated in single particle mode ($t_{well} = 10$ ms). (b) spICP-MS signal for GNRs selected at peak $d_{m,r}$. (c) Intensity distribution for (b). Peak of the Gaussian fit to histogram in (c) was used as the mean intensity to calculate v_r .

5.3 Discussion

5.3.1 Characterization of GNRs by TEM

A representative wide range of GNR dimensions were selected in order to validate the DMA-spICP-MS method. These dimensions include d_r (11.8 nm to 38.2 nm), L_r (47.1 nm to 151.7 nm) and aspect ratio (1.8 to 6.9). The surface coating and suspending medium for GNRs were obtained from the vendor. The dimensions d_r and L_r were independently determined by TEM and representative images are shown in Figure 5.2. Around 200 GNRs were measured, and the mean and standard deviation are summarized in Table 5.1. Vendor provided d_r and L_r were also provided for comparison in Table 5.2.

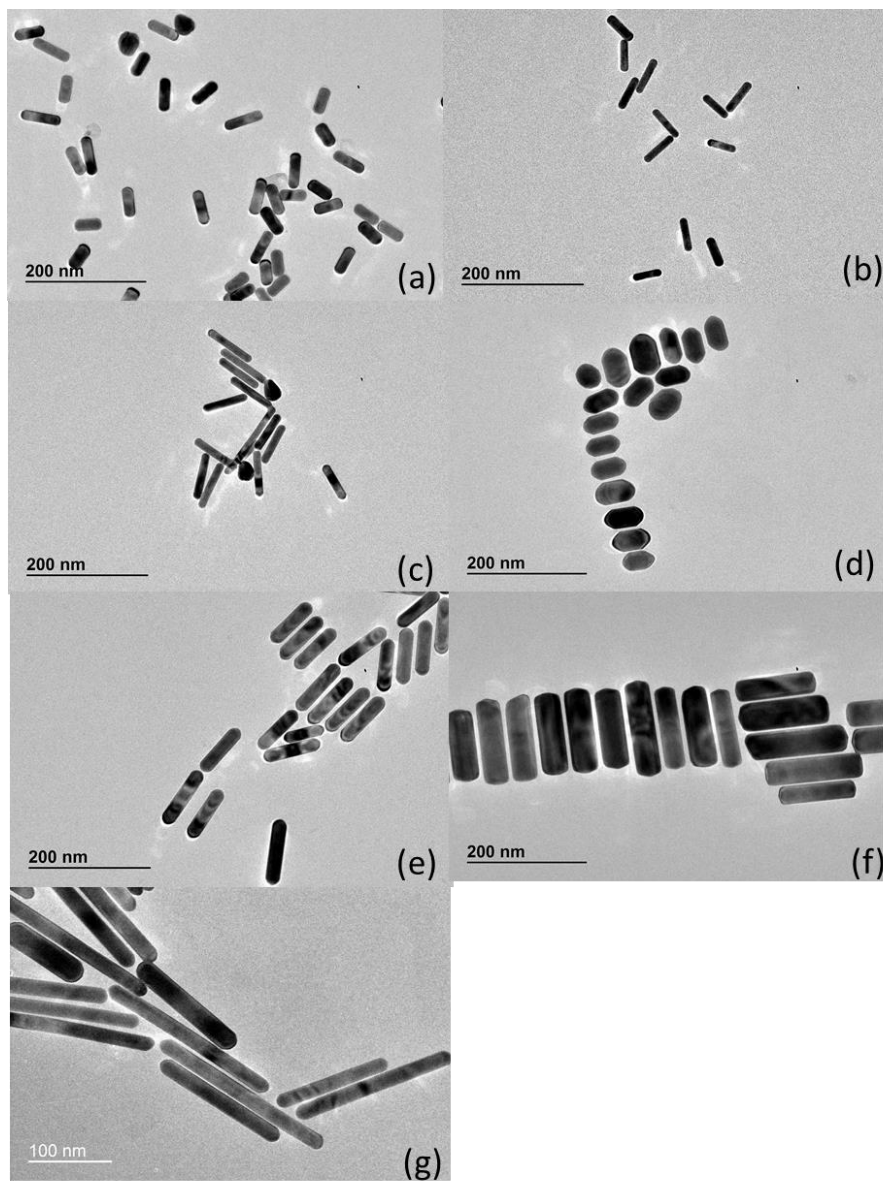


Figure 5.2. TEM image for GNRs (a) CIT-660 (b) CIT-800 (c) CIT-980 (d) CTAB-600 (e) CTAB-20-850 (f) CTAB-40-850 (g) CTAB-1400

Table 5.1. Characterization of GNRs by TEM

GNRs	Dimeter (d_r, nm)	Length (L_r, nm)	Aspect Ratio (AR)	Surface / Medium *
CIT-660	17.5±1.2	47.1±6.7	2.7±0.5	Citrate / Water
CIT-800	11.9±1.3	51.4±5.3	4.3±0.6	Citrate / Water
CIT-980	11.8±1.1	70.4±9.2	6.1±1.2	Citrate / Water
CTAB-600	30.9±4.6	56.4±7.4	1.8±0.2	CTAB/3mmol/L CTAB
CTAB-20-850	20.7±1.4	89.6±12.8	4.3±0.6	CTAB/3mmol/L CTAB
CTAB-40-850	38.2±4.2	135.4±12.7	3.6±0.5	CTAB/3mmol/L CTAB
CTAB-1400	24.6±7.2	151.7±54.1	6.9±3.7	CTAB/5mmol/L CTAB

*The medium information is obtained by vendor.

Table 5.2. Geometries for GNRs provided by vendor (TEM)

GNRs	Diameter (d_r, nm)	Length (L_r, nm)	Aspect Ratio (AR)	Ratio
CIT-660	17.4 ± 1.2	45.5 ± 6.3	2.6	
CIT-800	12.5 ± 1.4	50.8 ± 5.0	4.1	
CIT-980	12.1 ± 0.8	69.7 ± 7.3	5.8	
CTAB-600	25	57	2.3	
CTAB-20-850	23	89	3.9	
CTAB-40-850	44	160	3.6	
CTAB-1400	25	256	10.2	

5.3.2 TEM evaluation for surface coating

GNRs used in this study are either citrate or CTAB coated. The media is deionized water or 3 mmol/L aqueous CTAB. In addition to the native coating, non-volatiles (e.g., CTAB, salts) in the medium will dry onto the GNR surface during the ES process. The total dried coating thickness must be included for an accurate mobility model (Eq. (5.1)). In order to sample a sufficient number of GNRs, samples were collected at the native concentration, although the DMA-spICP-MS measurements were, out of necessity, performed at much lower concentrations.

Two representative TEM images show evidence for a thin low density adlayer on the surface of GNRs. (Figure 5.3)

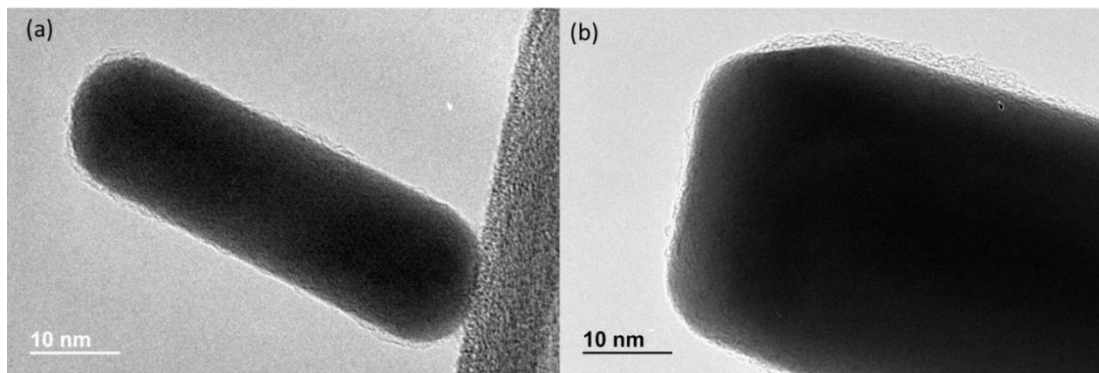


Figure 5.3. Two representative TEM images show evidence for a thin low density adlayer on the surface of GNRs. Both citrate and CTAB coatings were examined: (a) CIT-660 (b) CTAB-40-850

The difference in thickness of the adlayer on GNRs for native concentration and 60× dilution was evaluated for CTAB-1400 as an example and proved to be negligibly small

(Figure 5.4). Therefore, it is reasonable to assume that this sampling method at the native concentration is representative.

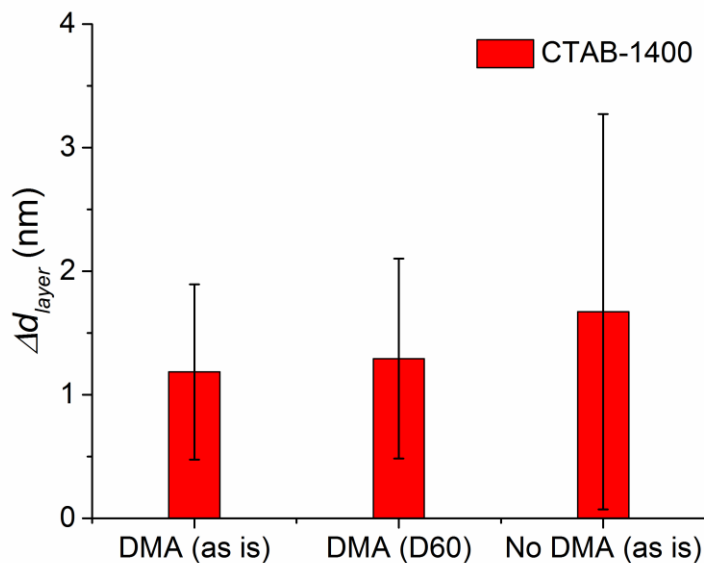


Figure 5.4. Comparison of dilution (D60 stands for 60 times dilution compared with original (as is) solution). The thickness of layer observed with DMA size selection is compared with that without DMA selection. Neither effect of dilution nor DMA selection has obvious effect on layer thickness. Around 10 GNRs with multiple places along each were measured to give an average and error bar standards for one standard deviation.

In imaging the GNRs, a thin low electron density adlayer is apparent. This adlayer is persistent for most of the rods, even though its thickness is non-uniform in some cases, and could vary slightly from GNR to GNR within the same sample. Mean values (from around 10 GNRs for each sample and from different spots on the grid for a single GNR

sample) was used to estimate the thickness (Figure 5.5(a)). The number of GNRs collected through DMA electrostatic deposition on lacey carbon film is very sparse even after duration of a 7 h collection. Further, ES tends to degrade after long hours of operating. Therefore, it becomes technical difficulty to collect large amount of GNRs samples for subsequent TEM imaging. To compromise and in hope to be statistically confident, we did the comparison of a layer thickness for randomly chosen 5 GNRs from around 50 GNRs samples (for both citrate and CTAB coating). It indicated that the adlayer thickness of 5 GNRs was representative of that of around 50 GNRs statistically. (Figure 5.5(b)) It is assumed this layer is the native coating plus any non-volatiles from the ES treatment. The contribution from non-volatiles was also estimated and evaluated based on the non-volatile peak from ES-DMA-CPC. Figure 5.6 is an example of mobility size distribution for CIT-660. Peak at 8nm is representative of dried particle in non-volatile species, and peak at 34nm is representative of gold nanorods. The volume of the non-volatile species would be estimated by $d_{s,r}^3$. This same volume of non-volatile species will form a thickness layer (Δr) on the rod nanoparticle with radius of r and length of L . These parameters follow Eq. 5.4:

$$\frac{\pi}{6} d_{s,r}^3 = \pi(r_r + \Delta r)^2 L - \pi r^2 = \pi \Delta r^2 L + 2\pi r \Delta r \quad (5.4)$$

Contribution of non-volatiles from ES (i.e. Δr) was calculated based on Eq. (5.4) and listed in Table 5.3. Since the samples are all measured in its original concentration, the contribution from ES as listed in Table 5.3 is the maximum estimation.

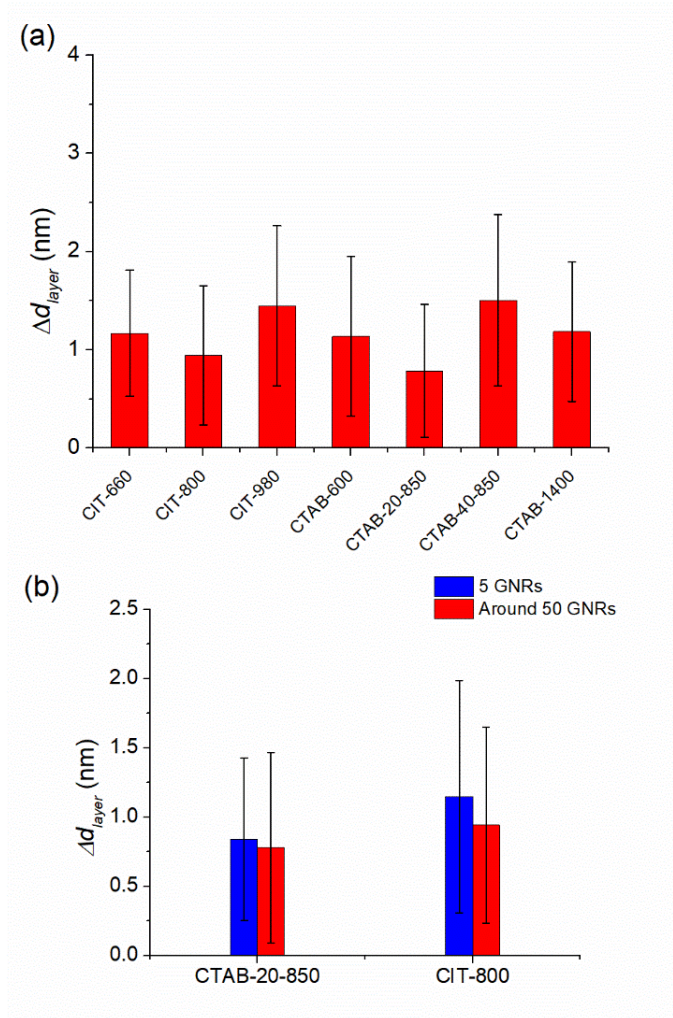


Figure 5.5. (a) Layer thickness of all GNRs by electrostatic deposition of peak size selected by DMA. Around 10 GNRs with multiple places along each were measured to give an average and error bar standards for one standard deviation. (b) Comparison of number of GNRs sampled (5 vs around 50) on determination of layer thickness for both CTAB and CIT coated sample. Multiple places along each were measured to give an average and error bar standards for one standard deviation.

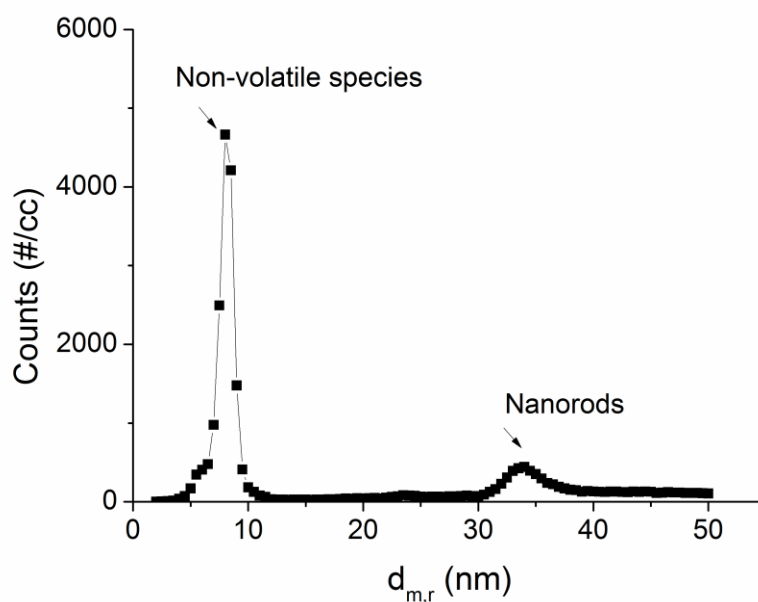


Figure 5.6. Mobility size distribution of CIT-600 by ES-DMA-CPC at its original concentration.

Table 5.3: Contribution of non-volatiles from ES to layer thickness (nm)

GNRs	Contribution from ES to layer thickness(nm)
CIT-660	0.2
CIT-800	2.2
CIT-980	0.1
CTAB-600	1.1
CTAB-20-850	0.1
CTAB-40-850	0.1
CTAB-1400	0.3

Finally, we incorporate the thickness of the coating layer (Δd_{layer}) into Eq. (5.1) to obtain a complete mobility model:

$$d_{m,r} = ((d_r + \Delta d_{gas} + \Delta d_{layer})(L_r + \Delta d_{gas} + \Delta d_{layer}) + \frac{1}{2}(d_r + \Delta d_{gas} + \Delta d_{layer})^2)^{\frac{1}{2}} \quad (5.5)$$

5.3.3 Accuracy of DMA-spICP-MS for quantitative GNR dimensions

The seven GNR samples listed in Table 5.1 were analyzed by DMA-spICP-MS, and the d_r and L_r were compared (see Figure 5.7(a)) with values directly obtained by TEM (which is used here as a benchmark). Overall, the values are consistent and comparable. Due to the nature of the method, the accuracy of measured d_r and L_r relies strongly on that of $d_{m,r}$ and v measurement. Using Eq. (5.1) and (5.2), v and $d_{m,r}$ were calculated based on d_r and L_r obtained directly from TEM (Δd_{layer} and Δd_{gas} were added to the calculation in Eq. 5.1). The measured $d_{m,r}$, and v by DMA-spICP-MS was then compared with this calculated (benchmark) value and the difference reported as relative error.

$$relative\ error = \frac{d_{m,r}\ by\ DMA-spICP-MS - d_{m,r}\ theoretical\ calculation\ based\ on\ TEM}{d_{m,r}\ theoretical\ calculation\ based\ on\ TEM} \% \quad (5.6)$$

In Figure 5.7(b), For most of the GNRs examined, both $d_{m,r}$ and v measurement fell within a 10 % relative error range . CIT-660 and CTAB-20-850 have relatively larger deviation in v than the other GNRs with -19% and -14% respectively. Another important observation is that, even though the error in $(d_{m,r}, v)$ are comparable ((7%, -1%), (3%, 9%), (-4%, -9%)) for CIT-800, CIT-980, and CTAB-40-850 respectively (Figure 5.7(b)), the prediction of d_r and L_r (Figure 5.7(a)) for CIT-800 deviated from TEM to larger extent (39% in L_r and 16% in d_r) in comparison to others ((i.e. CIT-980 (3% in L_r , and 3% in d_r), CTAB-40-850 (10% in L_r and 1% in d_r)). This indicates that different geometries of GNRs have different sensitivity (robustness) to error in $d_{m,r}$ and v measurement. This also indicates the weight or importance of error in $d_{m,r}$ and v measurement could be different in influencing the final accuracy of prediction of L_r and d_r . A detailed robustness analysis explaining this phenomenon was discussed in following section. Despite this, most GNRs, d_r and L_r lie well within the one standard deviation range of TEM results (error bars represent 1σ). The relatively large error bars from TEM (more than 100 GNRs) indicates the polydisperse nature of the GNR samples. It should be noted that the DMA-spICP-MS method measures the geometry of the peak center population and therefore has a negligible polydispersity.

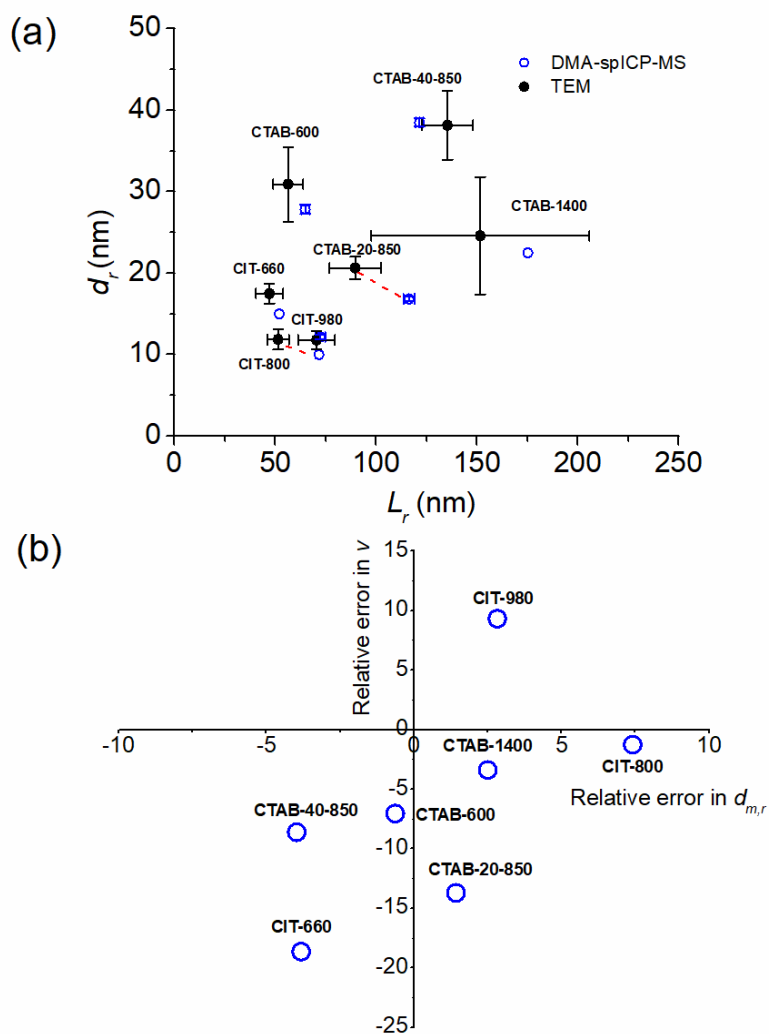


Figure 5.7. (a) Comparing d_r and L_r determined by DMA-spICP-MS (solid circles) to that obtained by TEM (open circles). Red dash lines which connected data corresponding to the same sample were used to guide eye. Error bars represent one standard deviation (3 replicate measurements for DMA-spICP-MS and around 200 GNRs for TEM). (b) Relative error (%) in $d_{m,r}$ and v measured by DMA-spICP-MS in comparison to theoretical calculation based on TEM.

5.3.4 Robustness Analysis

To test the method robustness, the effect of perturbation (bias or error) in each parameter (i.e., $d_{m,r}$, v and Δd_{layer}) on the final predicted d_r and L_r was evaluated. The $d_{m,r}$ and v based on TEM results was used as a benchmark (zero point of x-axis in Figure 5.8) for quantifying extent of perturbation. For the Δd_{layer} , the actual thickness measured from TEM was used as benchmark. When examining the perturbation of one parameter, say, $d_{m,r}$, the other parameters (v and Δd_{layer}) were kept at the benchmark value. A 5 % perturbation in $d_{m,r}$ is $1.05\times$ benchmark $d_{m,r}$, while -5% is $0.95\times$ the benchmark value. All three parameters were then applied to our model to predict d_r and L_r . The final combined error (CE) in comparison to actual d_r and L_r in TEM was used as a quantitative metric for the method and is mathematically defined as:

$$CE = \left(\left(\frac{d_r - d_{r,0}}{d_{r,0}} \right)^2 + \left(\frac{L_r - L_{r,0}}{L_{r,0}} \right)^2 \right)^{\frac{1}{2}} \quad (5.7)$$

Where $d_{r,0}$ and $L_{r,0}$ is the benchmark TEM diameter and length of GNRs.

From the definition of CE, $CE/2$ represented the averaged error in prediction of d_r and L_r . Figure 5.8(a) presents the change of predicted d_r , L_r and CE as a function of $d_{m,r}$ perturbation. d_r and L_r changed in the opposite direction (red and black trace) with respect to perturbation in $d_{m,r}$, while there was a minimum (valley) for CE (blue trace).

Next we evaluated the effect of perturbation in d_p and v , examining two different geometries (CIT-800 with d_r of 11.9nm and L_r of 51.4nm, and CTAB-40-850 with d_r of 38.2nm and L_r of 135.4 nm). In Figure 5.8(b), for the same percentage of perturbation in both $d_{m,r}$ and v , v yields a much lower final CE for the two geometries of GNRs examined. This means v is more resistant to perturbation in measurement compared to

$d_{m,r}$. This explained CIT-800 exhibited largest deviation in d_r and L_r prediction, because it has the largest error in $d_{m,r}$ measurement. Meanwhile, for the same extent of perturbation in either $d_{m,r}$ or v , larger size GNRs (CTAB-850 in comparison to CIT-800) exhibited slightly higher CE and therefore were slightly less robust. Still, 0%-5% perturbation in v yields negligibly small CE ($CE/2 < 6\%$) meaning on average $< 6\%$ error in prediction of d_r and L_r . However 0%-5% perturbation in $d_{m,r}$ yield relatively larger ($CE/2 < 23\%$) error in prediction, meaning care should be taken more when conducting mobility measurement.

Finally, the perturbation in layer thickness was also examined. In this case, larger size GNRs (e.g., CTAB-40-850) yield a smaller CE with respect to the same extent of perturbation (Figure 5.8(c)) This is because the relatively smaller influence of layer thickness is to that of larger diameter.

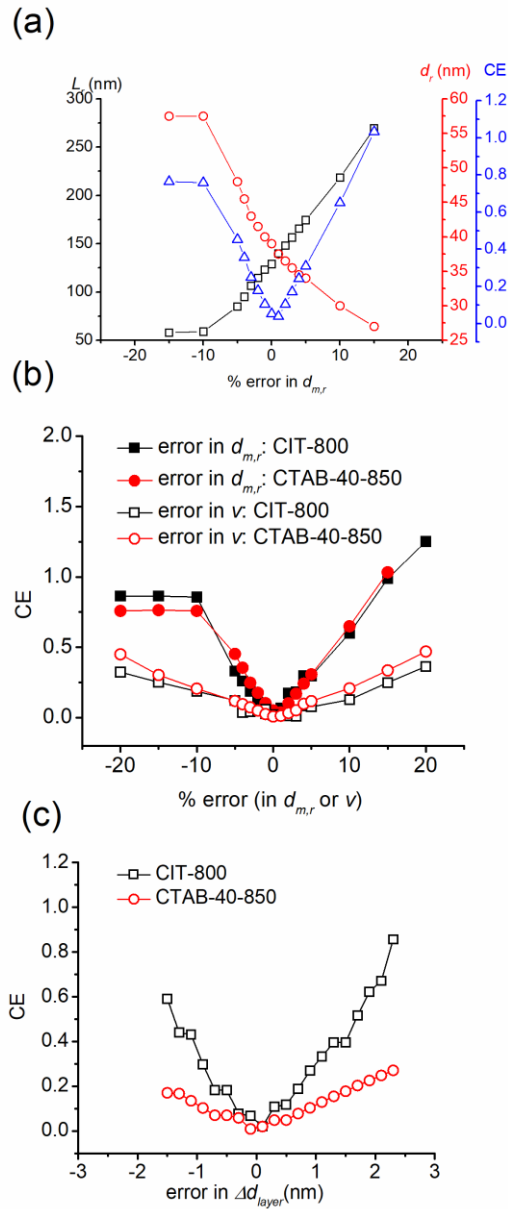


Figure 5.8. Robustness analysis of DMA-spICP-MS method. CE is defined as the combined error as defined in Eq. 5.7. (a) Change of L_r , d_r , and CE with respect to perturbation in $d_{m,r}$ measurement (CTAB-40-850 as an example). (b) Effect of both $d_{m,r}$ and v perturbation on CE comparing two different geometries (CIT-800 vs. CTAB-40-850). (c) Effect of layer Δd_{layer} on CE comparing two different geometries (CIT-800 vs. CTAB-40-850).

5.3.5 Nanorod Detection and Separation Based on Aspect Ratio

The quality and purity of synthesized GNRs is essential for application, however polydispersed GNRs with undesired by-products are frequently observed in both laboratory and commercial grade materials [156, 160]. From a quality control perspective, applicability of DMA-spICP-MS for such a purpose was investigated by intentionally combining GNRs having different geometries (i.e., CTAB-20-850, CTAB-40-850 and CTAB-1400) with spheroidal gold NPs (CTAC-50). A contour plot is used for visualization and interpretation of the data. Prior to the construction of the contour plot, the intensity of GNRs for each spike were converted to volume (and further to diameter) using RM8013 as a calibration standard. Figure 5.9(a) shows that four populations can be resolved, each representing a specific geometry/size combination. The white line represents the theoretical expectation for spherical nanoparticles, where the volume based diameter d_{vol} should track linearly with the mobility diameter $d_{m,r}$. This line was constructed by linear fit to RM8012 and RM8013. The slope of which is about 0.94, not 1, means there is inherently a bias in mobility based diameter versus volume based diameter. Among the four populations, one lies very close to the white line, which corresponds to CTAC-50 spherical gold nanoparticles. The other populations deviate from the theoretical line, indicating non-spherical geometry, i.e., the different GNRs in the mixture. Using $d_{m,r}$ and d_{vol} from the peak of each population to our model, the d_r and L_r for each GNR are obtainable. The results for determining the GNR geometries from the mixture are compared with that from individual measurements as well as benchmark TEM values in Figure 5.9(b). The layer thickness was considered in all cases. The d_r and L_r measured from multicomponent mixtures

agrees well with individual measurements as well as comparing with TEM benchmark values, and therefore indicates robustness of the method. The DMA-spICP-MS method can thus distinguish spherical nanoparticles from rods, has sufficient resolution to separate GNRs from different geometries, and yields an accurate dimensional measurement for each population in a mixture.

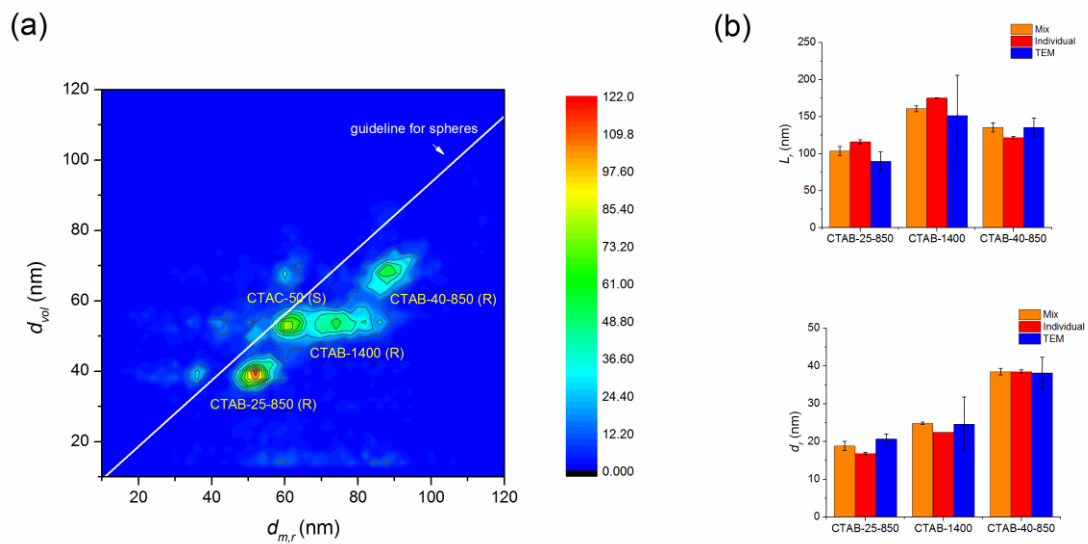


Figure 5.9 (a) Comparison of volume-based d_{vol} and mobility diameter $d_{m,r}$ for mixture of GNRs and gold nano-spheres. (b) L_r , d_r obtained from mixture, individual and that of TEM as benchmark.

In some cases, there may be no significant adlayer on the ES processed GNRs and the gas molecule (i.e. argon) contribution is small (i.e., $\Delta d_{gas} + \Delta d_{layer} \approx 0$). For example, this may include GNRs that have no ligand functionalization, GNRs in a cleaner buffer, or GNRs that can be dialyzed into a volatile buffer (such as ammonium

acetate) without loss of stability. In this case, a reduced form combining Eq. (5.1)-(5.2) would be obtained as follows:

$$\rho_a = \frac{v_{mobility}}{v} = \frac{2(AR+0.5)^{1.5}}{3AR} \quad (5.8)$$

Where $\frac{v_{mobility}}{v}$ is defined here as a mobility-based apparent density, ρ_a [159].

Theoretically, for a mixture of GNRs with different geometries or aspect ratios, one could differentiate between the species using ρ measured by DMA-spICP-MS or use ρ_a to estimate the aspect ratio. The GNR samples examined in this study are not sufficiently stable after removing the buffer components, and we did not have a perfect mixture of clean or non-surface functionalized GNRs available to test this relationship. Instead, for this purpose, we utilized the same rod mixture and gold nanospheres as in Figure 5.9(a) and therefore with an expectation of some deviation from equation (5.8). The different populations have been identified as in Figure 5.9(a) and the peak value ($d_{m,r}$, d_{vol}) was utilized to calculate ρ (i.e., $v_{mobility} = \frac{\pi}{6}d_{m,r}^3$, $v = \frac{\pi}{6}d_{vol}^3$). Each population was therefore represented by black open circles in Figure 5.10(a) where ρ_a vs. $d_{m,r}$ was presented. The blue line represents the theoretical relationship between ρ_a and AR based on Eq. (5.8). For each GNR, from the experimentally measured ρ_a its corresponding AR was derived from the blue curve. Briefly, we draw a horizontal line from the center of the dot to a point where it intersects the blue line. The x value at that point is the aspect ratio (gray dotted line). The aspect ratios obtained in this manner for the three GNR populations yielded values of about 8.1, 8.9 and 4.9 (orange bar in Figure 5.10(b)). These values correspond to CTAB-20-850 CTAB-1400 and CTAB-40-850 with TEM benchmark AR to be 4.3, 6.9 and 3.6 respectively (blue bar in Figure

5.10(b)). The reason for the observed deviation from the true AR is primarily due to the assumption that $\Delta d_{gas} + \Delta d_{layer} \approx 0$. If the adlayer obtained from TEM image was considered in the model the AR obtained therein from Figure 5.9 (b) orange bar, mix based on $AR = L_r/d_r$ for the three rods are 5.5, 6.5, and 3.5 for CTAB-20-850, CTAB-1400, and CTAB-40-850 respectively (red bar in Figure 5.10 (b)). This is very consistent with the benchmark TEM.

Overall, the AR differentiation within a mixture of GNRs obtained by DMA-spICP-MS measurement is deemed satisfactory, and we anticipate an improvement in agreement for samples in a cleaner buffer and without the CTAB coating. It should be noted that one open circle data point lies just above the spheres line (red dotted line in 5.10(a)) and with a predicted AR of roughly 2. This is because we applied rod equations to the spherical CTAC-50 nanoparticle. An AR of 2 in this case is also a good indication of “quasi-spherical” shape. The slope of the blue curve represents the sensitivity of the DMA-spICP-MS method in distinguishing GNRs of differing AR . In our case, a variation of AR ranging from 1 to 10, would result in an apparent density change of roughly 1. This indicates that this method is limited in sensitivity with respect to AR determination. Regardless, the technique shows promise in its capacity for separating and distinguishing mixtures of GNRs with different dimensions and AR values, and its low detection limits ($\approx 10^5$ particles/mL). [159]

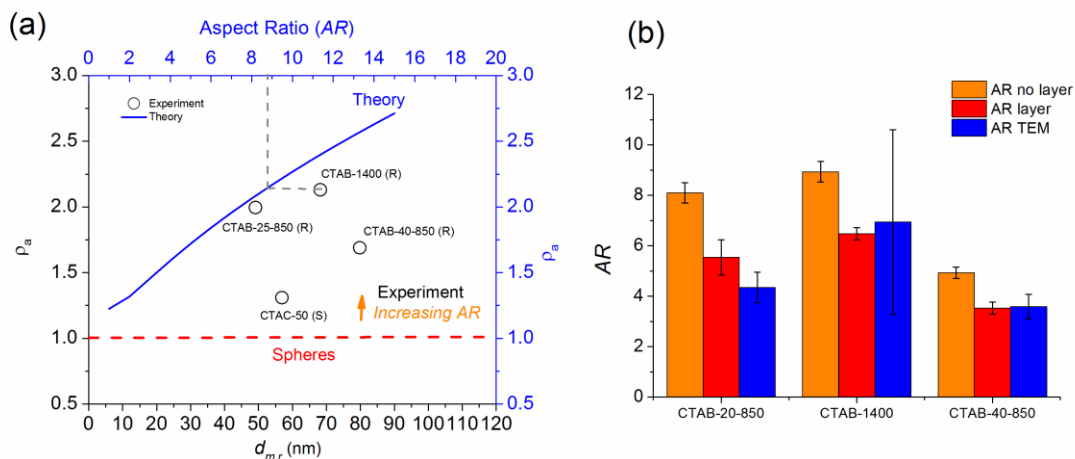


Figure 5.10. (a) Distinguishing mixtures of gold nanorods and spheres by aspect ratios. Black hollow dots are experimental data ($d_{m,r}$ vs. ρ_a). Blue line represented theoretical relationship between AR and ρ_a . (b) Comparison of AR by three different method: (1) AR no layer means deriving AR from theoretical curve as in (a), with assumption of no layer on rods. (2) AR layer means deriving AR from geometry obtained from figure 5.9(b) (i.e. mix, orange bar, $AR = L_r/d_r$). (3) AR TEM is that calculated from geometry measured by TEM ($AR = L_r/d_r$).

5.4 Conclusions

By combining information obtained from two orthogonal techniques operated in tandem, we have demonstrated the capacity for ES-DMA-spICP-MS to simultaneously quantify both the length and diameter of technologically important gold nanorod samples over a wide range of dimensions. Accuracy was determined by comparison with direct measurements obtained off-line using TEM imaging. Due to the nature of spICP-MS, this method has an inherent advantage of fast sampling at low

concentration. Due to the high-resolution nature of the DMA, impurities can be distinguished from nanorods and rods within an extremely narrow dimensional range (i.e., single mode population) can be selected for analysis by varying the applied voltage. A simple model was presented and evaluated. The results suggest this approach has relevance in quality assessment in R&D and quality control in manufacturing for asymmetric nanomaterials.

Chapter 6: Feasibility of ES-DMA to characterize an open and high order structure protein particle.

6.1 Introduction

Informative and fast physical characterization tools are essential to assure quality and safety of pharmaceutical products during development and manufacture.

Characterization aspects may include structure, stability, impurity detection etc.

Cryo-TEM has been used to examine viral structures close to native (hydrated) state with atomic scale resolution. However handling of sample is complicated and needs to be very careful. Low temperature required to prevent electron beam damage and reliance on highly sophisticated and expensive machinery limit its wide applicability.

[^{161, 162}] Staining-TEM will induce possible artifacts due to sample staining and fixing (false positive interactions that form during stain drying). For ultracentrifugation, structural, conformation and molecular interaction information can be obtained from concentration distribution under centrifugal field. [¹⁶³] This method, however, is also time and labor intensive and not suitable for routine analysis. On the other hand, DLS is a relatively fast analysis tool to detect nanoparticle size, and is very sensitive to large aggregates. However, it is not appropriate for heterogeneous samples containing mixed populations.

ES-DMA has been applied for the analysis of intact protein complexes, [¹⁶⁴] viruses, [^{165, 166, 167}] and bacteriophages. [¹⁶⁶] ES-DMA can provide information of size, aggregation states [¹⁶⁸] as well as viral integrity. [¹⁶⁵] One of the major concerns regarding electrospray process is the possible influence on altering the structure of analytes. Electrospray has been shown to be sufficiently gentle to preserve spheroidal

capsids. [169] MS2 was demonstrated to retain viability after electrospray aerosolization. [166, 170, 171] On the other hand, rod-like or elongated virus structures may experience degradation following electrospray process. Rod-like tobacco mosaic virus capsids were shown to be fragmented or bent by observation of TEM after collection. [172]

In this chapter, an interesting open and high-order rosette structure protein particle was examined by ES-DMA. The protein particles are composed of multiple hatpin-shaped rod oligomers arranged in the form of rosettes. [173] This chapter investigated the feasibility of ES-DMA to study the open rosette structure protein particles. We examined the effect of electrospray on particle structure. To assist visualization of protein structure after electrospray, staining procedure was optimized. Finally, mobility simulation by MOBCAL was performed to assign oligomeric structures in the mobility spectrum.

6.2 Experimental

Buffer exchange (i.e. to 175mM ammonium acetate (AmAc)) was performed prior to analysis by ES-DMA. Two staining reagents (i.e. phosphotungstic acid (PTA) and uranyl acetate (UAc)) and three TEM grids (i.e. carbon, SiO/Formvar, carbon/Formvar) were used to optimize staining procedure. Surfaces were functionalized by poly-l-lysine when necessary. Nanometer aerosol sampler was used for electrostatic collection of protein particles after electrospray. TEM grids were mounted on the center electrode. For solution protein sample, one drop was drop-cast onto appropriate TEM grids, dried and followed by negative staining. Protein particles after electrospray were deposited electrostatically to TEM grid mounted in aerosol sampler, and then followed by

negative staining. Aerosol sampler was operated at a voltage of -9.5 kV and a gas flow of 0.9 liter/min.

6.3 Results and Discussion

6.3.1 Consideration prior to ES-DMA measurement

There were several factors to be considered for accurate ES-DMA measurement. First, the original protein particles were dispersed in formulation buffer. The presence of nonvolatile salts and surfactants may cause issues such as clogging of electrospray capillary and destabilization of electrospray. Most importantly, the additional signal associated with these species could mask the signals from protein analytes. Buffer exchange to 175mM AmAc was therefore conducted prior to DMA measurement. The protein particles were stable for at least 2 weeks after buffer exchange demonstrated by three orthogonal measurements including RP-HPLC, DLS and DMA. RP-HPLC and DLS data comparing proteins before and after buffer exchange were not shown. Figure 6.1(a) presented the mobility size spectrum for protein particles measured by ES-DMA at three time points after buffer exchange. It was clearly shown that the mobility size distribution remained largely unchanged during 2-week period. The protein particles stored in 175mM buffer were therefore claimed to be stable for at least 2 weeks. The slight decrease in peak signal at around 10 nm was assumed to be attributed to the decrease in instrument sensitivity.

Secondly, to accurately characterize protein particle size and oligomers, care should be taken to avoid droplet induced aggregation. If the concentration of measured sample was too high, two or more analyte particles were possibly entrapped in one electrospray droplet. This resulted in the observation of oligomers originated from the droplet

formation and not the true oligomers from the sample. Therefore, we optimized the concentration of protein solutions so that the effect from droplet induced aggregation was avoided. Theoretical parameter of λ , $\lambda = V_d \times C_p$ physically represented the mean number of particles per final droplet. V_d is droplet volume and C_p is analyte number concentration. The lower the concentration, the less possibility of droplet induced aggregation. A practical criterion for the cutoff is a critical concentration of C_p , further dilution upon which yields no difference between ratios of any two peaks (i.e. peaks at 10 nm, 12.5 nm and 15.5 nm). In Figure 6.1(b), The ratio between peak intensity at 10 nm to that at 12.5 nm remains the same for 10 \times and 100 \times dilution. This meant concentration for 10 \times dilution was low enough to avoid any droplet induced aggregation. It was therefore safe and recommended to work at concentrations equal or lower than 10 \times .

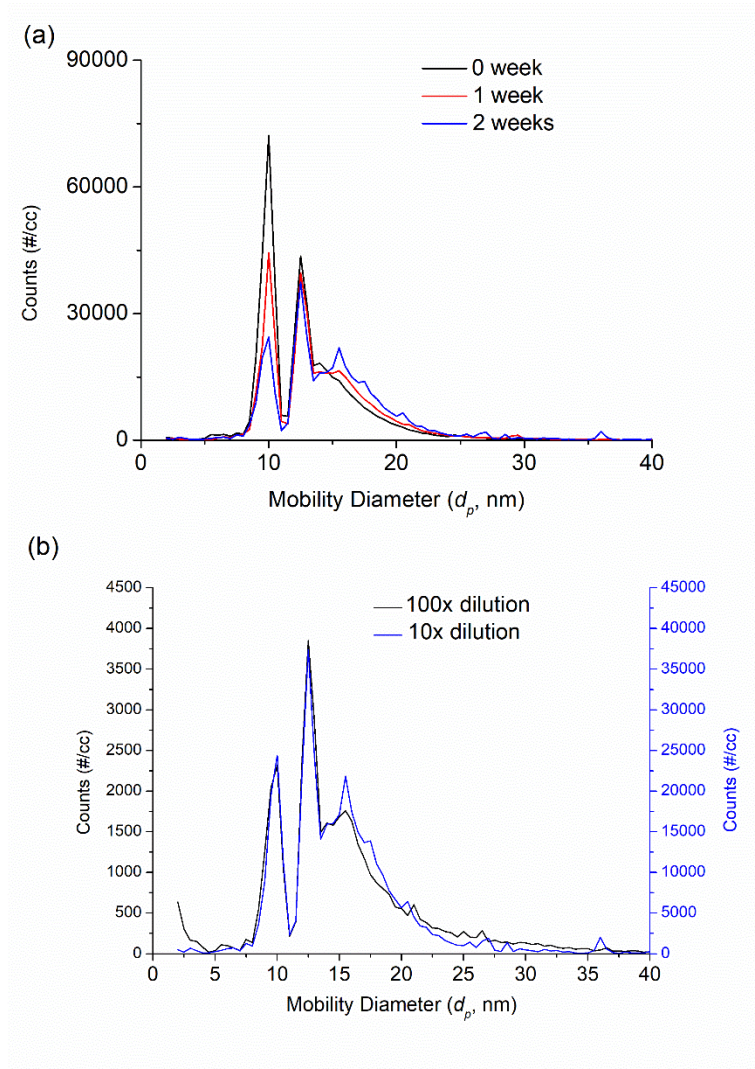


Figure 6.1. (a) Mobility size spectrum for protein particles after buffer exchange at three time points: 0 week (right after buffer exchange), 1 week, and 2 weeks. Samples were diluted 10 times right (10 \times) before conducting DMA experiment. (b) Mobility spectrum comparing different dilutions (i.e. 100 \times vs. 10 \times). No droplet induced aggregation was observed at that of 10 \times concentration.

6.3.2 Staining Protocol Development for Aerosol Protein Particle Deposition

To visualize the protein particle structure after electrospray process, electrostatic collection of particles was performed by nanometer aerosol sampler followed by negative staining. It is more challenging task than staining solution samples. First the number concentration decreased due to loss during electrospray and charging (i.e. only charged particles are captured by aerosol sampler). In addition, the poor interactions between aerosol phase protein particles and TEM grid surface was assumed to account for the poor landing efficiency. This was demonstrated by difficulties in observing protein particles on TEM grid after negative staining. It was therefore necessary to optimize the negative staining protocols including stain types as well as TEM grid types. Because the collection of protein particles after electrospray deposition was relatively time and labor consuming, the optimization was initially conducted with solution samples. First, we examined two different stain types (i.e. PTA and UAc). It was clearly demonstrated that UAc (i.e. Figure 6.2(b)) yielded better contrast compared with PTA (i.e. Figure 6.2(a)). UAc was therefore used for our study. It was shown that the protein particles are composed of multiple hatpin-shaped rod oligomers arranged in the form of rosettes. (Detailed discussions in following section). Four types of TEM grid surface were also examined: carbon, carbon-formvar, carbon coated with poly-l-lysine as well as carbon-formvar with poly-l-lysine coating. No significant difference for imaging performance was found for the four different TEM grid types (data not shown). However, there was an effect of TEM grid types for protein samples collected after electrospray. It was found that silicon monoxide formvar (SiO/F) yielded the best

negative staining performance. Figure 6.2(c) and (d) were two examples of carbon grid and SiO/Formvar grid both by UAc staining. The reason for the difference was not completely understood and it was assumed to be attributed to specific surface interaction between protein particles by aerosol landing and TEM grid surface.

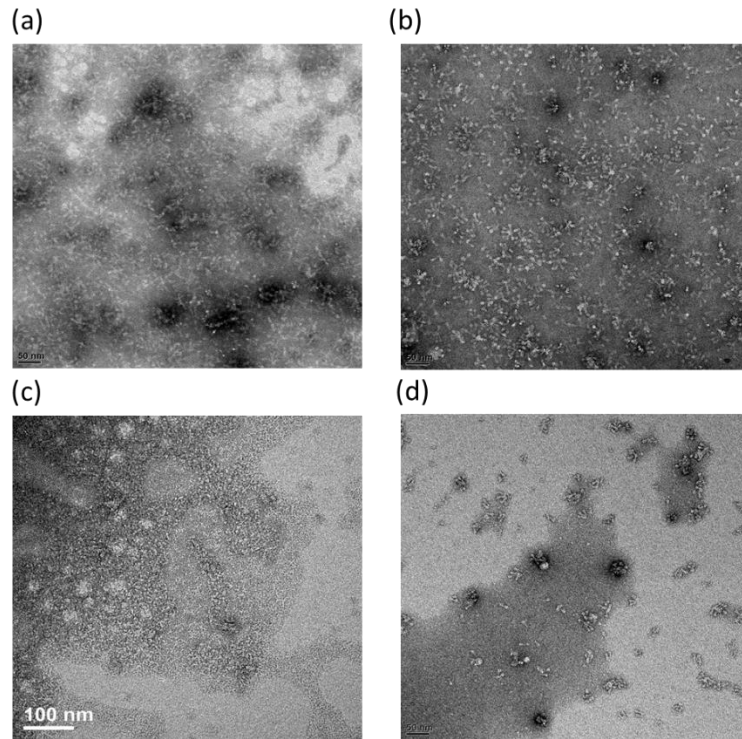


Figure 6.2. (a) PTA was used as stain for protein particles in solution. (b) UAc was used as stain for protein particles in solution. (c) Carbon grid by UAc staining for electrospay deposited protein particles. (d) Silicon monoxide-formvar grid by UAc staining for electrospay deposited protein particles.

6.3.3 Protein Particle Structure after ES

With the negative staining protocol optimized, we moved on to investigate the geometries of protein particles after electrospay. Figure 6.3(a) showed a clear negative

staining TEM image for protein particles after electrospray. Comparing with images for particles in solution (Figure 6.3(b)), the overall protein particle structures were largely unchanged after electrospray process. The average numbers of hatpin-shaped rods constituting the rosette particle structure were comparatively less than that from solution. This indicated possible influence of fragmentation for rosettes from electrospray process. Nonetheless, there were still particles with large rosette structures preserved as shown in zoom-in from Figure 6.3(a). The geometries of hatpin-shape rods constituting particle rosettes were measured and compared with that from solution. The statistics were summarized in Figure 6.3(c). If we define the length (L) and diameter (d) of the hatpin-shape rod constituting rosette particles, both L and d remained unchanged after electrospray. There is no collapse of the protein structure.

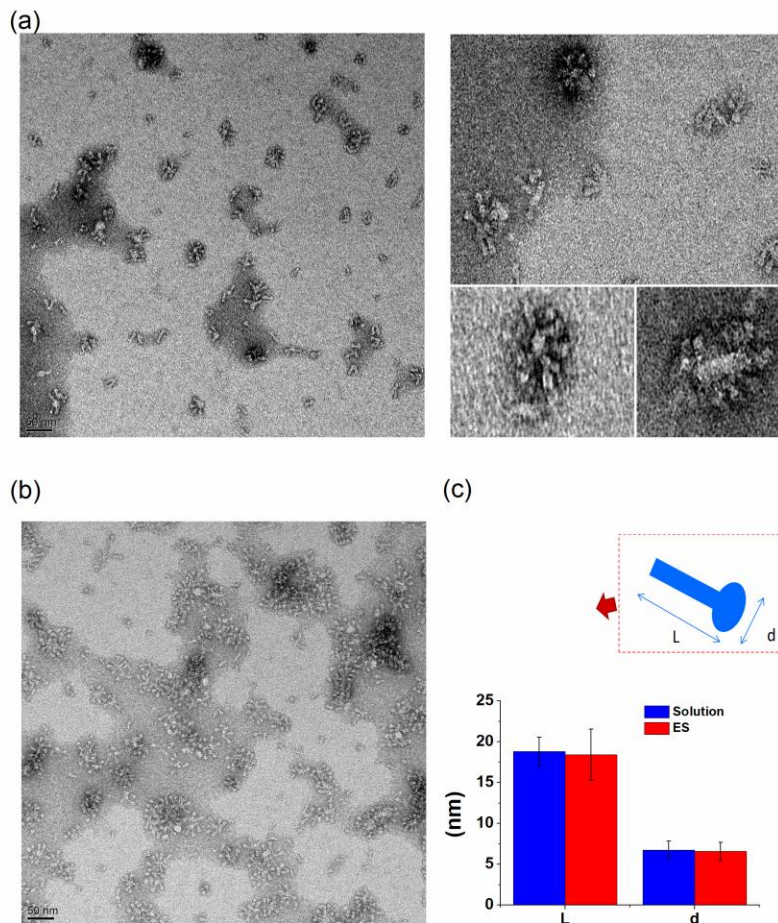


Figure 6.3. (a) Staining TEM for protein particles collected after electrospray and zoom-in (b) Staining TEM for particles from solution (c) Geometries comparison of L and d for a hatpin-shaped rods forming protein particles (i.e. from electrospray and solution, summarized from TEM measurement).

6.3.4 Assignment of Peaks in Mobility Spectrum by MOBCAL Simulation

Finally, to assign the peaks from mobility spectrum (i.e. 10 nm, 12.5 nm and 15.5 nm) to appropriate structures, MOBCAL simulation using Projection Area Method (PA)

was performed. The protein rosette structures were assembled by putting one, two and three rods in arranged directions (named monomer, dimer trimer). The coordinates were then used as input in MOBCAL. The raw data obtained from PA method were averaged cross section (A), and the spherical mobility diameter, d_p , were obtained as: $d_p = \left(\frac{4A}{\pi}\right)^{1/2}$. The mobility spectrum by ES-DMA was compared with that from simulation (Table 6.1). The three experimental peaks at 10 nm, 12.5 nm and 15.5 nm were close to that from MOBCAL simulation (9.5 nm, 13.1 nm and 16.3 nm). The peaks by ES-DMA were then assigned to be monomer, dimer and trimer (i.e. trimer is protein particle composed of three hatpin-shaped rods). This assignment could be further verified through TEM after collection of protein particles selected at specific peak position. Currently, there was challenge in obtaining enough population for successful negative staining. Future work would focus on addressing this challenge.

Table 6.1. Simulation of mobility size by MOBCAL

Protein	Simulation by Projection Area Method		Experimental Mobility Diameter (nm)
	Averaged Cross Section (Å)	Spherical Mobility Diameter (nm)	
Particle monomer	7111	9.5	10
Particle dimer	14308	13.1	12.5
Particle trimer	20901	16.3	15.5

6.4 Conclusions

ES-DMA was applied in this study to investigate an interesting open and high-order rosette protein structure. Protein particles after buffer exchange was deemed stable for at least 2 weeks. Droplet induced aggregation was avoided by optimization of concentration. SiO/Formvar in combination with UAc stains were the best for negative staining performance. Overall rosette structures were maintained after electrospray. The average numbers of hatpin-shaped rods constituting the rosette particle structure were comparatively less than that from solution, indicating possible influence of fragmentation for rosettes from electrospray process. The hatpin-shaped rods did not collapse and remained at the same length and diameter. MOBCAL simulation for the assembled structure showed close matches with measured mobility spectrum. Future work would include optimization of electrospray conditions and elucidating relationship with respect to protein particle structure maintenance.

Chapter 7: Conclusion and Future work.

7.1 Conclusion

The dissertation provides a systematic study on developing and extending the capability of novel hyphenated instruments composing primarily ion mobility analysis (i.e. DMA) and ICP-MS to characterization of nanoparticles for biomedical and environmental application. Polyethylene glycol (PEG) stabilized cisplatin-complexed AuNPs were synthesized as a model anti-tumor drug platform, where cisplatin (Pt^{II}) is attached via a dendrimer-like ligand. Surface modification and its influence on drug loading, colloidal stability and drug release were assessed. It was shown that upon complexation of Pt^{II} , colloidal stability decreased, but PEGylated AuNP conjugates (Pt^{II} -AuNP-dendrimer-SH-PEG) exhibited enhanced dispersion stability with an insignificant trade-off in drug loading capacity – compared with the non-PEGylated control. In this context, the effect of varying PEG concentration and molar mass was investigated. On a quantitative basis, the extent of PEGylation was characterized and its influence on dispersion stability and drug loading was examined using a novel, previously described electrospray differential mobility analyzer (ES-DMA) hyphenated with an inductively coupled plasma mass spectrometer (ICP-MS). Using ES-DMA-ICP-MS, AuNP conjugates were size-classified based on their electrical mobility, while Pt^{II} loading was simultaneously quantified by determination of Pt mass. Colloidal stability was quantitatively evaluated in biologically relevant media by ES-DMA-ICP-MS. Finally, Pt^{II} release performance was evaluated, and exhibited a clear pH dependence. Relative molecular mass of the PEG had no significant influence on Pt^{II} uptake or release

performance, while PEGylation substantially improved the colloidal stability of the conjugate.

We further applied a novel single particle mode ICP-MS hyphenated with ES-DMA for real-time size, mass and concentration measurement of nanoparticles (NPs) on a particle-to-particle basis. As proof-of-concept study, the feasibility of this technique was validated through both concentration and mass calibration using NIST gold NP reference materials. A detection limit of 10^5 NPs mL⁻¹ was determined under current experimental conditions, which is about four orders of magnitude lower in comparison to a traditional ES-DMA setup using a condensation particle counter as principal detector. Furthermore, independent and simultaneous quantification of both size and mass of NPs provides information regarding NP aggregation states. Two demonstrative applications include gold NP mixtures with a broad size range (30 nm to 100 nm), and aggregated gold NPs with a primary size of 40 nm. A detection limit of 10^5 NPs mL⁻¹ was determined under current experimental conditions, which is about four orders of magnitude lower in comparison to a traditional ES-DMA setup using a condensation particle counter as principal detector. This technique showed the capability (1) Clearly resolving NP populations from a mixture containing a broad size range; (2) Defining a linear relationship between mobility size and one-third power of ICP-MS intensity for spherical NPs; (3) Monitoring propagation of NP aggregation with well characterized oligomers; and (4) Differentiating aggregated NPs and non-aggregated states based on the “apparent density” derived from both DMA size and spICP-MS mass.

Based on the technique developed, ES-DMA-spICP-MS was applied as a fast and quantitative method for determining the geometries of nanorods (i.e., length and

dimeter). Seven gold nanorod samples with different geometries (diameters 11.8-38.2 nm, aspect ratios 1.8-6.9) were used to evaluate the method. We demonstrate that DMA-spICP-MS can (1) achieve quantification of both length and diameter comparable with TEM analysis, (2) make statistically meaningful measurements in minutes at low concentrations and (3) separate nanorods from spheres and quantify the geometry of each population. A robustness analysis of this method was performed to evaluate accuracy of the approach.

Finally, an interesting rosette structure protein particle without protective hard shell was investigated. The effect of electrospray aerosolizing process on the preservation of protein structure was examined by gas phase ES collection followed by staining TEM. The staining procedure was optimized in terms of stain types and grid type. Uranyl acetate combined with silicon monoxide-formvar was shown to yield best imaging performance for gas collection of protein particle. It was demonstrated electrospray was gentle enough to maintain largely the structure, with some fragmentation. The structure of hatpin-shaped rods constituting the high-order rosette was maintained and did not collapse. Mobility size distribution representing different protein rosette structures measured by ES-DMA was consistent with that from MOBCAL simulation.

7.2 Recommended Future Work

The instrument developed in this dissertation serves as a complimentary analysis method in quantifying different aspects of nanoparticles including, but are not limited to, size, shape, mass, concentration, aggregation and surface coating states. The accuracy and robustness of the methods were primarily validated through reference

material or well defined materials. More work is recommended in application of this method to more realistic samples such as nanoparticles in environmental media (i.e. soil extract) and examine the interaction between nanoparticles and natural colloids. This would require optimization of DMA-ICP-MS setup to increase detection limit as well as extending maximum mobility size range. In addition, with the improvement in hardware in ICP-MS instrument, and therefore the capability in multicomponent analysis in single particle ICP-MS mode, there are more opportunities in DMA-spICPMS for nanoparticle characterization.

References

1. ASTM E2456 - 06 Standard Terminology Relating to Nanotechnology. 2006.
2. Powell, M. C.; Griffin, M. P.; Tai, S. Bottom-up risk regulation? How nanotechnology risk knowledge gaps challenge federal and state environmental agencies. *Environ Manage* **2008**, *42* (3), 426-43.
3. Tiede, K.; Boxall, A. B.; Tear, S. P.; Lewis, J.; David, H.; Hasselov, M. Detection and characterization of engineered nanoparticles in food and the environment. *Food Addit Contam Part A Chem Anal Control Expo Risk Assess* **2008**, *25* (7), 795-821.
4. Lin, P. C.; Lin, S.; Wang, P. C.; Sridhar, R. Techniques for physicochemical characterization of nanomaterials. *Biotechnol Adv* **2014**, *32* (4), 711-26.
5. Duncan, R.; Gaspar, R. Nanomedicine(s) under the microscope. *Mol Pharm* **2011**, *8* (6), 2101-41.
6. Farokhzad, O. C.; Langer, R. Nanomedicine: developing smarter therapeutic and diagnostic modalities. *Adv Drug Deliv Rev* **2006**, *58* (14), 1456-9.
7. Hall, J. B.; Dobrovolskaia, M. A.; Patri, A. K.; McNeil, S. E. Characterization of nanoparticles for therapeutics. *Nanomedicine (Lond)* **2007**, *2* (6), 789-803.
8. Patri, A. K.; Dobrovolskaia, M. A.; Stern, S. T.; McNeil, S. E. *Preclinical Characterization of Engineered Nanoparticles Intended for Cancer Therapeutics / Nanotechnology for Cancer Therapy*; CRC Press 2006.
9. Sadrieh, N. Overview of CDER Experience with Nanotechnology-related Drugs. In: Slides for the August 9, 2012 Meeting of the Advisory Committee for Pharmaceutical Science and Clinical Pharmacology, 2012.
10. Cruz, C. N.; Tyner, K. M.; Velazquez, L.; Hyams, K. C.; Jacobs, A.; Shaw, A. B.; Jiang, W.; Lionberger, R.; Hinderling, P.; Kong, Y.; Brown, P. C.; Ghosh, T.; Strasinger, C.; Suarez-Sharp, S.; Henry, D.; Van Uitert, M.; Sadrieh, N.; Morefield, E. CDER risk assessment exercise to evaluate potential risks from the use of nanomaterials in drug products. *Aaps j* **2013**, *15* (3), 623-8.
11. Feng, S. S. Nanoparticles of biodegradable polymers for new-concept chemotherapy. *Expert Rev Med Devices* **2004**, *1* (1), 115-25.
12. Xiue Jiang; Janguang Jiang; Yongdong Jin; Erkang Wang, a.; Dong*, S. Effect of Colloidal Gold Size on the Conformational Changes of Adsorbed Cytochrome c: Probing by Circular Dichroism, UV-Visible, and Infrared Spectroscopy. **2004**.
13. Brodbeck, W. G.; Shive, M. S.; Colton, E.; Nakayama, Y.; Matsuda, T.; Anderson, J. M. Influence of biomaterial surface chemistry on the apoptosis of adherent cells. *J Biomed Mater Res* **2001**, *55* (4), 661-8.
14. Asati, A.; Santra, S.; Kaittanis, C.; Perez, J. M. Surface-Charge-Dependent Cell Localization and Cytotoxicity of Cerium Oxide Nanoparticles. **2010**.
15. George, S.; Lin, S.; Ji, Z.; Thomas, C. R.; Li, L.; Mecklenburg, M.; Meng, H.; Wang, X.; Zhang, H.; Xia, T.; Hohman, J. N.; Lin, S.; Zink, J. I.; Weiss, P. S.; Nel, A. E. Surface Defects on Plate-Shaped Silver Nanoparticles Contribute to Its Hazard Potential in a Fish Gill Cell Line and Zebrafish Embryos. **2012**.

16. Pal, S.; Tak, Y. K.; Song, J. M. Does the Antibacterial Activity of Silver Nanoparticles Depend on the Shape of the Nanoparticle? A Study of the Gram-Negative Bacterium *Escherichia coli*. **2007**.
17. Buzea, C.; Pacheco, II; Robbie, K. Nanomaterials and nanoparticles: sources and toxicity. *Biointerphases* **2007**, 2 (4), Mr17-71.
18. Hardman, R. A Toxicologic Review of Quantum Dots: Toxicity Depends on Physicochemical and Environmental Factors. In *Environ Health Perspect*, 2006; Vol. 114, pp 165-72.
19. Briscoe, C. J.; Hage, D. S. Factors affecting the stability of drugs and drug metabolites in biological matrices. *Bioanalysis* **2009**, 1 (1), 205-20.
20. Nel, A. E.; Mädler, L.; Velegol, D.; Xia, T.; Hoek, E. M. V.; Somasundaran, P.; Klaessig, F.; Castranova, V.; Thompson, M. Understanding biophysicochemical interactions at the nano[ndash]bio interface. *Nature Materials* **2009**, 8 (7), 543-557.
21. Ferrari, M. Nanogeometry: Beyond drug delivery. *Nature Nanotechnology* **2008**, 3 (3), 131-132.
22. Vance, M. E.; Kuiken, T.; Vejerano, E. P.; McGinnis, S. P.; Hochella, M. F., Jr.; Rejeski, D.; Hull, M. S. Nanotechnology in the real world: Redeveloping the nanomaterial consumer products inventory. *Beilstein J Nanotechnol* **2015**, 6, 1769-80.
23. Stone, V.; Nowack, B.; Baun, A.; van den Brink, N.; Kammer, F.; Dusinska, M.; Handy, R.; Hankin, S.; Hasselov, M.; Joner, E.; Fernandes, T. F. Nanomaterials for environmental studies: classification, reference material issues, and strategies for physico-chemical characterisation. *Sci Total Environ* **2010**, 408 (7), 1745-54.
24. Oberdorster, G.; Maynard, A.; Donaldson, K.; Castranova, V.; Fitzpatrick, J.; Ausman, K.; Carter, J.; Karn, B.; Kreyling, W.; Lai, D.; Olin, S.; Monteiro-Riviere, N.; Warheit, D.; Yang, H. Principles for characterizing the potential human health effects from exposure to nanomaterials: elements of a screening strategy. *Part Fibre Toxicol* **2005**, 2, 8.
25. Powers, K. W.; Brown, S. C.; Krishna, V. B.; Wasdo, S. C.; Moudgil, B. M.; Roberts, S. M. Research strategies for safety evaluation of nanomaterials. Part VI. Characterization of nanoscale particles for toxicological evaluation. *Toxicol Sci* **2006**, 90 (2), 296-303.
26. Thomas, T.; Thomas, K.; Sadrieh, N.; Savage, N.; Adair, P.; Bronaugh, R. Research Strategies for Safety Evaluation of Nanomaterials, Part VII: Evaluating Consumer Exposure to Nanoscale Materials. *Toxicological Sciences* **2006**, 91 (1), 14-19.
27. Warheit, D. B. How meaningful are the results of nanotoxicity studies in the absence of adequate material characterization? *Toxicol Sci* **2008**, 101 (2), 183-5.
28. Klaine, S. J.; Alvarez, P. J. J.; Batley, G. E.; Fernandes, T. F.; Handy, R. D.; Lyon, D. Y.; Mahendra, S.; McLaughlin, M. J.; Lead, J. R. Nanomaterials in the environment: Behavior, fate, bioavailability, and effects. *Environmental Toxicology and Chemistry* **2008**, 27 (9), 1825-1851.
29. Powers, K. W.; Palazuelos, M.; Moudgil, B. M.; Roberts, S. M. Characterization of the size, shape, and state of dispersion of nanoparticles for toxicological studies. *Nanotoxicology* **2009**, 1 (1), 42-51.
30. Laborda, F.; Bolea, E.; Cepria, G.; Gomez, M. T.; Jimenez, M. S.; Perez-Arantegui, J.; Castillo, J. R. Detection, characterization and quantification of inorganic

engineered nanomaterials: A review of techniques and methodological approaches for the analysis of complex samples. *Anal Chim Acta* **2016**, *904*, 10-32.

31. Calzolari, L.; Gilliland, D.; Rossi, F. Measuring nanoparticles size distribution in food and consumer products: a review. *Food Addit Contam Part A Chem Anal Control Expo Risk Assess* **2012**, *29* (8), 1183-93.

32. Hendrickson, O. D.; Safenkova, I. V.; Zherdev, A. V.; Dzantiev, B. B.; Popov, V. O. Methods of detection and identification of manufactured nanoparticles | SpringerLink. *Biophysics* **2012**, *56* (6), 961-986.

33. Lapresta-Fernández, A.; Salinas-Castillo, A.; Llana, S. A. d. l.; Costa-Fernández, J. M.; Domínguez-Meister, S.; Cecchini, R.; Capitán-Vallvey, L. F.; Moreno-Bondi, M. C.; Marco, M.-P.; Sánchez-López, J. C.; Anderson, I. S. A General Perspective of the Characterization and Quantification of Nanoparticles: Imaging, Spectroscopic, and Separation Techniques. *Critical Reviews in Solid State and Materials Sciences* **2014**, *39* (6), 423-458.

34. Sadik, O. A.; Du, N.; Kariuki, V.; Okello, V.; Bushlyar, V. Current and Emerging Technologies for the Characterization of Nanomaterials. *ACS Sustainable Chemistry & Engineering* **2014**, *2* (7), 1707-1716.

35. Kim, B.; Murayama, M.; Colman, B. P.; Hochella, M. F., Jr. Characterization and environmental implications of nano- and larger TiO₂ particles in sewage sludge, and soils amended with sewage sludge. *J Environ Monit* **2012**, *14* (4), 1129-37.

36. Yang, Y.; Wang, Y.; Westerhoff, P.; Hristovski, K.; Jin, V. L.; Johnson, M. V.; Arnold, J. G. Metal and nanoparticle occurrence in biosolid-amended soils. *Sci Total Environ* **2014**, *485-486*, 441-9.

37. Mavrocordatos, D.; Pronk, W.; Boiler, M. Analysis of environmental particles by atomic force microscopy, scanning and transmission electron microscopy. *Water Sci Technol* **2004**, *50* (12), 9-18.

38. Cao, B.; Xu, H.; Mao, C. Transmission Electron Microscopy as a Tool to Image Bio-Inorganic Nanohybrids: The Case of Phage-Gold Nanocomposites. *Microsc Res Tech* **2011**, *74* (7), 627-35.

39. Sapsford, K. E.; Tyner, K. M.; Dair, B. J.; Deschamps, J. R.; Medintz, I. L. Analyzing nanomaterial bioconjugates: a review of current and emerging purification and characterization techniques. *Anal Chem* **2011**, *83* (12), 4453-88.

40. Gallego-Urrea, J. A.; Tuoriniemi, J.; Hasswillov, M. Applications of particle-tracking analysis to the determination of size distributions and concentrations of nanoparticles in environmental, biological and food samples. *TrAC Trends in Analytical Chemistry* **2011**, *30* (3), 473-483.

41. Shang, L.; Wang, Y.; Jiang, J.; Dong, S. pH-dependent protein conformational changes in albumin:gold nanoparticle bioconjugates: a spectroscopic study. *Langmuir* **2007**, *23* (5), 2714-21.

42. Baudot, C.; Tan, C. M.; Kong, J. C. FTIR spectroscopy as a tool for nanomaterial characterization. **2010**, *53* (6), 434-438.

43. Hind, A. R.; Bhargava, S. K.; McKinnon, A. At the solid/liquid interface: FTIR/ATR--the tool of choice. *Adv Colloid Interface Sci* **2001**, *93* (1-3), 91-114.

44. Liu, H.; Webster, T. J. Nanomedicine for implants: a review of studies and necessary experimental tools. *Biomaterials* **2007**, *28* (2), 354-69.

45. Loof, D.; Hiller, M.; Oschkinat, H.; Koschek, K. Quantitative and Qualitative Analysis of Surface Modified Cellulose Utilizing TGA-MS. *Materials* **2016**, *9* (6), 415.
46. Krystek, P.; Ulrich, A.; Garcia, C. C.; Manohar, S.; Ritsema, R. Application of plasma spectrometry for the analysis of engineered nanoparticles in suspensions and products. *Journal of Analytical Atomic Spectrometry* **2011**, *26* (9), 1701-1721.
47. Gray, E. P.; Bruton, T. A.; Higgins, C. P.; Halden, R. U.; Westerhoff, P.; Ranville, J. F. Analysis of gold nanoparticle mixtures: a comparison of hydrodynamic chromatography (HDC) and asymmetrical flow field-flow fractionation (AF4) coupled to ICP-MS. *Journal of Analytical Atomic Spectrometry* **2012**, *27* (9), 1532-1539.
48. Allen, M. D.; Raabe, O. G. Slip Correction Measurements of Spherical Solid Aerosol-Particles in an Improved Millikan Apparatus. *Aerosol Science and Technology* **1985**, *4* (3), 269-286.
49. Li, M. D.; You, R.; Mulholland, G. W.; Zachariah, M. R. Development of a Pulsed-Field Differential Mobility Analyzer: A Method for Measuring Shape Parameters for Nonspherical Particles. *Aerosol Science and Technology* **2014**, *48* (1), 22-30.
50. Kousaka, Y.; Endo, Y.; Ichitsubo, H.; Alonso, M. Orientation-Specific Dynamic Shape Factors for Doublets and Triplets of Spheres in the Transition Regime. *Aerosol Science and Technology* **1996**, *24* (1), 36-44.
51. Kim, S. H.; Mulholland, G. W.; Zachariah, M. R. Understanding ion-mobility and transport properties of aerosol nanowires. **2007**, *38* (8), 823-842.
52. Li, M.; Mulholland, G. W.; Zachariah, M. R. The Effect of Orientation on the Mobility and Dynamic Shape Factor of Charged Axially Symmetric Particles in an Electric Field. *Aerosol Science and Technology* **2012**, *46* (9), 1035-1044.
53. Li, M.; You, R.; Mulholland, G. W.; Zachariah, M. R. Evaluating the Mobility of Nanorods in Electric Fields. *Aerosol Science and Technology* **2013**, *47* (10), 1101-1107.
54. Li, M. Quantifying Particle Properties from Ion-Mobility Measurements. University of Maryland, College Park 2012.
55. Martinez-Lozano, P.; Fernandez de la Mora, J. Resolution improvements of a nano-DMA operating transonically - ScienceDirect. *Journal of Aerosol Science* **2017**, *37* (4), 500-512.
56. Tammet, H. F. The aspiration method for the Determination of Atmospheric-Ion Spectra. *Israel Program for Scientific Translations, Jerusalem (The original work in Russian was published in 1967)* **1970**.
57. Salm, J. Diffusion Distortions in a Differential Mobility Analyzer: The Shape of Apparent Mobility Spectrum. *Aerosol Science and Technology* **2000**, *32* (6), 602-612.
58. Rossell-Llompart, J.; Loscertales, I. G.; Bingham, D.; Fernandez de la Mora, J. Sizing nanoparticles and ions with a short differential mobility analyzer - ScienceDirect. *Journal of Aerosol Science* **1996**, *27* (5), 695-719.
59. Gillig, K. J.; Chen, C. H. Increasing the Performance of Portable Ion Mobility Analyzers: Development of the Periodic Focusing Differential Mobility Analyzer (PFDMA). *Mass Spectrom (Tokyo)* **2014**, *3* (Spec Issue).

60. Cai, R.; Chen, D.-R.; Jiming, H.; Jiang, J. A miniature cylindrical differential mobility analyzer for sub-3 nm particle sizing. *Journal of Aerosol Science* **2017**, *106*, 111–119.
61. Mora, J. F. d. I.; Kozłowski, J. Hand-held differential mobility analyzers of high resolution for 1–30 nm particles: Design and fabrication considerations. *Journal of Aerosol Science* **2013**, *57*, 45–53.
62. Barmounis, K.; Maisser, A.; Schmidt-Ott, A.; Biskos, G. Lightweight differential mobility analyzers: Toward new and inexpensive manufacturing methods. *Aerosol Science and Technology* **2015**, *50* (1), 2-5.
63. Li, M.; Guha, S.; Zangmeister, R.; Tarlov, M. J.; Zachariah, M. R. Quantification and Compensation of Nonspecific Analyte Aggregation in Electrospray Sampling. *Aerosol Science and Technology* **2011**, *45* (7), 849-860.
64. Li, M.; Tan, J.; Tarlov, M. J.; Zachariah, M. R. Absolute Quantification Method for Protein Concentration. *Analytical Chemistry* **2014**, *86* (24), 12130-12137.
65. Tsai, D. H.; Pease, L. F., 3rd; Zangmeister, R. A.; Tarlov, M. J.; Zachariah, M. R. Aggregation kinetics of colloidal particles measured by gas-phase differential mobility analysis. *Langmuir* **2009**, *25* (1), 140-6.
66. Saffari, H.; Malugin, A.; Ghandehari, H.; Pease III, L. F. Electrostatic deposition of nanoparticles into live cell culture using an electrospray differential mobility analyzer (ES-DMA). *Journal of Aerosol Science* **2012**, *48*, 56–62.
67. Hogan, C. J., Jr.; de la Mora, J. F. Ion mobility measurements of nondenatured 12-150 kDa proteins and protein multimers by tandem differential mobility analysis-mass spectrometry (DMA-MS). *J Am Soc Mass Spectrom* **2011**, *22* (1), 158-72.
68. Christopher J. Hogan, J.; Ruotolo, B. T.; Robinson, C. V.; Mora, J. F. d. I. Tandem Differential Mobility Analysis-Mass Spectrometry Reveals Partial Gas-Phase Collapse of the GroEL Complex. *Journal of Physical Chemistry B* **2011**, *115* (13), 3614-3621.
69. Jr., C. J. H.; Loo, R. R. O.; Loo, J. A.; Mora, J. F. d. I. Ion mobility–mass spectrometry of phosphorylase B ions generated with supercharging reagents but in charge-reducing buffer. *Physical Chemistry Chemical Physics* **2010**, *12* (41).
70. Guha, S.; Li, M.; Tarlov, M. J.; Zachariah, M. R. Electrospray-differential mobility analysis of bionanoparticles. *Trends Biotechnol* **2012**, *30* (5), 291-300.
71. Tseng, Y. H.; Pease, L. F., 3rd. Electrospray differential mobility analysis for nanoscale medicinal and pharmaceutical applications. *Nanomedicine* **2014**, *10* (8), 1591-600.
72. Thomas, R. *Practical Guide to ICP-MS: A Tutorial for Beginners, Third Edition*; CRC Press 2013.
73. Mitrano, D. M.; Leshner, E. K.; Bednar, A.; Monserud, J.; Higgins, C. P.; Ranville, J. F. Detecting nanoparticulate silver using single-particle inductively coupled plasma-mass spectrometry. *Environ Toxicol Chem* **2012**, *31* (1), 115-121.
74. Laborda, F.; Bolea, E.; Jiménez-Lamana, J. Single Particle Inductively Coupled Plasma Mass Spectrometry: A Powerful Tool for Nanoanalysis. *Analytical Chemistry* **2013**, *86* (5), 2270-2278.
75. Myojo, T.; Takaya, M.; Ono-Ogasawara, M. DMA as a Gas Converter from Aerosol to "Argonsol" for Real-Time Chemical Analysis Using ICP-MS. *Aerosol Science and Technology* **2010**, *36* (1), 76-83.

76. Carazzone, C.; Raml, R.; Pergantis, S. A. Nanoelectrospray Ion Mobility Spectrometry Online with Inductively Coupled Plasma-Mass Spectrometry for Sizing Large Proteins, DNA, and Nanoparticles. *Analytical Chemistry* **2008**, *80* (15), 5812-5818.
77. Nishiguchi, K.; Utani, K.; Fujimori, E. Real-time multielement monitoring of airborne particulate matter using ICP-MS instrument equipped with gas converter apparatus. *Journal of Analytical Atomic Spectrometry* **2008**, *23*, 1125-1129.
78. Elzey, S.; Tsai, D. H.; Yu, L. L.; Winchester, M. R.; Kelley, M. E.; Hackley, V. A. Real-time size discrimination and elemental analysis of gold nanoparticles using ES-DMA coupled to ICP-MS. *Anal Bioanal Chem* **2013**, *405* (7), 2279-88.
79. Elzey, S.; Tsai, D. H.; Yu, L. L.; Winchester, M. R.; Kelley, M. E.; Hackley, V. A. Real-time size discrimination and elemental analysis of gold nanoparticles using ES-DMA coupled to ICP-MS. *Analytical and Bioanalytical Chemistry* **2013**, *405* (7), 2279-2288.
80. Wang, D.; Lippard, S. J. Cellular processing of platinum anticancer drugs. *Nat Rev Drug Discov* **2005**, *4* (4), 307-20.
81. Kelland, L. The resurgence of platinum-based cancer chemotherapy. *Nature Reviews Cancer* **2007**, *7* (8), 573-584.
82. Jung, Y. W.; Lippard, S. J. Direct cellular responses to platinum-induced DNA damage. *Chemical Reviews* **2007**, *107* (5), 1387-1407.
83. Seiwert, T. Y.; Salama, J. K.; Vokes, E. E. The concurrent chemoradiation paradigm - general principles. *Nature Clinical Practice Oncology* **2007**, *4* (2), 86-100.
84. Rose, P. G. New treatment paradigm for locally advanced cervical cancer? *Nature Reviews Clinical Oncology* **2011**, *8* (7), 388-390.
85. Barabas, K.; Milner, R.; Lurie, D.; Adin, C. Cisplatin: a review of toxicities and therapeutic applications. *Vet Comp Oncol* **2008**, *6* (1), 1-18.
86. Wheate, N. J.; Walker, S.; Craig, G. E.; Oun, R. The status of platinum anticancer drugs in the clinic and in clinical trials. *Dalton Trans* **2010**, *39* (35), 8113-27.
87. Cho, K.; Wang, X.; Nie, S.; Chen, Z. G.; Shin, D. M. Therapeutic nanoparticles for drug delivery in cancer. *Clin Cancer Res* **2008**, *14* (5), 1310-6.
88. Hu, C. M.; Zhang, L. Therapeutic nanoparticles to combat cancer drug resistance. *Curr Drug Metab* **2009**, *10* (8), 836-41.
89. Maeda, H. The enhanced permeability and retention (EPR) effect in tumor vasculature: the key role of tumor-selective macromolecular drug targeting. *Adv Enzyme Regul* **2001**, *41*, 189-207.
90. Tanaka, T.; Shiramoto, S.; Miyashita, M.; Fujishima, Y.; Kaneo, Y. Tumor targeting based on the effect of enhanced permeability and retention (EPR) and the mechanism of receptor-mediated endocytosis (RME). *Int J Pharm* **2004**, *277* (1-2), 39-61.
91. Paciotti, G. F.; Kingston, D. G. I.; Tamarkin, L. Colloidal gold nanoparticles: A novel nanoparticle platform for developing multifunctional tumor-targeted drug delivery vectors. *Drug Development Research* **2006**, *67* (1), 47-54.
92. Bazak, R.; Houry, M.; El Achy, S.; Kamel, S.; Refaat, T. Cancer active targeting by nanoparticles: a comprehensive review of literature. *J Cancer Res Clin Oncol* **2015**, *141* (5), 769-84.

93. Bertrand, N.; Wu, J.; Xu, X.; Kamaly, N.; Farokhzad, O. C. Cancer nanotechnology: the impact of passive and active targeting in the era of modern cancer biology. *Adv Drug Deliv Rev* **2014**, *66*, 2-25.
94. Li, S. D.; Huang, L. Nanoparticles evading the reticuloendothelial system: role of the supported bilayer. *Biochim Biophys Acta* **2009**, *1788* (10), 2259-66.
95. Tanima Bose, D. L., Partha Pratim Mondal, Subhra Mandal. Overview of nano-drugs characteristics for clinical application: the journey from the entry to the exit point | SpringerLink. *Journal of Nanoparticle Research* **2014**, (16), 2527.
96. Ghosh, P.; Han, G.; De, M.; Kim, C. K.; Rotello, V. M. Gold nanoparticles in delivery applications. *Adv Drug Deliv Rev* **2008**, *60* (11), 1307-15.
97. Connor, E. E.; Mwamuka, J.; Gole, A.; Murphy, C. J.; Wyatt, M. D. Gold nanoparticles are taken up by human cells but do not cause acute cytotoxicity. *Small* **2005**, *1* (3), 325-7.
98. FRENS, G. Controlled Nucleation for the Regulation of the Particle Size in Monodisperse Gold Suspensions. *Nature* **1973**, *241* (105), 20-22.
99. Brown, S. D.; Nativio, P.; Smith, J. A.; Stirling, D.; Edwards, P. R.; Venugopal, B.; Flint, D. J.; Plumb, J. A.; Graham, D.; Wheate, N. J. Gold Nanoparticles for the Improved Anticancer Drug Delivery of the Active Component of Oxaliplatin. *J Am Chem Soc* **2010**, *132* (13), 4678-84.
100. Carter, J. D.; Cheng, N. N.; Qu, Y. Q.; Suarez, G. D.; Guo, T. Nanoscale energy deposition by x-ray absorbing nanostructures. *Journal of Physical Chemistry B* **2007**, *111* (40), 11622-11625.
101. Pradhan, A. K.; Nahar, S. N.; Montenegro, M.; Yu, Y.; Zhang, H. L.; Sur, C.; Mrozik, M.; Pitzer, R. M. Resonant X-ray enhancement of the Auger effect in high-Z atoms, molecules, and nanoparticles: potential biomedical applications. *J Phys Chem A* **2009**, *113* (45), 12356-63.
102. Lee, S. M.; Tsai, D. H.; Hackley, V. A.; Brechbiel, M. W.; Cook, R. F. Surface-engineered nanomaterials as X-ray absorbing adjuvant agents for Auger-mediated chemo-radiation. *Nanoscale* **2013**, *5* (12), 5252-5256.
103. Tsai, D. H.; Cho, T. J.; Elzey, S. R.; Gigault, J. C.; Hackley, V. A. Quantitative analysis of dendron-conjugated cisplatin-complexed gold nanoparticles using scanning particle mobility mass spectrometry. *Nanoscale* **2013**, *5* (12), 5390-5.
104. Cho, T. J.; Zangmeister, R. A.; MacCuspie, R. I.; Patri, A. K.; Hackley, V. A. Newkome-type dendron stabilized gold nanoparticles: Synthesis, reactivity, and stability. *Chem Mater* **2011**, *23* (10), 2665-76.
105. Ryan, S. M.; Mantovani, G.; Wang, X. X.; Haddleton, D. M.; Brayden, D. J. Advances in PEGylation of important biotech molecules: delivery aspects. *Expert Opinion on Drug Delivery* **2008**, *5* (4), 371-383.
106. Klibanov, A. L.; Maruyama, K.; Beckerleg, A. M.; Torchilin, V. P.; Huang, L. Activity of amphipathic poly(ethylene glycol) 5000 to prolong the circulation time of liposomes depends on the liposome size and is unfavorable for immunoliposome binding to target. *Biochim Biophys Acta* **1991**, *1062* (2), 142-8.
107. Howard, M. D.; Jay, M.; Dziubla, T. D.; Lu, X. PEGylation of Nanocarrier Drug Delivery Systems: State of the Art. *Journal of Biomedical Nanotechnology* **2008**, *4*, 133-148.

108. Comenge, J.; Sotelo, C.; Romero, F.; Gallego, O.; Barnadas, A.; Parada, T. G.; Dominguez, F.; Puentes, V. F. Detoxifying antitumoral drugs via nanoconjugation: the case of gold nanoparticles and cisplatin. *PLoS One* **2012**, *7* (10), e47562.
109. Tsai, D.-H.; DelRio, F. W.; Pettibone, J. M.; Lin, P.-A.; Tan, J.; Zachariah, M. R.; Hackley, V. A. Temperature-Programmed Electrospray–Differential Mobility Analysis for Characterization of Ligated Nanoparticles in Complex Media. *Langmuir* **2013**, *29* (36), 11267-11274.
110. Petroski, J.; El-Sayed, M. A. FTIR study of the adsorption of the capping material to different platinum nanoparticle shapes. *Journal of Physical Chemistry A* **2003**, *107* (40), 8371-8375.
111. Mansur, H. S.; Orefice, R. L.; Mansur, A. A. P. Characterization of poly(vinyl alcohol)/poly(ethylene glycol) hydrogels and PVA-derived hybrids by small-angle X-ray scattering and FTIR spectroscopy. *Polymer* **2004**, *45* (21), 7193-7202.
112. Pease, L. F.; Tsai, D. H.; Zangmeister, R. A.; Zachariah, M. R.; Tarlov, M. J. Quantifying the surface coverage of conjugate molecules on functionalized nanoparticles. *Journal of Physical Chemistry C* **2007**, *111* (46), 17155-17157.
113. Tsai, D. H.; DelRio, F. W.; MacCuspie, R. I.; Cho, T. J.; Zachariah, M. R.; Hackley, V. A. Competitive adsorption of thiolated polyethylene glycol and mercaptopropionic acid on gold nanoparticles measured by physical characterization methods. *Langmuir* **2010**, *26* (12), 10325-33.
114. Ivanov, M. R.; Haes, A. J. Anionic Functionalized Gold Nanoparticle Continuous Full Filling Separations: Importance of Sample Concentration. *Analytical Chemistry* **2012**, *84* (3), 1320-1326.
115. Tsai, D. H.; Cho, T. J.; DelRio, F. W.; Gorham, J. M.; Zheng, J. W.; Tan, J. J.; Zachariah, M. R.; Hackley, V. A. Controlled Formation and Characterization of Dithiothreitol-Conjugated Gold Nanoparticle Clusters. *Langmuir* **2014**, *30* (12), 3397-3405.
116. Ye, L.; Letchford, K.; Heller, M.; Liggins, R.; Guan, D.; Kizhakkedathu, J. N.; Brooks, D. E.; Jackson, J. K.; Burt, H. M. Synthesis and characterization of carboxylic acid conjugated, hydrophobically derivatized, hyperbranched polyglycerols as nanoparticulate drug carriers for cisplatin. *Biomacromolecules* **2011**, *12* (1), 145-55.
117. Kulhari, H.; Pooja, D.; Singh, M. K.; Chauhan, A. S. Optimization of carboxylate-terminated poly(amidoamine) dendrimer-mediated cisplatin formulation. *Drug Dev Ind Pharm* **2015**, *41* (2), 232-8.
118. Yan, X.; Gemeinhart, R. A. Cisplatin delivery from poly(acrylic acid-co-methyl methacrylate) microparticles. *J Control Release* **2005**, *106* (1-2), 198-208.
119. Paraskar, A. S.; Soni, S.; Chin, K. T.; Chaudhuri, P.; Muto, K. W.; Berkowitz, J.; Handlogten, M. W.; Alves, N. J.; Bilgicer, B.; Dinulescu, D. M.; Mashelkar, R. A.; Sengupta, S. Harnessing structure-activity relationship to engineer a cisplatin nanoparticle for enhanced antitumor efficacy. *PNAS* **2010**, *107*, 12435-12440.
120. Contado, C. Nanomaterials in consumer products: a challenging analytical problem. *Frontiers in chemistry* **2015**, *3*, 48.
121. Duncan, T. V. Applications of nanotechnology in food packaging and food safety: barrier materials, antimicrobials and sensors. *Journal of colloid and interface science* **2011**, *363* (1), 1-24.

122. Vance, M. E.; Kuiken, T.; Vejerano, E. P.; McGinnis, S. P.; Hochella, M. F.; Rejeski, D.; Hull, M. S. Nanotechnology in the real world: Redeveloping the nanomaterial consumer products inventory. *Beilstein journal of nanotechnology* **2015**, *6*, 1769-1780.
123. de Dios, A. S.; Diaz-Garcia, M. E. Multifunctional nanoparticles: Analytical prospects. *Anal Chim Acta* **2010**, *666* (1-2), 1-22.
124. Levard, C.; Hotze, E. M.; Lowry, G. V.; Brown, G. E. Environmental Transformations of Silver Nanoparticles: Impact on Stability and Toxicity. *Environ Sci Technol* **2012**, *46* (13), 6900-6914.
125. Reidy, B.; Haase, A.; Luch, A.; Dawson, K. A.; Lynch, I. Mechanisms of Silver Nanoparticle Release, Transformation and Toxicity: A Critical Review of Current Knowledge and Recommendations for Future Studies and Applications. *Materials* **2013**, *6* (6), 2295-2350.
126. Lowry, G. V.; Gregory, K. B.; Apte, S. C.; Lead, J. R. Transformations of Nanomaterials in the Environment. *Environ Sci Technol* **2012**, *46* (13), 6893-6899.
127. Maurer-Jones, M. A.; Gunsolus, I. L.; Murphy, C. J.; Haynes, C. L. Toxicity of Engineered Nanoparticles in the Environment. *Anal Chem* **2013**, *85* (6), 3036-3049.
128. Tuoriniemi, J.; Cornelis, G.; Hasselov, M. Size Discrimination and Detection Capabilities of Single-Particle ICPMS for Environmental Analysis of Silver Nanoparticles. *Analytical Chemistry* **2012**, *84* (9), 3965-3972.
129. Pace, H. E.; Rogers, N. J.; Jarolimek, C.; Coleman, V. A.; Gray, E. P.; Higgins, C. P.; Ranville, J. F. Single particle inductively coupled plasma-mass spectrometry: a performance evaluation and method comparison in the determination of nanoparticle size. *Environ Sci Technol* **2012**, *46* (22), 12272-80.
130. Pace, H. E.; Rogers, N. J.; Jarolimek, C.; Coleman, V. A.; Higgins, C. P.; Ranville, J. F. Determining transport efficiency for the purpose of counting and sizing nanoparticles via single particle inductively coupled plasma mass spectrometry. *Anal Chem* **2011**, *83* (24), 9361-9.
131. Pergantis, S. A.; Jones-Lepp, T. L.; Heithmar, E. M. Hydrodynamic chromatography online with single particle-inductively coupled plasma mass spectrometry for ultratrace detection of metal-containing nanoparticles. *Anal Chem* **2012**, *84* (15), 6454-62.
132. Rakcheev, D.; Philippe, A.; Schaumann, G. E. Hydrodynamic Chromatography Coupled with Single Particle-Inductively Coupled Plasma Mass Spectrometry for Investigating Nanoparticles Agglomerates. *Anal Chem* **2013**, *85* (22), 10643-10647.
133. Loeschner, K.; Navratilova, J.; Kobler, C.; Molhave, K.; Wagner, S.; von der Kammer, F.; Larsen, E. H. Detection and characterization of silver nanoparticles in chicken meat by asymmetric flow field flow fractionation with detection by conventional or single particle ICP-MS. *Anal Bioanal Chem* **2013**, *405* (25), 8185-8195.
134. Group, I. E. W. Validation of analytical procedures: text and methodology Q2(R1). In *International Conference on Harmonisation of Technical requirements for Registration of Pharmaceuticals for Human use*, 2005.
135. Hu, S. H.; Liu, R.; Zhang, S. C.; Huang, Z.; Xing, Z.; Zhang, X. R. A New Strategy for Highly Sensitive Immunoassay Based on Single-Particle Mode Detection by Inductively Coupled Plasma Mass Spectrometry. *J Am Soc Mass Spectr* **2009**, *20* (6), 1096-1103.

136. Lee, S.; Bi, X. Y.; Reed, R. B.; Ranville, J. F.; Herckes, P.; Westerhoff, P. Nanoparticle Size Detection Limits by Single Particle ICP-MS for 40 Elements. *Environ Sci Technol* **2014**, *48* (17), 10291-10300.
137. Hackley, V. *Gold Nanoparticles, Nominal 60 nm Diameter* 2015.
138. Guha, S.; Pease, L. F.; Brorson, K. A.; Tarlov, M. J.; Zachariah, M. R. Evaluation of electrospray differential mobility analysis for virus particle analysis: Potential applications for biomanufacturing. *J Virol Methods* **2011**, *178* (1-2), 201-208.
139. Li, Y.; Shen, W. Morphology-dependent nanocatalysts: rod-shaped oxides. *Chem Soc Rev* **2014**, *43* (5), 1543-74.
140. Huang, X.; Neretina, S.; El-Sayed, M. A. Gold nanorods: from synthesis and properties to biological and biomedical applications. *Adv Mater* **2009**, *21* (48), 4880-910.
141. Shuhui Liang; Fei Teng; G. Bulgan; Ruilong Zong, a.; Zhu*, Y. Effect of Phase Structure of MnO₂ Nanorod Catalyst on the Activity for CO Oxidation. *J. Phys. Chem. C* **2008**, *112* (14), 5307-5315.
142. Reddy, N. K.; Devika, M.; Tu, C. W. High-quality ZnO nanorod based flexible devices for electronic and biological applications. *RSV Adv.* **2014**, *4* (71), 37563-37568.
143. Manekkathodi, A.; Lu, M. Y.; Wang, C. W.; Chen, L. J. Direct Growth of Aligned Zinc Oxide Nanorods on Paper Substrates for Low - Cost Flexible Electronics. *Advanced Materials* **2017**, *22* (36), 4059-4063.
144. Pissuwan, D.; Valenzuela, S.; Cortie, M. B. Prospects for gold nanorod particles in diagnostic and therapeutic applications. *Biotechnol Genet Eng Rev* **2008**, *25*, 93-112.
145. Gold nanorod-based localized surface plasmon resonance biosensors: A review. **2014**, *195*, 332-351.
146. Huff, T. B.; Tong, L.; Zhao, Y.; Hansen, M. N.; Cheng, J. X.; Wei, A. Hyperthermic effects of gold nanorods on tumor cells. *Nanomedicine (Lond)* **2007**, *2* (1), 125-32.
147. S. Link; M. B. Mohamed, a.; El-Sayed*, M. A. Simulation of the Optical Absorption Spectra of Gold Nanorods as a Function of Their Aspect Ratio and the Effect of the Medium Dielectric Constant. *J. Phys. Chem. B* **1999**, *103* (16), 3073-3077.
148. Brioude, A.; Jiang, X. C.; Pileni, M. P. Optical properties of gold nanorods: DDA simulations supported by experiments. *J Phys Chem B* **2005**, *109* (27), 13138-42.
149. Slaughter, L. S.; Chang, W.-S.; Swanglap, P.; Tcherniak, A.; Khanal, B. P.; Zubarev, E. R.; Link, S. Single-Particle Spectroscopy of Gold Nanorods beyond the Quasi-Static Limit: Varying the Width at Constant Aspect Ratio. *J. Phys. Chem. C* **2010**, *114* (11), 4934-4938.
150. and, B. N. K.; Nikolai G. Khlebtsov*, ‡. Multipole Plasmons in Metal Nanorods: Scaling Properties and Dependence on Particle Size, Shape, Orientation, and Dielectric Environment. *J. Phys. Chem. C* **2007**, *111* (31), 11516-11527.
151. Near, R. D.; Hayden, S. C.; El-Sayed, M. A. Thin to Thick, Short to Long: Spectral Properties of Gold Nanorods by Theoretical Modeling. *J. Phys. Chem. C* **2013**, *117* (36), 18653-18656.
152. Xu, N. H.; Bai, B. F.; Tan, Q. F.; Jin, G. F. Fast statistical measurement of aspect ratio distribution of gold nanorod ensembles by optical extinction spectroscopy. *Optics Express* **2013**, *21* (3), 2987-3000.

153. Khlebtsov, B. N.; Khanadeev, V. A.; Khlebtsov, N. G. Observation of Extra-High Depolarized Light Scattering Spectra from Gold Nanorods. *J. Phys. Chem. C* **2008**, *112* (33), 12760-112768.
154. Khlebtsov, B. N.; Khanadeev, V. A.; Khlebtsov, N. G. Extinction and extra-high depolarized light scattering spectra of gold nanorods with improved purity and dimension tunability: direct and inverse problems. *Phys. Chem. Chem. Phys.* **2014**, *16* (12), 5710-5722.
155. Hu, Z. J.; Hou, S.; Ji, Y. L.; Wen, T.; Liu, W. Q.; Zhang, H.; Shi, X. W.; Yan, J.; Wu, X. C. Fast characterization of gold nanorods ensemble by correlating its structure with optical extinction spectral features. *AIP Advances* **2014**, *4* (11), 117137.
156. Nguyen, T.; Liu, J.; Hackley, V. Fractionation and Characterization of High Aspect Ratio Gold Nanorods Using Asymmetric-Flow Field Flow Fractionation and Single Particle Inductively Coupled Plasma Mass Spectrometry. *Chromatography* **2015**, *2* (3), 422-435.
157. Mingdong Li, R. Y., George W. Mulholland, Michael R. Zachariah. Evaluating the Mobility of Nanorods in Electric Fields. *Aerosol Science and Technology* **2013**, *47* (10), 1101-1107.
158. Ku, B. K.; Mora, J. F. d. l. Relation between Electrical Mobility, Mass, and Size for Nanodrops 1–6.5 nm in Diameter in Air. *Aerosol Science and Technology* **2009**, *43* (3), 241-249.
159. Tan, J.; Liu, J.; Li, M.; El Hadri, H.; Hackley, V. A.; Zachariah, M. R. Electrospray-Differential Mobility Hyphenated with Single Particle Inductively Coupled Plasma Mass Spectrometry for Characterization of Nanoparticles and Their Aggregates. *Anal Chem* **2016**, *88* (17), 8548-55.
160. Nguyen, T. M.; Pettibone, J. M.; Gigault, J.; Hackley, V. A. In situ monitoring, separation, and characterization of gold nanorod transformation during seed-mediated synthesis. *Anal Bioanal Chem* **2016**, *408* (9), 2195-201.
161. Wilson, S. M.; Bacic, A. Preparation of plant cells for transmission electron microscopy to optimize immunogold labeling of carbohydrate and protein epitopes. *Nature Protocols* **2012**, *7*, 1716-1727.
162. Pease, L. F., 3rd; Tsai, D. H.; Brorson, K. A.; Guha, S.; Zachariah, M. R.; Tarlov, M. J. Physical characterization of icosahedral virus ultra structure, stability, and integrity using electrospray differential mobility analysis. *Anal Chem* **2011**, *83* (5), 1753-9.
163. Liu, J.; Andya, J. D.; Shire, S. J. A critical review of analytical ultracentrifugation and field flow fractionation methods for measuring protein aggregation. *Aaps j* **2006**, *8* (3), E580-9.
164. Bacher, G.; Szymanski, W. W.; Kaufman, S. L.; Zollner, P.; Blaas, D.; Allmaier, G. Charge-reduced nano electrospray ionization combined with differential mobility analysis of peptides, proteins, glycoproteins, noncovalent protein complexes and viruses. *J Mass Spectrom* **2001**, *36* (9), 1038-52.
165. Leonard F. Pease, I.; Tsai, D.-H.; Brorson, K. A.; Guha, S.; Zachariah, M. R.; Tarlov, M. J. Physical Characterization of Icosahedral Virus Ultra Structure, Stability, and Integrity Using Electrospray Differential Mobility Analysis. *Analytical Chemistry* **2011**, *83* (5), 1753-1759.

166. Christopher J. Hogan, J.; Eric M. Kettleon; Bala Ramaswami; Da-Ren Chen, a.; Biswas*, P. Charge Reduced Electrospray Size Spectrometry of Mega- and Gigadalton Complexes: Whole Viruses and Virus Fragments. *Analytical Chemistry* **2006**, 78 (3), 844-852.
167. Pease, L. F., 3rd. Physical analysis of virus particles using electrospray differential mobility analysis. *Trends Biotechnol* **2012**, 30 (4), 216-24.
168. Pease, L. F., 3rd; Elliott, J. T.; Tsai, D. H.; Zachariah, M. R.; Tarlov, M. J. Determination of protein aggregation with differential mobility analysis: application to IgG antibody. *Biotechnol Bioeng* **2008**, 101 (6), 1214-22.
169. Fuerstenau, S. D.; Benner, W. H.; Thomas, J. J.; Brugidou, C.; Bothner, B.; Siuzdak, G. Mass Spectrometry of an Intact Virus. *Angew Chem Int Ed Engl* **2001**, 40 (3), 541-544.
170. Hogan, C. J., Jr.; Kettleon, E. M.; Lee, M. H.; Ramaswami, B.; Angenent, L. T.; Biswas, P. Sampling methodologies and dosage assessment techniques for submicrometre and ultrafine virus aerosol particles. *J Appl Microbiol* **2005**, 99 (6), 1422-34.
171. Allmaier, G.; Maiber, A.; Laschober, C.; Messner, P.; Szymanski, W. W. Parallel differential mobility analysis for electrostatic characterization and manipulation of nanoparticles and viruses - ScienceDirect. *TrAC Trends in Analytical Chemistry* **2010**, 30 (1), 123-132.
172. Allmaier, G.; Laschober, C.; Szymanski, W. W. Nano ES GEMMA and PDMA, new tools for the analysis of nanobioparticles-protein complexes, lipoparticles, and viruses. *J Am Soc Mass Spectrom* **2008**, 19 (8), 1062-8.
173. Smith, G.; Raghunandan, R.; Wu, Y.; Liu, Y.; Massare, M.; Nathan, M.; Zhou, B.; Lu, H.; Boddapati, S.; Li, J.; Flyer, D.; Glenn, G. Respiratory syncytial virus fusion glycoprotein expressed in insect cells form protein nanoparticles that induce protective immunity in cotton rats. *PLoS One* **2012**, 7 (11), e50852.

Publications

- **Tan, J.**, Yang, Y., Hadri, H.E., Li, M., Hackley, V.A. and Zachariah, M.R. Fast geometry measurement for rod shaped nanoparticle by IMS-ICPMS. Journal of Analytical Atomic Spectrometry (to be submitted)
- **Tan, J.**, Cho, T-J., Liu, J., Hackley, V.A. and Zachariah, M.R. Structure-Function of PEG Stabilized Cisplatin-Complexed Gold Nanoparticles using Hyphenated ES-DMA-ICPMS. Langmuir (submitted, 2017)
- **Tan, J.**, Liu, J., Li, M., Hadri, H.E., Hackley, V.A. and Zachariah, M.R. Electrospray Differential Mobility Hyphenated with Single Particle Mass Spectrometry for Characterization of Nanoparticles and their Aggregates. Analytical Chemistry 2016, 88(17), 8548-55
- Li, M., **Tan, J.**, Tarlov, M., and Zachariah, M.R. Absolute Quantification Method for Protein Concentration. Analytical Chemistry 2014, 86, 12130
- Tsai, D., Cho, T-J., DelRio, F., Zheng, J., **Tan, J.**, Zachariah, M.R. and Hackley, V. Controlled Formation and Characterization of Dithiothreitol-Conjugated Gold Nanoparticle Clusters. Langmuir 2014, 30, 3397
- Zhou, L., You, R., **Tan, J.** and Zachariah, M.R. Wavelength Resolved UV Photoelectric Charging Dynamics of Nanoparticles: Comparison of Spheres and Aggregates. Aerosol Science and Technology 2013, 47, 672
- Tsai, D., DelRio, F.W., Pettibone, J.M., Lin, P-A., **Tan, J.**, Zachariah, M.R. and Hackley, V.A. Temperature-Programmed Electrospray Differential Mobility Analysis for Characterization of Ligated Nanoparticles in Complex Media. Langmuir 2013, 29, 11267

Presentations

- 2016, Global Summit on Regulatory Science (poster)
- 2014, AIChE conference (platform), Best Presentation Award of the Session
- 2014, AAAR conference (platform)
- 2012, PerkinElmer & NIST-Nanolytica Educational Symposium (poster), First Prize